PNNL-28259

Pacific Northwest
NATIONAL LABORATORY

Proudly Operated by **Battelle** *Since 1965*

Third-Year Report of the Atmosphere to Electrons Mesoscale-to-Microscale Coupling Project

Year 3 Report

December 2017

SE Haupt	A Anderson
L Berg	B Brown
M Churchfield	C Draxl
C Kalb	E Koo
B Kosović	R Kotamarthi
L Mazzaro	J Mirocha
E Quon	R Rai
G Sever	

U.S. DEPARTMENT OF
ENERGY

Prepared for the U.S. Department of Energy
under Contract DE-AC05-76RL01830

PACIFIC NORTHWEST NATIONAL LABORATORY
operated by
BATTELLE
for the
UNITED STATES DEPARTMENT OF ENERGY
under Contract DE-AC05-76RL01830

Printed in the United States of America

Available to DOE and DOE contractors from the
Office of Scientific and Technical Information,
P.O. Box 62, Oak Ridge, TN 37831-0062;
ph: (865) 576-8401
fax: (865) 576-5728
email: reports@adonis.osti.gov

Available to the public from the National Technical Information Service
5301 Shawnee Rd., Alexandria, VA 22312
ph: (800) 553-NTIS (6847)
email: orders@ntis.gov <http://www.ntis.gov/about/form.aspx>
Online ordering: http://www.ntis.gov

This document was printed on recycled paper.

(8/2010)

PNNL-28259

Third-Year Report of the Atmosphere to Electrons Mesoscale-to-Microscale Coupling Project

Year 3 Report

December 2017

SE Haupt[1]
L Berg[2]
M Churchfield[3]
C Kalb[1]
B Kosović[1]
L Mazzaro[5]
E Quon[3]
G Sever[4]
A Anderson[1]
B Brown[2]
C Draxl[3]
E Koo[4]
R Kotamarthi[5]
J Mirocha[6]
R Rai[2]

Prepared for
the U.S. Department of Energy
under Contract DE-AC05-76RL01830

Pacific Northwest National Laboratory
Richland, Washington 99352

---

[1] National Center for Atmospheric Research (NCAR)
[2] Pacific Northwest National Laboratory (PNNL)
[3] National Renewable Energy Laboratory (NREL)
[4] Los Alamos National Laboratory (LANL)
[5] Argonne National Laboratory (ANL)
[6] Lawrence Livermore National Laboratory (LLNL)

Summary

The goal of the mesoscale-to-microscale coupling (MMC) project is to build new high-performance-computing-based multiscale wind-plant simulation tools that couple a broad range of scales to enable the optimization of wind plants to ensure the efficient, reliable production and integration of future wind-generated electricity. To meet this goal, the project seeks to create, assess, and validate state-of-the-science atmospheric simulation methodologies to incorporate important mesoscale flow characteristics into microscale wind-plant simulations.

The third year of the project (fiscal year 2017 [FY17]) focused on:

- documenting and assessing the impacts of modeling at the mesoscale in the *terra incognita*—the modeling range in which neither the mesoscale nor the microscale models fully apply—including providing recommendations;
- assessing methods for initiating turbulence in microscale simulations;
- exploring methods to better represent the surface layer; and
- evaluating the turbulence statistics for model case studies in complex terrain.

The project team documented the fact that the upper limit of the *terra incognita* range should be based on the depth of the boundary layer. It also showed the importance of including a mesoscale nest, which leads to more realistic simulations in the flow simulated with the microscale model. Further, the results also suggest that the impact of mesoscale domains with grid spacing in the *terra incognita* do not have a large impact on the microscale results, but this finding does not agree with other recent studies, indicating that more study is required. Other recommendations from the work are that users should avoid mesoscale domains that employ grid spacing smaller than the boundary-layer depth due to unrealistic features in the flow; the choice of boundary-layer parameterization may not be critical to model results; and users should use fully coupled simulations that employ mesoscale nests, rather than driving microscale simulations with large-scale reanalysis products, in order to maintain a more realistic energy profile.

Studies of modeling in the *terra incognita* in complex terrain using cases selected from the Wind Forecast Improvement Project 2 (WFIP 2) indicate that rolls formed in the simulations were realistic rather than spurious as was found in the flat-terrain cases modeled previously. We hypothesize that complex terrain forces waves at realistic frequencies, avoiding the numerically generated ones. This result was supported by the formal assessment, which showed that model resolutions in the *terra incognita* more correctly captured wind features.

Several different methods were examined to accelerate the development of turbulence within large-eddy simulations (LES) in general settings that do not permit the traditional method of using periodic lateral boundary conditions. Two methods based on using precursor simulations to generate turbulent inflow for LES, and three methods based on perturbing smooth mesoscale inflow upon its entry into the LES domain were evaluated. One precursor method used a periodic LES driven by mesoscale forcing parameters to provide turbulent inflow to an offline microscale simulation over complex terrain. This approach was successfully applied over complex terrain at the WFIP 2 site, showing great promise as a means of providing instantaneous turbulent inflow. A second method involved saving the precomputed fields in a library, thereby saving computational expense. A prototype of such a library, and a second technique for integrating the library files into an offline LES—, asynchronous coupling—was also examined by producing 108 LESs over a range of wind speeds, temperatures, surface roughnesses, and model resolutions, based upon a neutral boundary-layer case study from the Scaled Wind Farm Test (SWiFT) facility. Incorporation of flow from the precomputed turbulence fields into an offline LES via the

asynchronous coupling procedure was attempted, but problems were encountered with the idealized open lateral boundary conditions used within the offline LES.

Incorporating inflow perturbations was also examined using two synthetic approaches based upon the spectral perturbations created with TurbSim and the Gabor kinematic simulation (KS) method. Simulations using each method produced turbulence rapidly at the LES inflow boundary, but each method produced anomalous turbulence kinetic energy (TKE) characteristics relative to a reference simulation. TKE using the TurbSim method nearly equilibrated after about 4 km of fetch, thereafter gradually decreasing with further distance, while that using the Gabor KS method exhibited a long-term high-amplitude oscillation that never equilibrated. The synthetic approaches were also used to investigate the impacts of turbulence on turbine-relevant quantities of interest characterizing machine performance and fatigue loading, via coupling the microscale flow field to the Fatigue, Aerodynamics, Structures, and Turbulence (FAST) aeroelastic model.

An alternative method to instigating turbulence development on LESs, the stochastic cell-perturbation method (SCPM), was also examined, this time in real-data case studies involving full physics multiscale MMC simulations conducted within the Weather Research and Forecasting (WRF) model. The SCPM used herein was modified to run concurrently with the nested LES domains and was examined over a case study consisting of a diurnal cycle at the flat-terrain SWiFT facility, simulated both with and without the SCPM. Simulations revealed that the SCPM neither improved nor degraded the simulations during the late morning to midafternoon hours, because of strong convective conditions leading to rapid turbulence generations via surface buoyancy. However, the SCPM considerably improved the representation of turbulence during the neutral and stable conditions later in the afternoon and overnight. The SCPM was also applied to a case study from the complex terrain WFIP 2 site, where it again was shown to accelerate the development of turbulence.

Application of perturbations to velocities was also investigated. Perturbations to the horizontal and vertical velocity components were shown to produce faster equilibration of some turbulence parameters than the thermal perturbations, and vertical velocity components produced the fastest equilibration. However, other quantities were better matched by the thermal perturbations. The investigations suggest that a combination of velocity and thermal perturbations could perform better overall than either method alone. Each of the turbulence-generation methods investigated during FY17 shows promise for specific applications and is worthy of continued development.

Three different explicit canopy physics modules were examined to increase the fidelity of surface- and boundary-layer flow in LES. These parameterizations augment or replace the standard Monin-Obukhov similarity theory (MOST) that is commonly used in atmospheric LES, despite its tenuous applicability to turbulence resolving flows in unsteady, heterogeneous settings.

Two canopy models were implemented into the WRF model—an explicitly resolved canopy for canopy elements taller than the vertical resolution of the LES and a pseudo-canopy model for surfaces characterized by small canopy elements. The explicitly resolved canopy implementation was validated against a test case from the literature, consisting of a horizontally homogeneous canopy with height variability representing a forest. WRF can now recover correct velocity and turbulence characteristics over tall vegetated canopies. Following the implementation of the explicit canopy model, a pseudo-canopy model using concepts from the explicit canopy, but tailored for smaller roughness elements, was developed. Simulations with the pseudo-canopy model over flat terrain with small roughness lengths produced significant improvements in the vertical distributions of velocity and turbulence characteristics relative to the standard MOST implementation, showing great promise for microscale wind-energy applications. A heterogeneous canopy model, which resolves individual trees in the horizontal direction, was also examined within the HIGRAD model, likewise showing applicability to wind-energy simulations in regions characterized by patchy vegetation. The canopy models implemented in the WRF model can also accommodate horizontal heterogeneity in canopy features, for which the HIGRAD simulations could provide useful validation data.

Formal assessment was accomplished for a complex terrain case from the WFIP 2 observational experiment using observations at the Physics Site for November 21, 2016. This case study was characterized by topographic wake and mountain waves over the area. The MMC simulation was carried out using WRF's nesting capability; the parent nest was run in mesoscale mode while two inner nests were run in LES mode. During the period between 19:00 and 21:00 Coordinated Universal Time (UTC), the wind speed error was up to 6 m s^{-1}. Turbulent sensible heat flux was predicted quite well except during a period of relatively short intervals when the model did not accurately capture cloud cover. Spectral analysis shows excellent agreement between measured and simulated turbulence frequency spectra in the well-resolved portion of the inertial range. Good agreement indicates that even when the mesoscale flow is not captured accurately, the turbulent energy transfer from large turbulent production scales to smaller scales can be represented accurately in a well-resolved LES. The assessment of MMC within a single model confirms the feasibility and validity of the approach that relies on online coupling within the same model.

Acknowledgments

The MMC project is supported at the participating laboratories by the Wind Energy Technologies Office within the U.S. Department of Energy's (DOE's) Office of Energy Efficiency and Renewable Energy through the Atmosphere to Electrons program. The collaborators on this project also thank Texas Tech University for providing the high-quality atmospheric data set from DOE's SWiFT facility.

Acronyms and Abbreviations

A2e	Atmosphere to Electrons (Initiative)
ANL	Argonne National Laboratory
CC	correlation coefficient
CDT	Central Daylight Time
CST	Central Standard Time
DAP	Data Archive and Portal
DOE	U.S. Department of Energy
GFS	Global Forecast System
HFM	high-fidelity modeling
HPM	high-performance modeling
HRRR	High-Resolution Rapid Refresh (model)
IEC	International Electrotechnical Commission
KS	kinematic simulation
LANL	Los Alamos National Laboratory
LLNL	Lawrence Livermore National Laboratory
LES	large-eddy simulation
LLJ	low-level jet
LST	local standard time
MAE	mean absolute error
ME	mean error
MMC	mesoscale-to-microscale coupling
MOST	Monin-Obukhov similarity theory
MSL	mean sea level
MYNN	Mellor-Yamada-Nakanishi-Niino
NBA	nonlinear backscatter and anisotropy
NCAR	National Center for Atmospheric Research
NOAA	National Oceanic and Atmospheric Administration
NREL	National Renewable Energy Laboratory
PBL	planetary boundary layer
PCM	pseudo-canopy model
PNNL	Pacific Northwest National Laboratory
QOI	quantity of interest
RMSE	root mean squared error
RMSD	root mean squared difference
SCPM	stochastic cell-perturbation method

SGS	subgrid-scale
sodar	sonic detection and ranging
SOWFA	Simulator fOr Wind Farm Applications
SWiFT	Scaled Wind Farm Test
3-D	three-dimensional
TKE	turbulence kinetic energy
UTC	Coordinated Universal Time
V&V	verification and validation
WFIP 2	Wind Forecasting Improvement Project 2
WRF	Weather Research and Forecasting
YSU	Yonsei University
z_i	boundary-layer depth

Contents

Figures

Tables

1.0 Introduction

1.1 Mesoscale-to-Microscale Coupling Project

The goal of the Mesoscale-to-Microscale Coupling (MMC) project is to build new high-performance-computing-based multiscale wind-plant simulation tools by coupling a broad range of scales that will enable the optimization of wind plants, thereby ensuring the efficient, reliable production and integration of future wind-generated electricity.

The overarching objective of the project is the creation, assessment, and validation of state-of-the-science atmospheric simulation methodologies to incorporate important mesoscale flow characteristics into microscale wind-plant simulations. MMC project objectives include the following:

- Compare the abilities of existing physics models to fully characterize the meso/micro planetary boundary-layer (PBL) characteristics, including plant inflows, wake flows, and interactions with the boundaries. Identified deficiencies will provide the rationale for the next steps for model improvement.
- Establish field data baseline cases as part of the verification and validation process for existing models. Thus, improvements can be grounded in data.
- Downselect from the existing modeling suite for future implementation to improve development efficiencies using a common high-fidelity modeling (HFM) framework. This process will enable development of a tool that is usable by industry.
- Establish research and development requirements to improve PBL model performance. This initiative will identify specific areas for improvement and examine how they will affect the microscale modeling initiative in the HFM environment.
- Advance development issues including nonstationarity, boundary interactions, coupling strategies, *terra incognita* issues, and modeling in complex terrain. It is necessary to improve in all of these issues if the HFM framework is expected to correctly represent critical mesoscale forcings.
- Transition existing model and physics requirements to the HFM development environment, working closely with the HFM team.

Realizing these objectives will enable simulation of the full suite of mesoscale and microscale flow characteristics affecting turbine and wind-plant uncertainties and performance, thereby allowing for substantive improvements in wind-plant design, operation, and performance projections. **Error! Reference source not found.** diagrams the MMC approach to the project, taking into account the objectives described above.

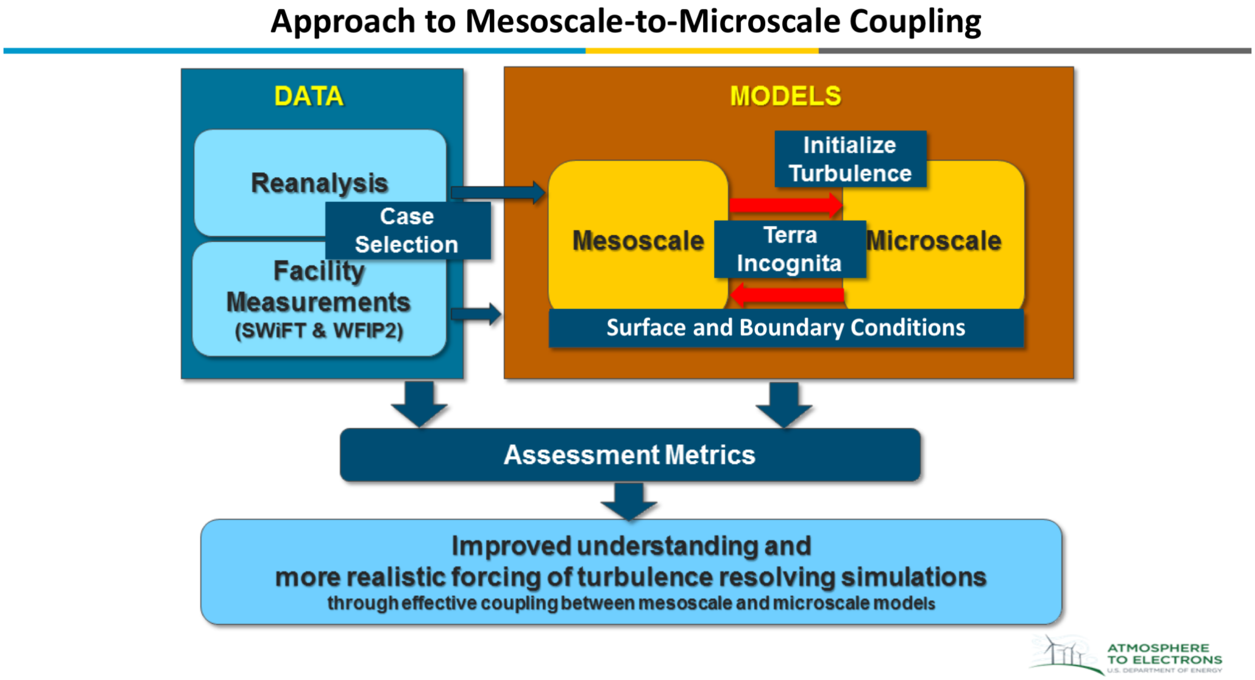

Figure 1.1. Diagram of the MMC project approach.

1.2 Mesoscale-to-Microscale Coupling Project Context within the Atmosphere to Electrons Initiative

The Atmosphere to Electrons (A2e) Initiative is an effort within the Wind and Water Power Technologies Office of the U.S. Department of Energy’s (DOE’s) Energy Efficiency and Renewable Energy Office. The goal of this initiative is to optimize power production from wind plants as a whole. To that end, the initiative is explicitly integrating advances in atmospheric sciences, wind-plant aerodynamics, and wind-plant control technologies, taking advantage of current and emerging capabilities for high-performance computing. Because atmospheric inflow is the fuel that powers wind plants—containing both the energy available for conversion into electricity as well as characteristics that modulate that conversion—the development and validation of first-principles based, high-fidelity physics models within an open-source simulation environment have been identified as a crucial part of A2e science goals and objectives. Furthermore, there has been an overwhelming consensus within the research community that these models must be developed and systematically validated using a formal verification and validation (V&V) process. The MMC project was intended to provide an initial demonstration of the V&V-guided approach to model development specifically applied to the mesoscale-microscale coupling problem and to provide the foundation for the ultimate selection of a common framework for the development of atmospheric and wind-plant modeling within the A2e Initiative. It has been a joint collaborative project between six DOE national laboratories with leadership from National Center for Atmospheric Research (NCAR), the formal subcontractor. The project incorporates external feedback from A2e Initiative team members (Argonne National Laboratory [ANL], Lawrence Livermore National Laboratory [LLNL], National Renewable Energy Laboratory [NREL], Pacific Northwest National Laboratory [PNNL]), industry, DOE leadership, and other stakeholders.

The MMC project is grounded in data provided by other A2e facilities and projects. For the first two years, the data have included measurements taken at the DOE/Sandia National Laboratories Scaled Wind

Farm Test (SWiFT) facility in West Texas. The MMC modeling has helped characterize and inform the wake dynamics experiments conducted at that site and its results are expected to contribute to modeling wake dynamics.

In year 3, the MMC project has focused on coupled modeling in complex terrain, using data derived from the observations taken in the Pacific Northwest as part of the A2e project, Wind Forecasting Improvement Project 2 (WFIP 2). Including mesoscale forcing in microscale models will also become critical to the success of the A2e project when focusing on wind-plant controls. Most prominently, the very specific coupling and modeling philosophies and technologies being developed by the MMC project are necessary for building the HFM tools. The results of MMC modeling and case studies are being archived in DOE's Data Archive and Portal (DAP).

1.3 Progression of the Mesoscale-to-Microscale Coupling Project

The MMC project was designed to systematically progress from simulation of canonical quasi-steady cases through the full complexity of nonstationarity and complex terrain. The plans are grounded in V&V based on comparing model cases to observations. Specifically, the plans for the first three years of the project were as follows:

- **FY15:** Couple mesoscale-to-microscale models for canonical steady flow conditions to include neutral, stable, and convective conditions for flat terrain and compare simulations to SWiFT site measurements.
- **FY16**: Couple mesoscale-to-microscale models for nonstationary conditions over the flat-terrain SWiFT site, devise coupling strategies in which mesoscale forcing causes microscale models to follow through the temporal changes, and compare to SWiFT site measurements of winds and turbulence.
- **FY17:** Couple mesoscale-to-microscale models for representative meteorological conditions occurring over a complex terrain site, where mesoscale forcing causes microscale models to follow through the temporal changes, and compare to WFIP 2 site measurements.

An overarching goal for the first three years has been to downselect which models and mesoscale-microscale coupling techniques to implement within the HFM environment. Downselection of the computational solvers was accomplished—the mesoscale model will be the Weather Research and Forecasting (WRF) model and the microscale model will be the Nalu model.

During each of the three project years, four specific objectives have been addressed: (1) to define V&V procedures and benchmarks, (2) to develop and assess microscale turbulence-generation methods, (3) to assess current surface-layer and boundary-layer parameterizations, and (4) to develop and assess approaches for coupling mesoscale models to microscale models.

Beyond fiscal year 2017 (FY17), the MMC project team expects to continue to add complexity; explicitly compare microscale simulations with and without mesoscale forcing, focusing on metrics important to wind plan operation; feed findings into low-order models that can be used rapidly by industry; improve turbulence models for industry; work with the HFM team to provide fast mesoscale modeling capabilities and couple them to the Nalu model; and feed the results into other A2e projects including controls and others. **Error! Reference source not found.** summarizes the project progression.

Table 1.1. Details of MMC project progression and milestones.

Fiscal Year	FY15		FY16				FY17			
Milestone	Q3	Q4	Q1	Q2	Q3	Q4	Q1	Q2	Q3	Q4
Case Selection										
Select Canonical Cases at SWiFT Site	⬛									
Select Nonstationary Cases at SWiFT Site				⬛						
Characterize SWiFT Site	🟩	🟩	🟩	🟩	🟩	🟩				
Select Complex Terrain Cases from WFIP2 Site							⬛			
Downselect Mesoscale Models										
WRF Model/Physics Sensitivity	🟦	🟦	🟦	🟦	🟦	🟦				
WRF Model/Boundary Conditions Sensitivity	🟦	🟦	🟦	🟦	🟦	🟦				
WRF Model/Grid Resolution Sensitivity	⬛	⬛	⬛	⬛	⬛	⬛				
MPAS Model/Suitability for Mesoscale Simulations				🟧	🟧	🟧				
Development of Evaluation Metrics/Evaluation	🟥	🟥	🟥	🟥	🟥	🟥				
Mesoscale Model Selection						⬛				
Downselect Microscale Models										
WRF-LES/Steady State	🟥	🟥	🟥	🟥	🟥	🟥				
WRF-LES/Neutral				🟧	🟧	🟧				
	🟥	🟥	🟥	🟥	🟥	🟥				
SOWFA/Steady State	🟦	🟦	🟦	🟦	🟦	🟦				
SOWFA/Neutral	🟦	🟦	🟦	🟦	🟦	🟦				
HIGRAD	🟨	🟨	🟨	🟨	🟨	🟨				
Development of Evaluation Metrics/Evaluation	🟥	🟥	🟥	🟥	🟥	🟥				
Model Selection/WRF-LES & NALU						⬛				
Test Microscale Model/Forcing strategies										
WRF-LES/Fixed Geostrophic Forcing	🟥	🟥	🟥	🟥	🟥	🟥	🟥	🟥		
WRF-LES/Tendency Forcing	🟥	🟥	🟥	🟥	🟥	🟥	🟥	🟥		
SOWFA	🟦	🟦	🟦	🟦	🟦	🟦	🟦	🟦		
Selection of Forcing Strategy									⬛	
Testing *Terra incognita* Modeling Strategy										
WRF – Multiresolution Modeling			🟦	🟦	🟦	🟦	🟦	🟦		
			🟦	🟦	🟦	🟦	🟦	🟦		
Group Recommendation										⬛
Complex Terrain Modeling/Evaluation										
WRF-LES								🟥	🟥	🟥
								🟦	🟦	🟦
								🟧	🟧	🟧
NALU/SOWFA								🟨	🟨	🟨

Fiscal Year	FY15		FY16				FY17			
								🟦	🟦	🟦
Development of Metrics/Case Studies/Evaluation								🟥	🟥	🟥
Recommend Best Practices										⬛
Test Coupling Strategies										
WRF-LES/WRF Online						🟫	🟫	🟫	🟫	🟫
						🔷	🔷	🔷	🔷	🔷
WRF-LES/WRF Offline									⬛	⬛
WRF-LES/Asynchronous									🟧	🟧
NALU/ WRF Offline-Coupling/Forcing Strategy									🟦	🟦
									🟨	🟨
Development of Metrics for Evaluation/Evaluation									🟥	🟥
Coupling Strategy Recommendation										⬛
Recommend Best Practices										⬛

Color Key

⬛	All	🟦	National Renewable Energy Laboratory (NREL)
🟥	National Center for Atmospheric Research (NCAR)	🔷	Pacific Northwest National Laboratory (PNNL)
🟧	Argonne National laboratory (ANL)	🟨	Los Alamos National Laboratory (LANL)
🟫	Lawrence Livermore National Laboratory (LLNL)	🟩	Sandia National Laboratories (SNL)

1.4 Expected Impacts on Industry

The overall impact of the MMC project is to advance the science and engineering of coupled mesoscale-microscale modeling in order to provide industry with more advanced wind-plant optimization capabilities. Industry stakeholders have made it clear what must be done in terms of better modeling of power output. This issue is complex and involves many factors beyond applying a simple power curve to a simulated mean wind speed and making small adjustments for turbulence. Uncertainties come from many different aspects of the coupling, including interannual variability due to longer-term climatic variability, variability in the outer scales that are resolved by the mesoscale models, variability due to wake effects, inner variability due to the heterogeneity within the wind plant, variability due to coherent structures, inherent uncertainty due to the chaotic nature of turbulent flow, and, finally, impacts through the surface-layer treatment and its interactions with characteristics of the underlying surface. The MMC project addresses these issues directly and, over the course of the multiyear project, will be able to provide specific guidance to DOE in industry. The MMC team developed **Error! Reference source not found.** as a list of uses of the MMC approach, the stakeholder(s), quantities and metrics to assess for each use, and the type of uncertainty analysis that will affect power output.

Table 1.2. Assessment of stakeholder use and assessment strategies to determine if MMC modeling provides useful information for that use.

MMC Use	Stakeholder	Quantity to Measure	Metrics	Uncertainty Analysis for Power Curve
Basic understanding of physics	Scientists, Engineers	Current list plus elevated structures	Current list plus below	Ensembles—physics, initial and boundary conditions
Micrositing	Developers, Contractors, Manufacturers	Binned wind speed, spectra, spatial variability	Probability structures and spatial correlations	Distributions, correlations, spatial correlations, covariance
Turbine siting	Developers, Contractors, Manufacturers	Binned wind speed, spectra, spatial variability	Probability structures and spatial correlations	Distributions, correlations, spatial correlations, covariance
Turbine reliability and design plus forensics		Turbine statistics, shear, coherent structures	Correlated structures to loads	Distribution extremes, wind direction variability
Operations and managements, controls, loads		Slow variations, event variations, binned wind speed, accurate turbulence statistics plus characterization of structures	Use spatial and temporal filters	Time-dependent statistics and variability
Inform low-order models: mass conserving models, Reynolds-averaged Navier-Stokes	Developers, Contractors, Original Equipment Manufacturers	Three-dimensional wind speed, TKE, and surface fluxes	Spatial correlations	All

Both the improved computational methodologies and the knowledge gained through their assessment and validation will enable substantive improvements in wind-plant design, operation, and performance projections, all of which are required to attract continued investment in wind power as a viable means of meeting national goals of mitigating climate change and establishing energy independence.

The successful outcome of the MMC project will result in improved computer simulation capability that accurately incorporates the impact of mesoscale weather on wind power plant performance. Meeting this goal will require microscale simulations driven by realistic mesoscale forcing, knowledge of when the additional complexity of mesoscale coupling is beneficial, and recommendations for best practices for modeling across spatial and temporal scales. Over the course of this project, the tools and knowledge developed during each phase—which are outlined above—will continue to be made available to industry and the broader research community. Experimental inputs and numerical results will be made available via the DOE DAP.

The MMC team has engaged with industry by participating in the first-year workshop held in September 2015 at NCAR, at which industry representatives were invited to comment on the approach and the results as well as to suggest changes. In FY16, the MMC team conducted an industry survey. During FY17, the team conducted a telecom with industry to inform them of our progress and solicit input.

MMC team members have also been actively engaged in organizing major wind industry conferences that were used as forums for bringing the research community together with industry. This was successfully accomplished at the International Conference on Energy and Meteorology held in Bari, Italy, in June 2017 and at WindTech 2017 held in Boulder, Colorado, in October 2017. Both of these meetings included presentations about the MMC project and afforded ample opportunity for industry representatives and team members to discuss the team's progress and plans. The team also connected with industry personnel at the Annual Meeting of the American Meteorological Society, American Geophysical Union, and North American Wind Energy Academy. Going forward, the team plans to increase the number of telecons with industry and maintain that communication to assure that the research is pointed in the most relevant directions to provide the greatest benefit to industry.

As described in more detail in the sections that follow, each of the models and techniques we used are validated against a range of metrics to determine their accuracy for a mix of wind-energy-related applications. A key outcome of this project is the generation of concrete guidance to both industry and research communities regarding the potential strengths and weaknesses of various MMC approaches. Additionally, the best performing of the approaches assessed will be incorporated into the A2e high-performance modeling (HPM) environment for future design and testing. A set of metrics defined by the project continues to be refined further as the project progresses into additional modeling realms and increasingly complex cases.

1.5 Background and Motivation

This work is motivated by the fact that the current generation of tools is insufficient to adequately simulate winds and turbulence on all of the atmospheric scales that drive wind-plant performance. This project has brought together a team of subject-matter experts to address these modeling gaps. It is widely reported that many wind plants in complex operating environments continue to underperform by 30–40% relative to annual production estimates. According to a survey conducted by AWS Truepower, LLC (Bailey 2013), the three largest factors contributing to performance losses, as well as four of the eight uncertainty sources, are affected by the quality of the numerical simulation tools used for turbine and wind-plant performance estimates.

A significant fraction of wind-plant underperformance and uncertainty can be attributed to design, siting, and operational strategies based upon inaccurate assessment of environmental conditions, as well as underestimation of the importance of environmental (mesoscale) influences at the sites where wind turbines operate. Wind turbine design, plant construction, and operations all rely on a suite of simulation design tools of varying levels of complexity and fidelity, each targeting different phases of wind-energy planning, deployment, and production. These computational tools span a range of applications including flow characterization, power production, fatigue loading, wake effects, and the impacts of complex terrain (e.g., Shaw et al. 2009).

Crucially, these tools all lack the ability to adequately address the impacts of the complexity of the mesoscale flow and the physical understanding and modeling of the weather phenomena that strongly influence turbine operation (Sanderse et al. 2011; Troldborg et al. 2011; Mehta 2014). Although recent advances have been made in the engineering models used to estimate wakes and loads and examine control strategies to improve plant production or mitigate fatigue (e.g., the National Renewable Energy

Laboratory's [NREL's] Simulator fOr Wind Farm Applications [SOWFA] and Fatigue, Aerodynamics, Structures, and Turbulence [FAST] toolkits; Los Alamos National Laboratory's [LANL's] WindBlade model), the range of atmospheric conditions represented within their simulation frameworks is limited. Further rationale and details of the needs are described in the report documenting the results of the first- and second-year efforts of the MMC team (Haupt et al. 2015, 2017).

One difficulty with MMC is that it bridges a wide span in spatial and temporal scales. Mesoscale models were designed for horizontal resolutions on the order of kilometers with time scales ranging from days to hours. Microscale models have resolutions on the order of multi-meters (i.e., from 10 m down to a couple of meters is common), depending on the atmospheric stability and desired resolution, and they resolve time scales ranging from hours to seconds. Spanning these scales involves resolving a wide range of disparate phenomena and turbulence that have different fundamental characteristics.

Examples of wind-energy applications benefiting from MMC include single wind turbine loads, power, and controls estimation (by creating more realistic microscale inflow under a variety of conditions for turbine simulators); wind-plant siting (by providing more site-specific inflow profiles under the full diurnal cycle in different seasons or terrain-induced flow behavior); wind-plant power forecasting and operation (through higher resolution wind-plant-local forecasting); wind-plant-level control system design (by testing these controls under more realistic mesoscale-forced situations rather than just applying simple canonical cases); and wake modeling (through microscale wake simulations in more realistic situations than the canonical ones). All such applications have differing needs for representations of the microscale.

For example, it is possible that for load analysis, the primary factor is employing more realistic mean wind profiles forced by the mesoscale as opposed to the power or log-law typically used today. Having site-specific profiles from different times of day and different types of common mesoscale-driven events could greatly improve load calculations. On the other hand, performing forensics to determine why certain turbines failed during a mesoscale weather event will likely require a sophisticated mesoscale-microscale coupled simulation. Wind-plant controls experts have been requesting more realistic mesoscale-forced microscale inflow to study because they realize that canonical microscale inflow may not rigorously exercise their control systems. Also, industry experts note that the current frameworks are not sufficient. This MMC project is directly addressing these known deficiencies common to industry research and design tools by assessing and validating mesoscale-microscale coupling strategies.

Thus, MMC is a key enabling technology required for the replacement of many of the inadequate idealizations and simplifications limiting the applicability of current microscale simulation tools. MMC will replace them with environmental forcing obtained from mesoscale simulations. Incorporation of these important environmental drivers will enable simulation of critical microscale flow characteristics that affect turbine and wind-plant performance and uncertainties.

1.6 FY17 Emphasis: Coupling for Complex Terrain

Mesoscale-microscale coupling presents the most promising approach to addressing the key limitations of current wind-plant simulation techniques. The MMC project has been evaluating and developing methods and tools to replace the existing highly idealized or steady-state forcing parameters, periodic lateral boundary conditions, and other simplifications typically employed in wind farm simulation tools. The key to these improved methods is dynamic input from mesoscale weather models that can provide important meteorological, topographical, and other environmental drivers of microscale variability.

During FY17, the emphasis of the MMC project has been on applying our coupling methods to complex terrain problems. The meteorology over complex terrains can be quite complicated—well beyond the obvious inhomogeneous nature of the lower boundary condition. During stable conditions, cold pools commonly form in the pockets between the mountains. The breakup of these cold pools depends on various meteorological features beyond just the changes in heating, which include shadowing effects, and also depends on the conditions being advected into the region, including the passage of weather patterns. In addition, the terrain generates topographic wakes and waves. During some conditions, hydraulic jumps occur, which depend on the baroclinicity that can be modeled with the mesoscale models. **Error! Reference source not found.** shows clouds visualizing the waves generated by the topography in the Pacific Northwest. Thus, a goal of project efforts during FY17 was to study the impact of coupling the mesoscale models to the microscale models and determining to what extent we can capture these complex features that will modify the energy available at wind farms.

Figure 1.2. Waves in the lee of mountains in the Pacific Northwest. (Photo credit: Jeff Mirocha)

To test the coupling methods for complex terrain, the team used measurements from the WFIP2 project. The data available from that experimental campaign provided the observations required to assess and fine-tune coupled model performance for this challenging environment as described later. Section 4.1 describes the specific cases chosen.

1.7 Report Contents and Organization

The remainder of this report provides detailed documentation of the results of the MMC project's third-year effort. The performance metrics were defined at the beginning of the project and updated as needed for these complex terrain cases to assess the phenomena mentioned above. The need for uncertainty quantification has been an intentional part of the metrics development and plans for model runs in the future.

Chapter 2 documents the FY17 work accomplished regarding the impact of the *terra incognita* on modeling and assessment of the modeling results both inside and outside that range. This assessment continues the work of year 2 and considers nonstationary cases in flat terrain, then progresses to complex terrain cases. Chapter 3 reports on findings regarding generating turbulence in the microscale simulations for the complex terrain cases. Evaluation of turbulence statistics is described in Chapter 4. Chapter 5 compares modeling results using different surface-layer schemes. Chapter 6 synthesizes the results and their expected impact. Appendix A lists the team's FY17 contributions to the peer-reviewed literature and conference papers presented on behalf of the MMC team. Appendix B details each lab's contributions to the FY17 efforts.

2.0 The Impact of *Terra incognita*

The MMC team began investigating the impact of the *terra incognita* on coupled modeling during FY16, the second year of the project, by modeling flow at differing resolutions (see the report about the second-year work [Haupt et al. 2017, Chapter 4]). The team found evidence of impacts related to *terra incognita* issues using traditional subgrid-turbulence closure approaches in the mesoscale simulations from about a 1-km resolution and finer. The "noise" in the wind speed (vertical and horizontal), turbulence kinetic energy (TKE), momentum flux, and temperature indicated these issues. Planar plots displayed increasing spurious rolls in simulations at 333-m and, to a lesser extent at 1-km spacing, when the Mellor-Yamada-Nakanishi-Niino (MYNN) boundary-layer scheme was used, but less so for the Yonsei University (YSU) scheme. Note that the investigation of *terra incognita* issues was conducted in coordination with A2e-supported development (via WFIP 2) of appropriate turbulence closure techniques for that range of scales, and that examination of those closures in the context of MMC is proposed as future work.

As documented in this report, the work progressed by further studying the impact of the *terra incognita* on the microscale flow in flat terrain (Section 2.1) and in complex terrain (Section 2.2). Formal verification accomplished for complex terrain is presented in Section 2.3.

2.1 Investigation of the Impact of the *Terra incognita* on Microscale Simulations

Wyngaard (2004) defined meteorological *terra incognita* as the range of spatial scales for which a weather forecast model, such as the WRF model, using traditional boundary-layer parameterizations begins to fail and the model erroneously simulates coherent structures in the boundary layer. A number of studies (e.g., Honnert et al. 2011; Shin and Hong 2013; Ching et al. 2014; Shin and Dudhia 2016; Rai et al. 2017) presented results showing spurious features in the simulated flow when the horizontal grid spacing fell within the *terra incognita*, but they did not investigate the impact of these features on microscale domains that use associated mesoscale domains to provide time-varying boundary conditions. To address these shortcomings, the MMC team conducted a detailed study designed to provide guidance related to the best configuration of mesoscale domains and the impact of grid spacing in the *terra incognita* on microscale simulations. In this first section, we focus on results in flat terrain and compare simulations to data recorded at the SWiFT site in Texas.

2.1.1 Model Configuration

A suite of simulations with a range of grid spacings were completed using the WRF model in both mesoscale and microscale modes with horizontal grid spacing ranging from 3.84 to 0.04 km for four cases. The cases focused on conditions at the SWiFT facility for four days with different simulated boundary-layer depths (z_i). All told, 10 different grid configurations were tested that applied different grid spacing, grid refinement ratios, and turbulence parameterizations, as listed in Table 2.1 and shown in a map of the various domains in Figure 2.1. The grid sizes remained the same size regardless of the horizontal grid spacing, leading to differences in the number of grid points used in the different cases. Simulations were completed using one of three commonly used turbulence parameterizations: MYNN (Nakanishi and Niino 2009), YSU (Hong et al. 2006), or Lilly (Lilly 1967). The MYNN and YSU parameterizations are commonly used one-dimensional parameterizations applied in mesoscale simulations. The Lilly parameterization is three-dimensional (3-D) and is typically used for large-eddy simulation (LES) applications. In this report, the turbulence parameterization used for the specific domains of interest are added to the name of the model configuration. For example, Ti2-0.24km Myn-

Myn indicates the Ti2 domain with 0.24-km grid spacing and application of the MYNN parameterization on both domain 1 and domain 2.

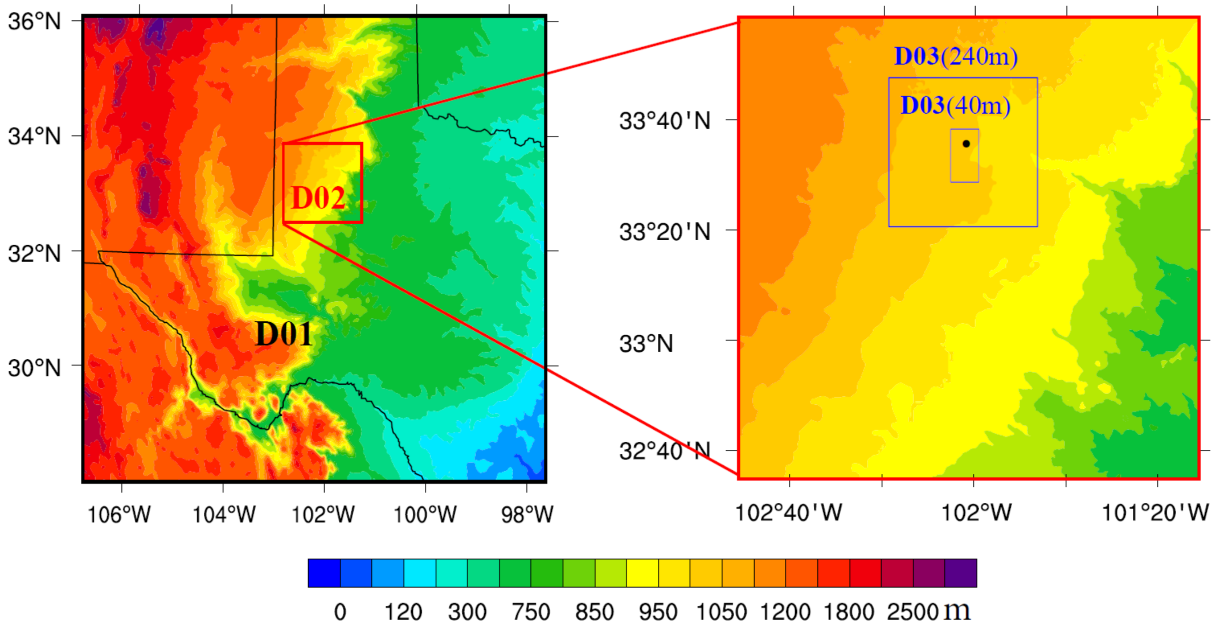

Figure 2.1. Terrain height (colors) and model domains D01-D03. Note the two different configurations for domain 3, one with horizontal grid spacing of 0.04 and 0.24 km as indicated on the figure. The black dot in domain 3 shows the location of the Texas Tech University tower at the SWiFT site.

Table 2.1. WRF/WRF-LES domains for the study, including run identification; grid spacing of domains 1, 2, and 3; z_i; and simulation date. Ti indicates runs in which at least one domain had horizontal grid spacing in *terra incognita*, and boldface type indicates domains with grid spacing greater than z_i.

Run	D01 Grid Spacing (km)	D02 Grid Spacing (km)	D03 Grid Spacing (km)	z_i (km)	Date
Ti1	**2.88**	1.44	0.24	2.4	6/12/13, 6/14/14
Ti2	**3.84**	0.96	0.24	2.4	6/12/13, 6/14/14
Ti3	**2.88**	0.48	0.24	2.4	6/12/13, 6/14/14
Ti4	**2.56**	0.32	0.04	2.4	6/12/13, 6/14/14
Ti5	**2.52**	0.28	0.04	2.4	6/12/13, 6/14/14
Ti6	2.40	0.24	0.04	2.4	6/12/13, 6/14/14
Ti7	2.20	0.2	0.04	2.4	6/12/13, 6/14/14
R1	0.04	—	—	2.4	6/12/13, 6/14/14
R2	1.50	—	—	1.5	9/22/13
R3	3.20	—	—	3.2	7/13/13

2.1.2 Analysis

One of our hypotheses is that issues associated with the *terra incognita* should appear as the model grid spacing approaches z_i, and this was confirmed using the suite of simulations. Figure 2.2 shows results for simulations completed for 12 June 2013, 22 September 2013, and 13 July 2013. Convective conditions were simulated for each day, but the midafternoon values of z_i were 2.4, 1.5, and 3.2 km, respectively. The top row of panels in Figure 2.2 shows the results for grid spacings of 3.2, 2.4, and 1.6 km, respectively. At the coarsest grid spacing, there is no evidence of unrealistic flow structures and the simulated winds are fairly uniform in time. As the grid spacing is changed to 2.4 km, however, anomalous flow features begin to appear that grow larger as the horizontal grid spacing is further reduced to 1.6 km. This can be seen in the large oscillations of the simulated wind speed for grid spacings of 2.4 and 1.6 km. Consistent results are found for the case in which the midafternoon value of z_i is 2.3 km. In this case, oscillations are only apparent for the domain with the grid spacing of 1.6 km, but the flow is more constant in time for the simulation with the grid spacing of 2.4 km. For the case with the smallest value of z_i, no oscillations are apparent, even when the grid spacing of 1.6 km is used. These results highlight how important it is to select horizontal grid spacings greater than the anticipated value of z_i when configuring mesoscale domains.

Analysis of the auto-spectral density function paints a similar picture; spurious energy associated with mesoscale simulations that use horizontal grid spacing less than z_i are shown in Figure 2.3 and provide more evidence of the impact of *terra incognita* on the simulated flow. For grid spacings larger than z_i, the energy associated with the horizontal (*u*) and vertical (*w*) velocity components is quite small, regardless of the exact grid spacing (Figure 2.3a and b). For grid spacings of 0.96 km and smaller, the WRF simulations completed using the MYNN parameterization have an order of magnitude more energy than similar runs using the YSU boundary-layer parameterization (note the differences in Ti2-0.96km Myn-Myn and Ti2-0.96km Ysu-Ysu found in Figure 2.3c and d). As the grid spacing is reduced further, the difference between the two simulations shrinks (Ti2-0.24km Myn-Myn and Ti2-0.24km Ysu-Ysu). There is, however, still generally more energy associated with *w* for the standard mesoscale boundary-layer parameterizations than is found using the Lilly turbulence parameterization (which is generally applied in LES applications), as comparing Figure 2.3d and f shows. A third set of spectra was computed for WRF runs using the Lilly subgrid parameterization rather than the MYNN or YSU schemes for domain 2 (Figure 2.3e and f). For a grid spacing of 0.96 km, there is very little difference in the results regardless of the boundary-layer parameterization used in domain 1. Similar to the previous case, more energy is resolved as the grid spacing shrinks and the difference between the runs using the MYNN and YSU parameterization is generally small.

A second part of the study was designed to investigate the impact of boundary conditions provided by mesoscale simulations that use grid spacings in the *terra incognita* on microscale simulations that use the mesoscale simulations as boundary conditions (Figure 2.4). A careful examination of results for the finest resolution domain in each configuration was also completed. Similar to the results for domain 2, the turbulence spectra look similar regardless of the PBL parameterization that is used for the other domains, the refinement ratio, or the resolution of either domain 1 or 2. For example, simulation Ti2 applies grid spacings of 3.84, 0.96, and 0.24 km in domains 1, 2, and 3, respectively. The spectra are nearly indistinguishable from the Ti6 case, which only uses two domains with grid spacings of 2.4 and 0.24 km. As an additional test, a simulation was completed using WRF-LES driven with time-varying boundary conditions directly from the North American Regional Reanalysis (Figure 2.4b). In this case, the turbulence spectra from the nested (Ti4-Ti7) and standalone simulation (R1) are very similar over much of the spectrum. The R1 case has smaller amounts of energy at larger scales, suggesting that the use of the mesoscale nest leads to more realistic simulations in the flow simulated with the microscale model. Our results presented here suggest that the impact of mesoscale domains with grid spacing in the *terra incognita* do not have a large impact on the microscale results.

So why do we see little impact of spurious results on the microscale simulations? We believe that part of the reason is the diffusion of the structures by the relaxation and smoothing algorithms applied at the WRF domain boundaries, and in the diffusiveness of the 3-D turbulence parameterization that is applied.

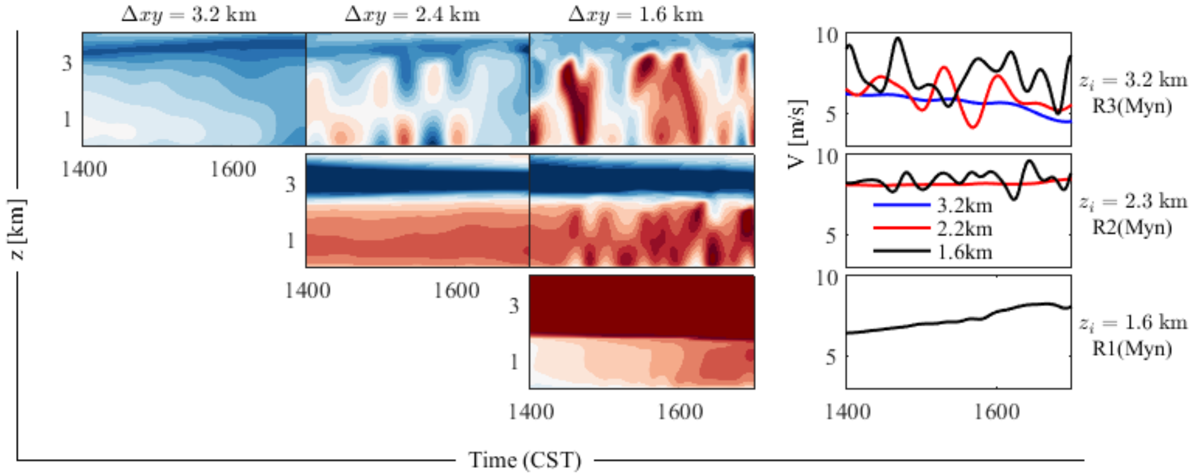

Figure 2.2. Time-height contour of wind speed constructed from a vertical profile extracted for the column closest to the Texas Tech University tower at the SWiFT site (left) and time series of wind speed (right) for horizontal grid spacings of 3.2, 2.4, and 1.6 km.

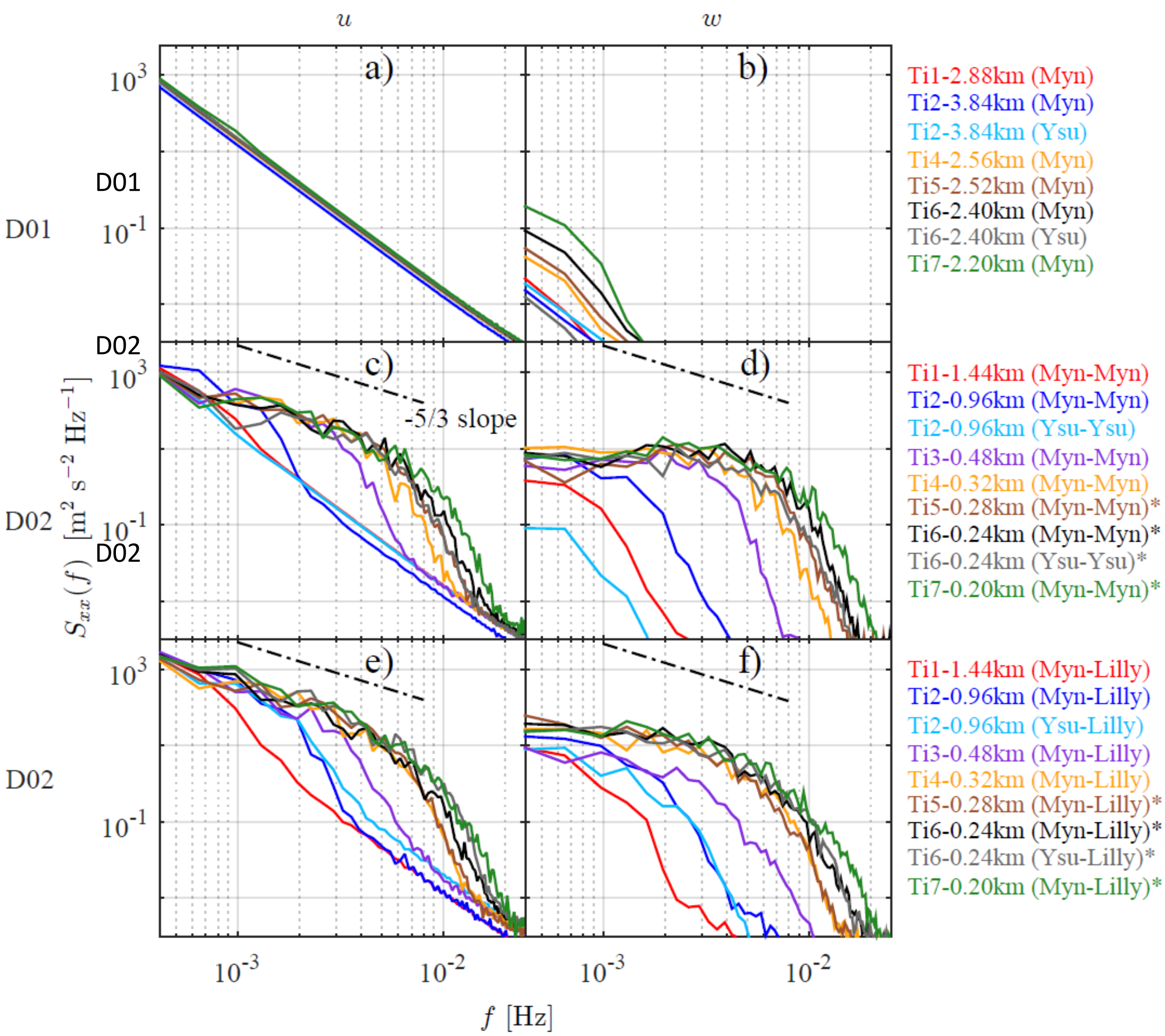

Figure 2.3. Auto-spectral density function derived for u- and w-component velocities approximately 95 m above the surface obtained from simulations with varying grid spacings, refinement ratios, and turbulence parameterizations. Simulations with an asterisk denote cases where seven times the grid spacing is smaller than z_i.

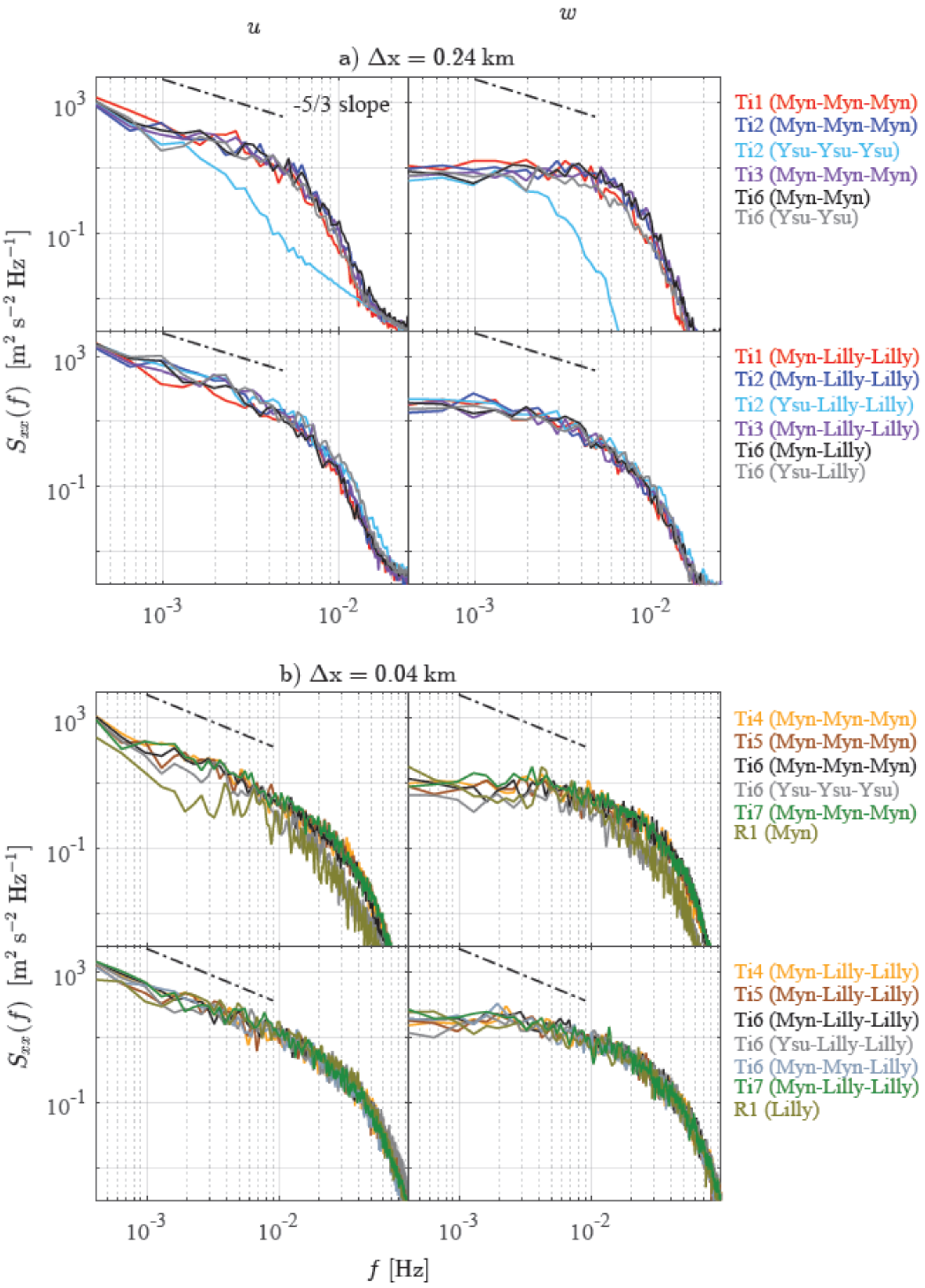

Figure 2.4. Auto-spectral density function derived for u- and w-components approximately 95 m above the surface obtained from simulations with horizontal grid spacings of 0.24 km (a-d) and 0.04 km (e-h) and different turbulence parameterizations.

2.1.3 Guidance for Configuring Coupled Mesoscale-Microscale Simulations

The results presented in this section include a number of key points that can be used to guide the configuration of the model used for mesoscale-microscale coupling:

- Users should avoid mesoscale domains that employ grid spacings smaller than z_i due to unrealistic features in the flow. If, however, the primary interest is in the results associated with the microscale domain, this advice could be ignored for the coupled WRF/WRF-LES systems. The same may not be true for other modeling systems.
- Users should feel free to select either the MYNN or YSU boundary-layer parameterization. The fine-scale turbulence properties found in the microscale domain are nearly independent of the boundary-layer parameterization used in the mesoscale domains.
- Users should avoid driving microscale simulations with large-scale reanalysis products. Fully coupled simulations that employ mesoscale nests have more energy at larger wavelengths than microscale simulations driven by a reanalysis product alone.

2.2 Mesoscale Modeling in the *Terra incognita* in Complex Terrain

Here we present work focusing on *terra incognita* issues in complex terrain. Specifically, we assessed turbulence modeling at two scales, 3 km and 750 m, the latter being in the *terra incognita*.

2.2.1 Model Setup

The focus of the simulations is the Columbia River Gorge, a densely instrumented area that is being researched under the A2e WFIP 2 project. Under the WFIP 2 project, the National Oceanic and Atmospheric Administration's High-Resolution Rapid Refresh (HRRR) model is being improved to better model wind in the PBL. To leverage efforts between the WFIP 2 and the MMC project, and to take advantage of the latest model developments, we used the HRRR and its setup for our simulations for this part of the study. This will not only allow us to study turbulence in the *terra incognita* in complex terrain for the MMC project, but also to compare our results to those of the improved HRRR model at a later time.

We assessed 12 November 2016 as a case study. This case exhibits many interesting meteorological features: (1) it is a cross-barrier synoptic case; (2) a cold front passes through the Columbia River Gorge around 1200 Coordinated Universal Time (UTC); (3) a cold pool had been persisting over the previous days, but was found to be decaying on the case day; 4) the sun breaks through the clouds later in the day, leading to showers from daytime convection around 2000–2100 UTC; (4) mountain waves are present, and topographic wakes were observed; and (5) this case was identified in the WFIP 2 event log as showing high importance for wind energy and it exhibits forecast errors. Fifteen-minute instantaneous model output was used for the analyses presented here, and we focus our investigations on Wasco, the supersite, and Arlington in both the 3-km (mesoscale) and 750-m (*terra incognita*) modeling domains.

Different grid spacings lead to different model topography, which in turn exhibits differences in model output.

Figure 2.5 shows the terrain around Wasco (black dot on the left in each panel). For Wasco itself, the grid point is close to the real altitude, for the location of Arlington, however (black dot on the right), the 750-m topography is realistic, whereas the 3-km topography deviates from reality by 100 m. This highlights the importance of choosing representative grid points in complex terrain when validating with observations, and also of interpreting results with regard to the model topography.

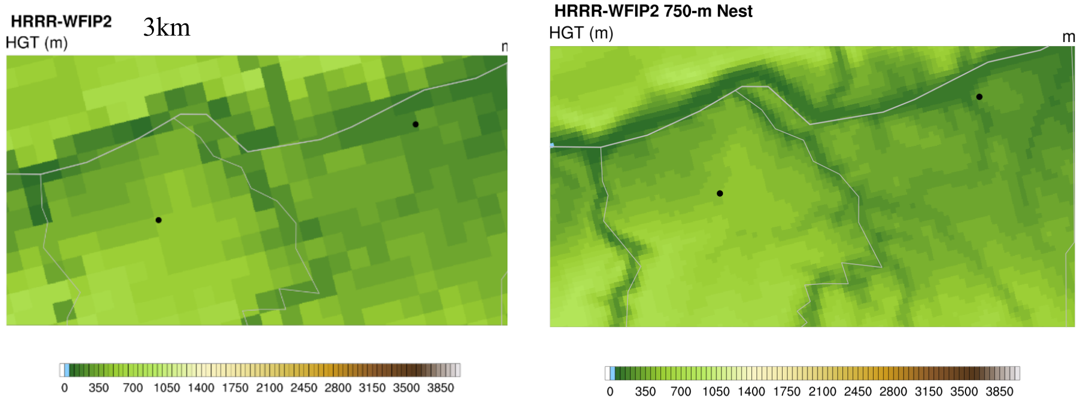

Figure 2.5. Model topography of the (left) 3-km domain and (right) the 750-m domain. In each panel, the black dot on the left represents Wasco, the right one Arlington. County borders are represented by white lines.

2.2.2 Results

First, wind speed profiles were compared to the observations (Figure 2.6). At Wasco, the timing of the onset of higher wind speeds (up-ramp) around 1500 UTC (7 a.m. local time) is well captured. However, the simulations exhibit a layer of weaker wind speed near the ground, which cannot be seen in the observations. The simulations and observations show periods of larger and smaller wind speeds during the latter part of the day, but the exact timing and magnitude of these changes are different between the observations and the 3-km and 750-m domains. Because this case exhibited wave activity and a wake from Mount Hood that was meandering, capturing these large/small wind speed patterns perfectly in time is nearly impossible for a mesoscale model. At Arlington (not shown), the onset of higher wind speed happens several hours too early in the simulations. This indicates that the skill of the HRRR model depends on the location.

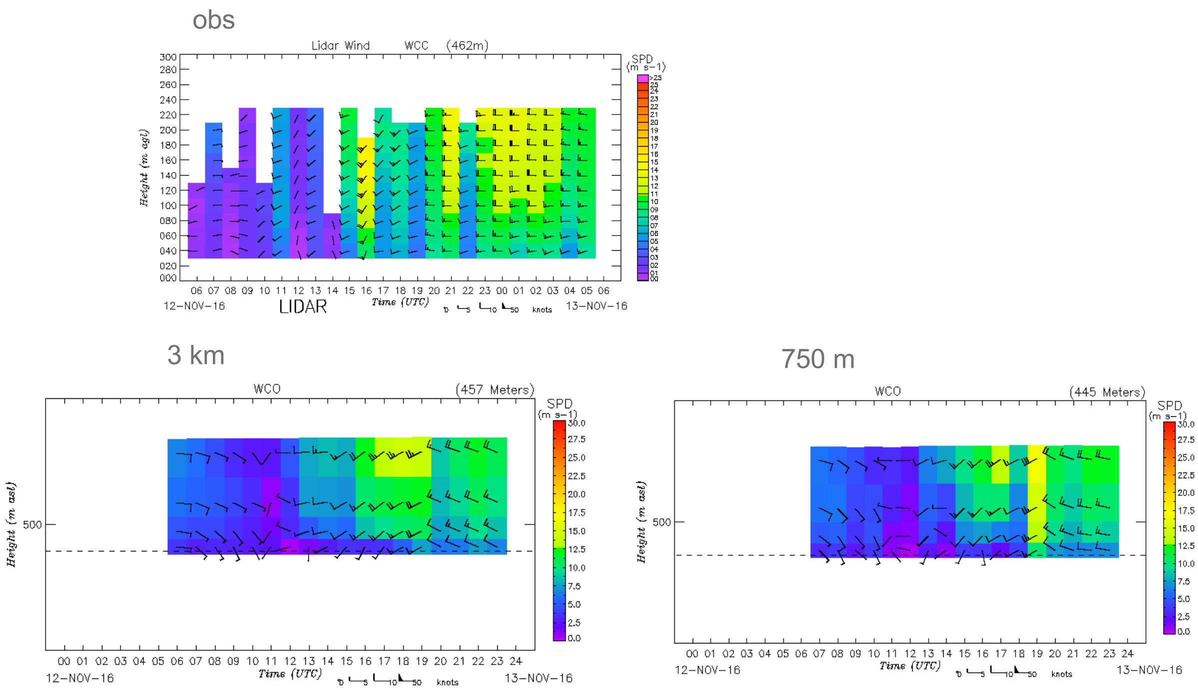

Figure 2.6. Hourly wind speed profiles at Wasco: observed (top), simulated in the 3-km domain (bottom left), and simulated in the 750-m domain (bottom right).

Figure 2.7 shows the simulated wind speed at 80 m in the 3-km domain (left) and 750-m domain (right). The finer scale structure of the flow is apparent in the 750-m domain. This also shows that at times the measurement sites can be in an area of low wind speeds and at other times in an area of high wind speeds, which supports the high/low wind speed changes seen in Figure 2.6.

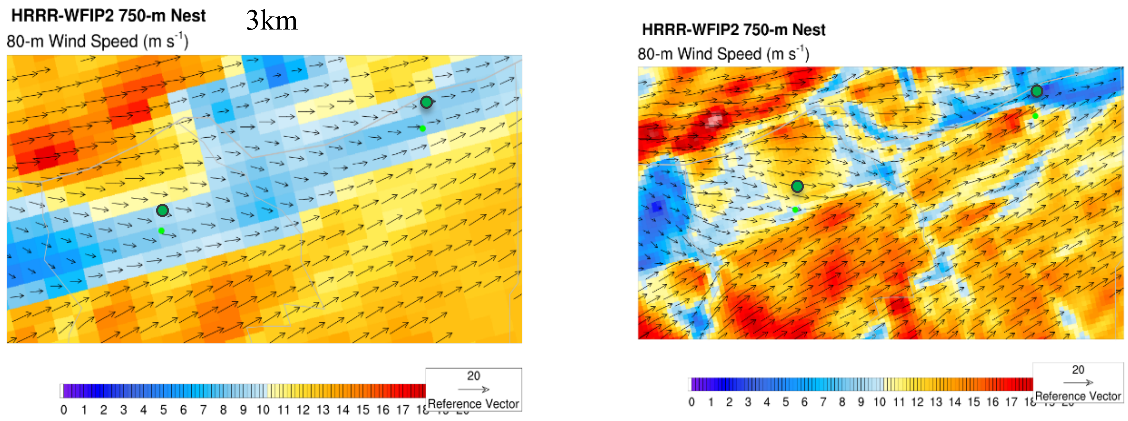

Figure 2.7. Instantaneous 80-m horizontal wind speed, over the same area as

Figure 2.5. Wasco and Arlington are represented by green dots. The 3-km domain is shown at left; the 750-m domain is shown at right.

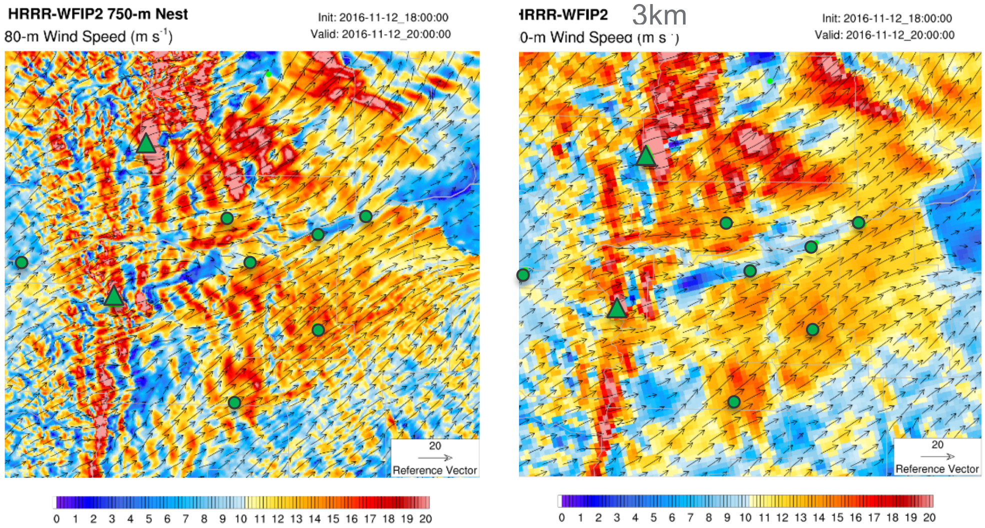

Figure 2.8. 80 m horizontal wind speed in the 750-m domain (left) and 3-km domain (right) at 2000 UTC.

Around 1800–2200 UTC, waves form and are most pronounced in the 750 m domain (Figure 2.8). They start more or less by the mountains (compare terrain over the same area as Figure 2.8 in Figure 2.9 [right]). The waves are situated parallel to the mountains and thus perpendicular to the flow and are scattered throughout the domain to the extent that one could take them for numerical noise and therefore a potential *terra incognita* issue. We believe those waves are real, but for the following reasons: (1) the wavelengths of the waves are ~10 km, which is realistic, while, on the contrary, numerical waves are assumed to be on the order of the grid spacing; (2) the waves are not parallel to the flow as observed in our FY16 study over flat terrain (Haupt et al. 2017, Chapter 4); and (3) the waves are also observed in a satellite image for the same day (Figure 2.9 [left]). Furthermore, the simulated waves can be seen in the sensible heat flux, boundary-layer height, vertical velocity, potential temperature, and cloud cover (not shown). It is worth noting that we ran the simulations with increased damping as well (zdamp increased from 5000 to 10000) without any change in simulated wave activity.

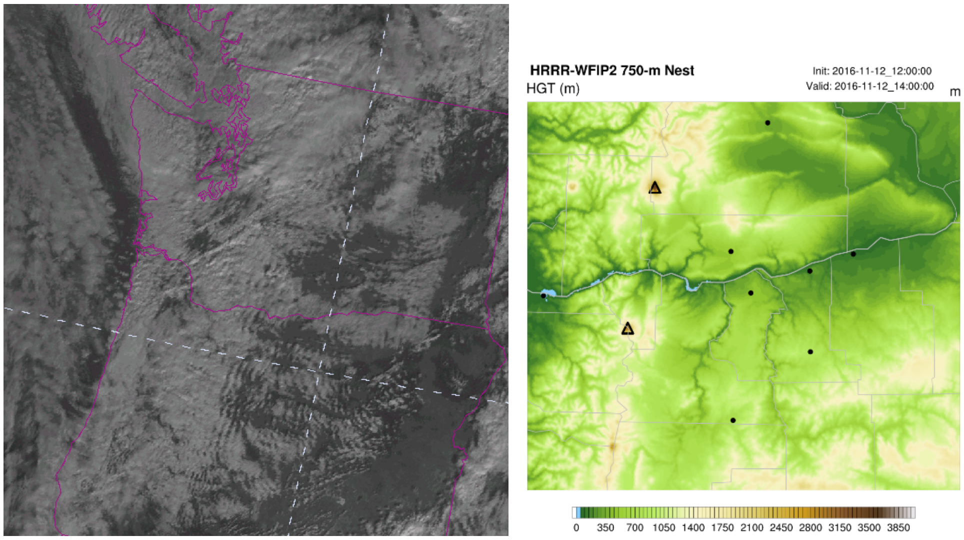

Figure 2.9. Satellite image of the Columbia River Gorge at 2100 UTC on 12 November 2016 (left); model topography over the same area as that shown in Figure 2.8 (right). Triangles denote major mountain summits and dots the measurement sites associated with the WFIP 2 project.

Next, we analyze the time series of various quantities at Wasco (Figure 2.10). The 750-m model output is more variable as expected, but not unrealistically so. The TKE increases around 1700 UTC in both simulations (Figure 2.10 c), which coincides with the PBL growth in the 3-km simulation, but not in the 750-m simulation. In the 750 m domain, the PBL begins to grow 3 h earlier, at 1400 UTC. This might explain why z_i/L (where z_i is the PBL depth and L the length scale) decreases after 1400 UTC in the 3-km simulation, but it reaches values of up to 4 until the TKE starts to increase in the 750-m simulation. The timing of this difference coincides with when the PBL is already growing in the 750-m domain, but the TKE has not yet increased. Higher values of the PBL depth lead to higher z_i/L, which indicates that L assumes values between the depth of the boundary layer and 0.25 times the boundary-layer depth in the 750-m domain between 1300–1700 UTC, but not in the 3-km domain because the depth of the boundary layer is close to zero.

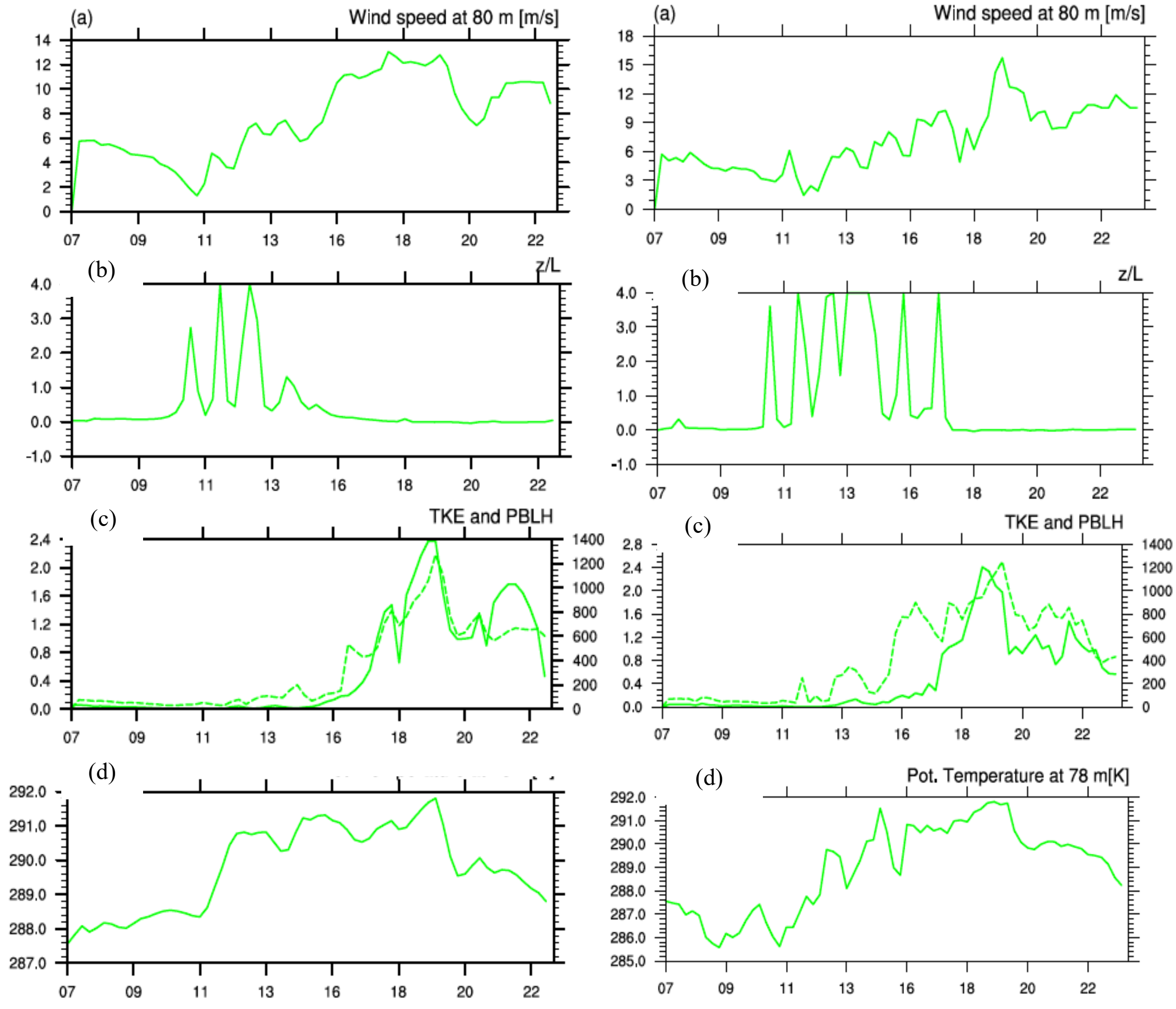

Figure 2.10. Time series for the 3-km simulations (left column) and 750-m simulation (right column) for (a) horizontal wind speed, (b) z_i / L, (c) TKE (solid) and boundary-layer depth (dashed), and (d) potential temperature.

A spectral analysis also provides valuable insight into *terra incognita* issues. Figure 2.11 displays the wind speed spectra on each domain during the 3-h window between 1800–2100 UTC, when the wave activity is at its maximum. As expected, the 750-m simulation shows higher energy than the 3-km model simulation.

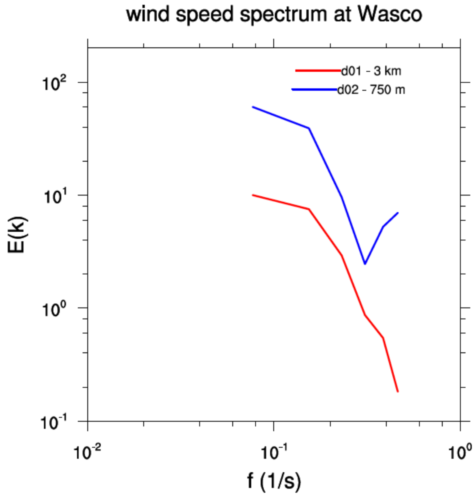

Figure 2.11. Spectra of 15-minute horizontal wind speed between 1800–2100 UTC at Wasco, as simulated on a 3-km grid (red) and on a 750-m grid (blue).

2.2.3 Outlook and Recommendations

The goal of improving simulations in the *terra incognita* is not likely to be achieved by resolving turbulence in a mesoscale model, but rather by determining whether wave-like structures are realistic features or numerical noise. Therefore, a case study in complex terrain was analyzed to determine whether simulated waves were realistic.

We found that the performance of the model depends on the site of interest and its situation within the complex terrain. The finer the grid spacing, the more realistic the terrain representation.

For this particular case, the simulated waves were perpendicular to the flow and realistic, and no *terra incognita* issues found. This is in contrast to our study last year in flat terrain, where unrealistic rolls were formed parallel to the flow. An explanation for that might be that complex terrain exhibits more horizontal variations, which could suppress the creation of unrealistic numerical features.

Follow-on work should include a comparison of these simulations in complex terrain with simulations using the improved versions of the HRRR model, which was optimized to produce realistic simulations in the *terra incognita* within the WFIP 2 domain by implementing 3-D boundary-layer parameterizations.

As has been concluded in Section 2.1.3, for coupled WRF/WRF-LES systems, the microscale solution might yield correct flow fields even if the mesoscale solution exhibits unrealistic features in the flow due to *terra incognita* issues. It will be important to know whether this is true for other modeling systems, such as standalone microscale solvers like Nalu or OpenFOAM.

2.3 Evaluation of Mesoscale Forecasts at Two Resolutions

For this formal evaluation, cases representing 12 and 21 November 2016 were chosen by MMC team. The 12 November case includes a frontal passage and cold pool in the Wasco area, followed by rolls and a wake. The 21 November case includes a wake in the lee of Mount Hood and is the same case discussed previously in Section 2.2. Here, performance of the WRF model is examined via comparisons to measurements from instruments at the Wasco WFIP 2 site (https://www.esrl.noaa.gov/psd/renewable_energy/wfip/).

WRF version 3.7+ model outputs of air temperature and wind speed/direction were verified against the observations at this site. The model used the aerosol-aware Thompson microphysics and the MYNN boundary-layer parameterization and was forced using a Global Forecast System model background. Two model grid spacings were used: 3 km to examine the impact of mesoscale accuracy on the microscale model it forces, and 750 m to compare the performance of predictions for the *terra incognita* with the mesoscale (3 km). From Figure 2.10c, we confirm that the PBL depth is always less than the mesoscale grid spacing, but during the nighttime hours it becomes less than the 750-m grid spacing of the finer nest as well.

The evaluation includes time series and profile plots of forecast and observed values for each model grid spacing, as well as summary verification statistics for each grid spacing and time period. All comparisons are based on the profiler and sonic detection and ranging (sodar) observations available at the Wasco site. For the profiler, the 417-ns measurements with 1-h time resolution are used; only temperature observations are available from the profiler. The sodar measurements of wind speed and direction have a 15-minute temporal resolution. Results for the two cases are provided in the following subsections.

2.3.1 12 November 2016

This case was characterized by a cold pool mix-out around 1500 UTC near Wasco, waves from Mount Hood between 1800–2000 UTC, and a wake at 2000 UTC.

2.3.1.1 Temperature

Time-series plots of temperature from the Wasco profiler are presented in Figure 2.12. The times marked on these plots (and for all time series for this date) represent the timing of the cold pool mix-out around 1500 UTC, the waves present from 1800–2000 UTC, and the wake at 2000 UTC. The plots in Figure 2.12 indicate that the model results are not greatly different for the two model resolutions; the patterns across both time and altitude are quite similar. However, the changeover from an inversion in the 3-km predictions is somewhat different from what occurred in the 750-m predictions. More specifically, the temperatures at lower altitudes do not change much in the 3-km predictions, but they increase a couple degrees in the 750-m predictions. The timing of the changeover from the inversion is also about 30–60 minutes later in the 750-m predictions. Moreover, the model results for both resolutions differ greatly from the profiler observations, which are characterized by distinct periods with different patterns. Most notably, the model did not capture the observed peak in temperature in the period between 0700–1100, or the large increase in temperature between 1800–2000 UTC (i.e., during the wave period). Thus, it did not adequately capture the breakup of the cold pool at either resolution.

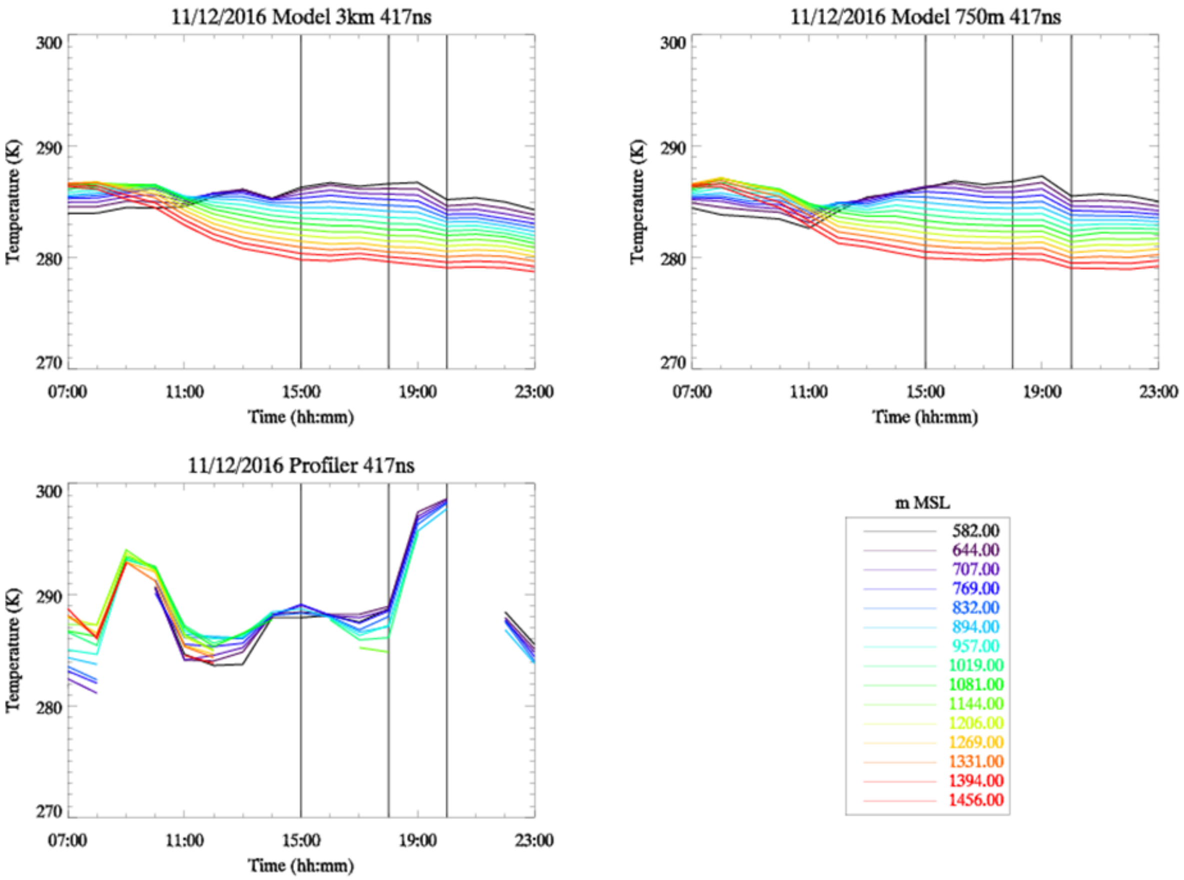

Figure 2.12. Time series of temperature forecasts at Wasco for the 12 November 2016 case with matching observations from the 417-ns profiler.

Temperature profiles for the three times of interest (i.e., the cold pool mix-out at 1500 UTC, the waves at 1900 UTC, and the wake at 2000 UTC) for the 12 November 2016 case are shown in Figure 2.13, with observations based on the 417-ns profiler measurements. These figures indicate that the model—at both grid spacings—greatly underestimated the temperatures at nearly all levels at these three times. The only exception is at lower levels at 1500 UTC when the model error is only 2–3 degrees cooler.

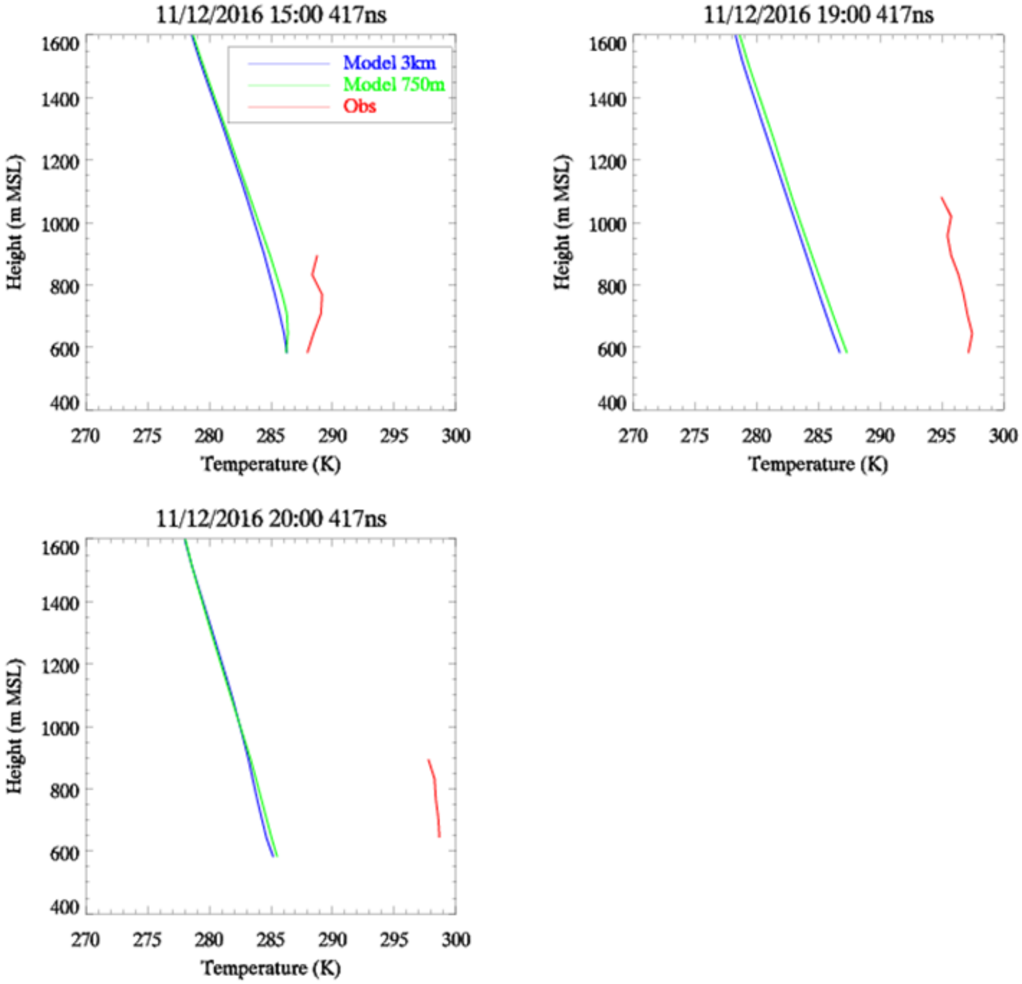
11/12/2016 15:00 417ns

11/12/2016 19:00 417ns

11/12/2016 20:00 417ns

Figure 2.13. Vertical profiles of temperature forecasts and observations at Wasco for the 12 November 2016 case with matching observations from the 417-ns profiler.

2.3.1.2 Wind Speed

Time series of model-based wind speed predictions for Wasco are shown in Figure 2.14, which includes comparisons of the model predictions to the values measured by the sodar. These plots indicate that very different time series of wind speed were predicted by the 750-m version of the model than by the coarser version. In particular, the 3-km version of the model predicted fairly consistent wind speeds across the time period at all levels, whereas the 750-m version showed increasing wind speeds at all levels in the first part of the period and a greater spread in speed with altitude, followed by a decrease through the rest of the period, at all levels. This is consistent with development of a low-level jet (LLJ) that is captured in the finer mesh, but not in the coarser version. The profiler plot indicates a weaker LLJ that breaks down later. The 750-m wind speed predictions also converge with altitude toward the end of the period as the LLJ breaks down, whereas the 3-km predictions begin to spread out slightly with altitude at later times. The observed wind speeds also increase during the first part of the period, but not as quickly or as much as in the 750-m model predictions. The observations vary somewhat in the period between 1500–2100 UTC but do not exhibit a consistent downward trend. However, this trend is difficult to quantify because of the amount of missing observational data after 1800 UTC. Overall, the 3-km model predictions are somewhat too large during the early period and on average close to the observed values during the later period. The 3-km model also does not capture the wind speed increases through time after 1300 UTC. In contrast, the 750-m model wind speeds are generally much too large during the first part of the period (i.e., before 1200 UTC), but an increase in wind speed, although several hours too early, is captured, denoting the formation of the LLJ, but not with the correct timing.

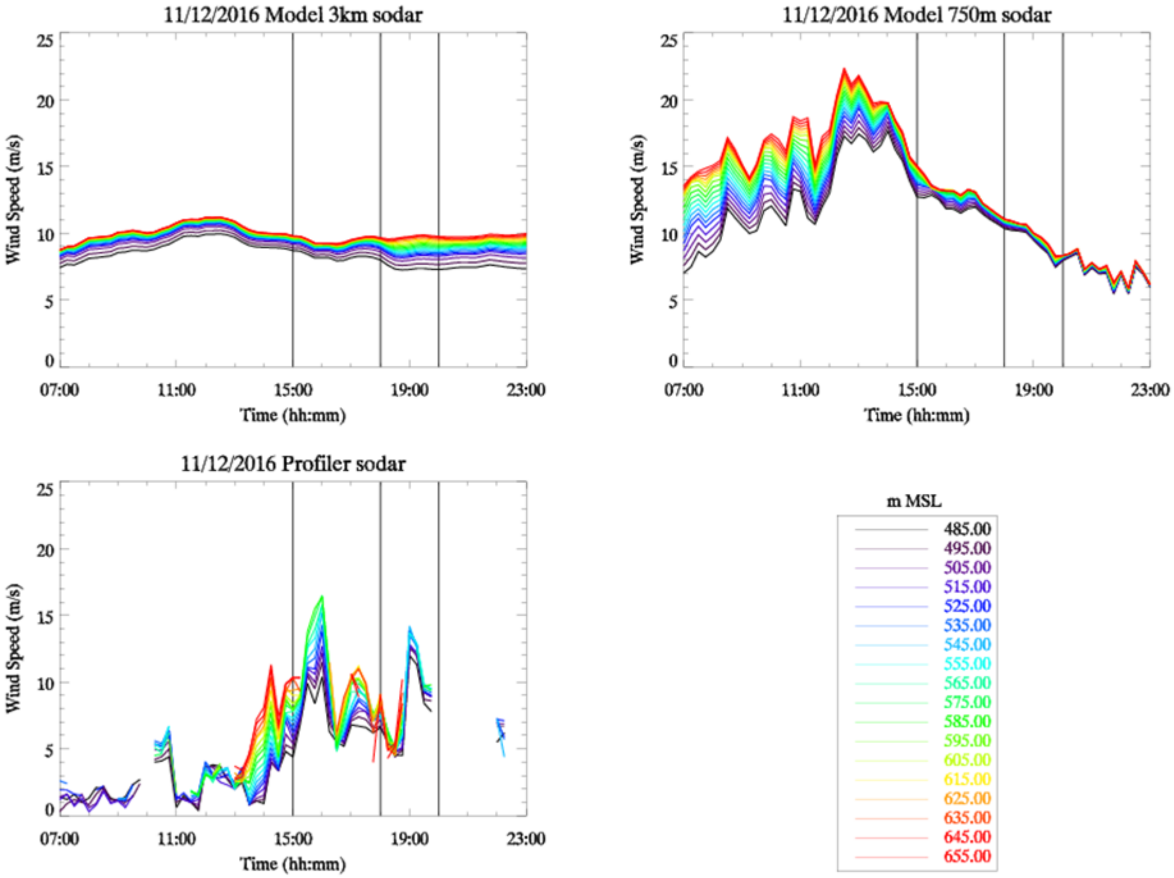

Figure 2.14. Time series of wind speed forecasts at Wasco for the 12 November 2016 case with matching observations from the sodar.

The vertical profiles in Figure 2.15 indicate that both versions of the model overestimated the wind speed at 1500 UTC at most levels, and that greater positive bias is associated with the 750 m version of the model. At 1900 UTC, the two versions of the model had similar wind speed profiles, and both underestimated the wind speed at all levels represented in the observed profile (up to about 550 m mean sea level). The 750-m predictions better captured the increase in wind speed with height at 1500 UTC, while at 1900 UTC the 750-m model forecast was almost uniform with height, indicating more uniform mixing by that time, while the observations still indicated an increase with height; this change was better captured by the 3-km model.

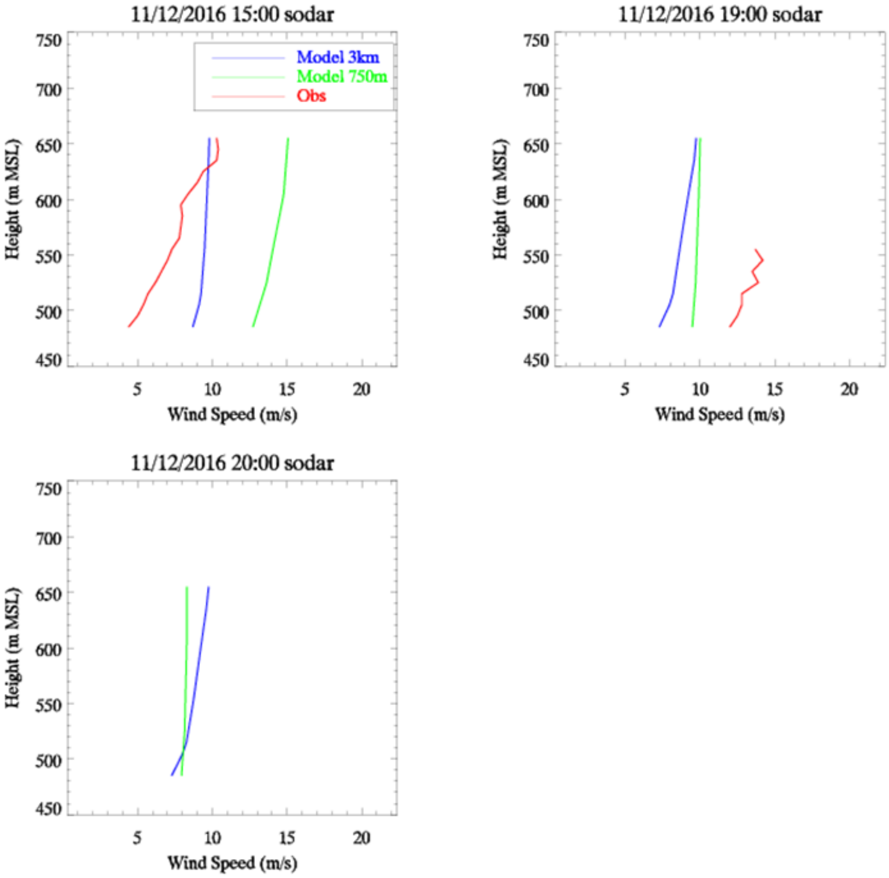

Figure 2.15. Vertical profiles of wind speed forecasts and observations at Wasco for the 12 November 2016 case with matching observations from the sodar.

2.3.1.3 Wind Direction

Figure 2.16 shows the time series of wind direction for Wasco for 12 November 2016, along with observations from the sodar. The forecast wind direction from the 3-km version of the model was consistently around 280 degrees across the time period for all heights, whereas the direction gradually shifted from about 190 degrees to about 280 degrees in the 750-m predictions, again at all heights. The observed direction was quite variable at low levels (upper-level observations were not available) during the early part of the period and became relatively consistent around 250 degrees during the middle part of the period. It is important to note that the observed wind speeds in the early part of the period were quite small, which naturally makes it difficult to obtain consistent wind direction measurements. During the period of interest, between 1500–2000 UTC, both versions of the model seem to have provided adequate estimates of wind direction. However, the distinctions between levels that are apparent in the observations are not visible in the model results, notably the backing of the winds with height.

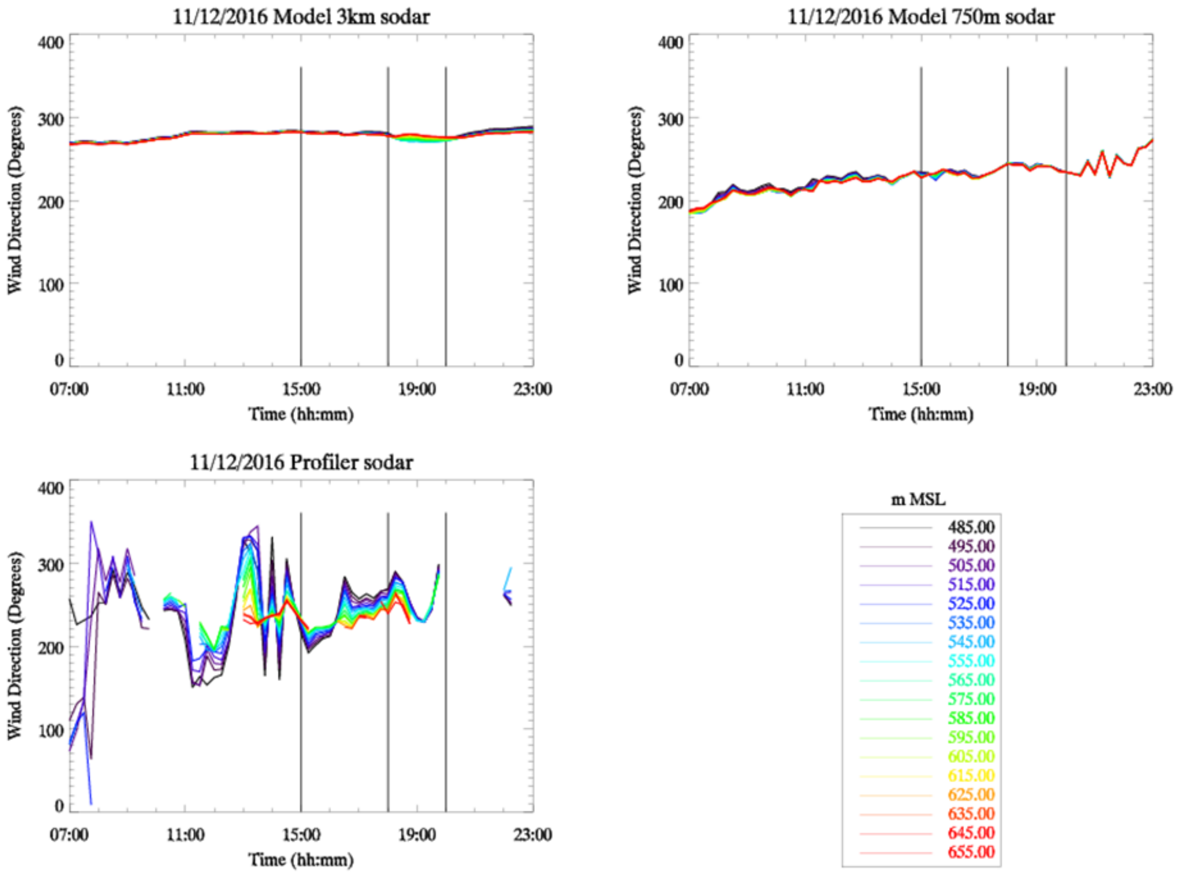

Figure 2.16. Time series of wind direction forecasts at Wasco for the 12 November 2016 case with matching observations from the sodar.

Vertical profiles of wind direction are shown and compared in Figure 2.17. The plots in this figure confirm that the 750-m predictions of wind direction were much closer to the observed values than the 3-km predictions and that the predictions from the two versions of the models were quite different from each other. In addition, the model profiles correctly indicate that the wind direction did not vary with height at these times.

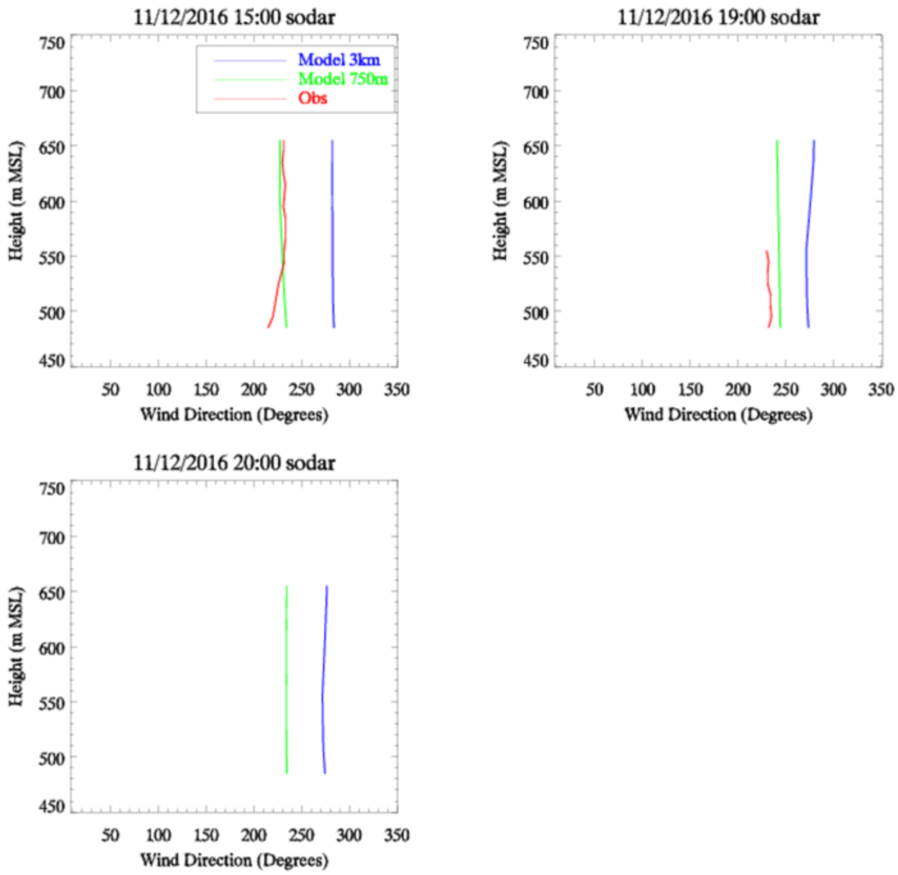

Figure 2.17. Vertical profiles of wind direction forecasts and observations at Wasco for the 12 November 2016 case with matching observations from the sodar.

2.3.1.4 Summary Statistics

Table 2.2 presents summary verification statistics for the 12 November case. The results in this table are based on an aggregation of all forecast and observation pairs across all times and levels. The mean error (ME) values indicate that both model versions are biased negatively overall for temperature and positively for wind speed. The 750-m version of the model appears to have much larger wind speed biases than the 3-km version. The mean absolute error (MAE) and root mean squared error (RMSE) values both indicate the overall errors for temperature for the mesoscale and *terra incognita* versions of the model were similar, whereas the 750-m MAE and RMSE values for wind speed are larger than those for the 3-km version of the model. Note that this result could represent a confounding of the bias (ME) values with the random errors. This suggestion is confirmed by the correlation coefficient (CC) values (because CC ignores bias), which are identical for the 3-km and 750-m wind speed predictions. The CC values for wind speed are negative, suggesting that overall, the predictions are providing “contrary” information about wind speed. The CC values for temperature are quite small but positive.

Table 2.2. Summary statistics for the 12 November 2016 case across all pairs of model predictions and observations. Temperature results are based on the profiler observations, and wind speed results are based on the sodar measurements.

Variable	Grid Spacing	Mean Error (ME)	Mean Absolute Error (MAE)	Root Mean Squared Error (RMSE)	Correlation Coefficient (CC)
Temperature	3 km	-3.08	3.58	4.93	0.17
	750 m	-3.09	3.54	4.85	0.25
Wind speed	3 km	3.19	4.22	5.07	-0.35
	750 m	7.04	7.83	9.30	-0.35

2.3.2 21 November 2016

This case was characterized by an observed wake from Mount Hood during the period from 1900–2300 UTC, which may or may not have affected the Wasco site. It is the same case discussed previously in Section 2.2.

2.3.2.1 Temperature

Time series of predicted and observed temperature values at the Wasco site on 21 November 2016 are shown in Figure 2.18. These time series indicate that the temperatures were consistent across time at all levels for this case, and the model-predicted temperatures appear to be fairly similar to the observed temperatures at most levels where observations were available. There were no major differences between the 3-km and 750-m temperature predictions.

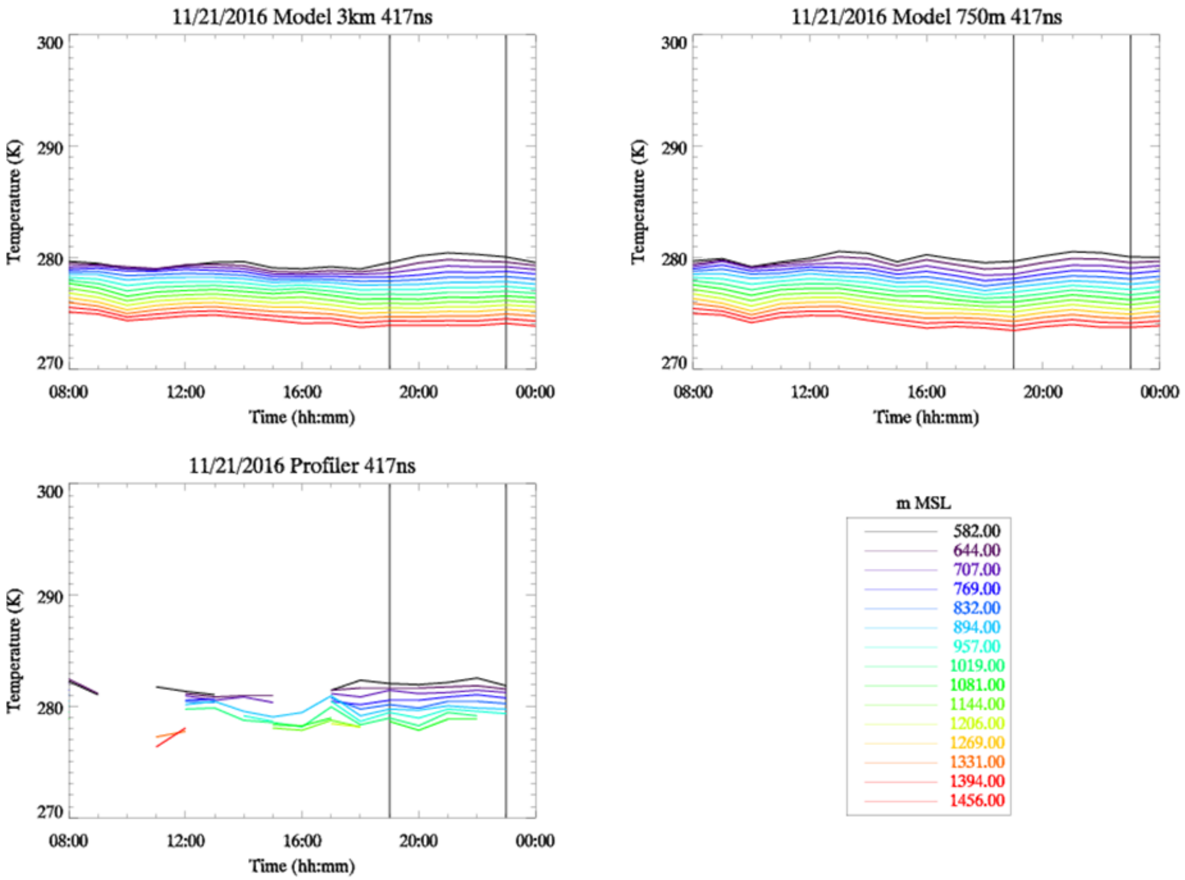

Figure 2.18. Time series of temperature forecasts at Wasco for the 21 November 2016 case with matching observations from the profiler.

However, the profiles of temperature at 1900, 2100, and 2300 UTC (the beginning, middle, and end of the wake period) shown in Figure 2.19, which provides a more detailed look at the differences between the predictions and observations at these particular times, indicate that the forecasts generally underestimated the temperatures by one or two degrees at all observed altitudes. The results from the two model versions are almost identical.

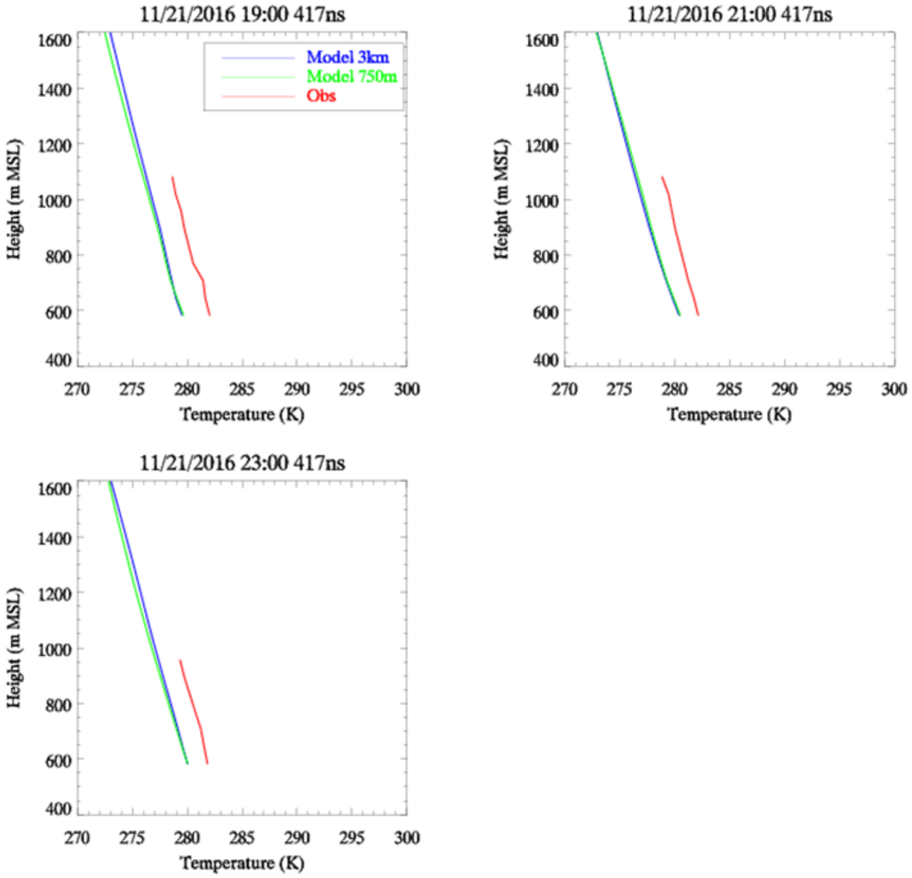

Figure 2.19. Vertical profiles of temperature forecasts and observations at Wasco for the 21 November 2016 case with matching observations from the profiler.

2.3.2.2 Wind Speed

The time series of wind speed in Figure 2.20 suggest that the 3-km version of the model is better able to capture an increase in wind speed at most levels during the period associated with the wake (between 1900–2300 UTC), although the 750-m version appears to capture the oscillations at about the correct frequency, in agreement with the results presented in Section 2.1.3. This provides further evidence that the oscillations are realistic and unlikely to just be numerical noise. However, the 750-m predictions appear to be more accurate during the early part of the period when the 3-km predictions are too large compared to the observations. Moreover, the 750-m wind speeds are closer to the observed values during the latter part of the period, even though the 750-m model did not capture the wind speed increase that characterizes the observed speeds between 1600–2100 UTC.

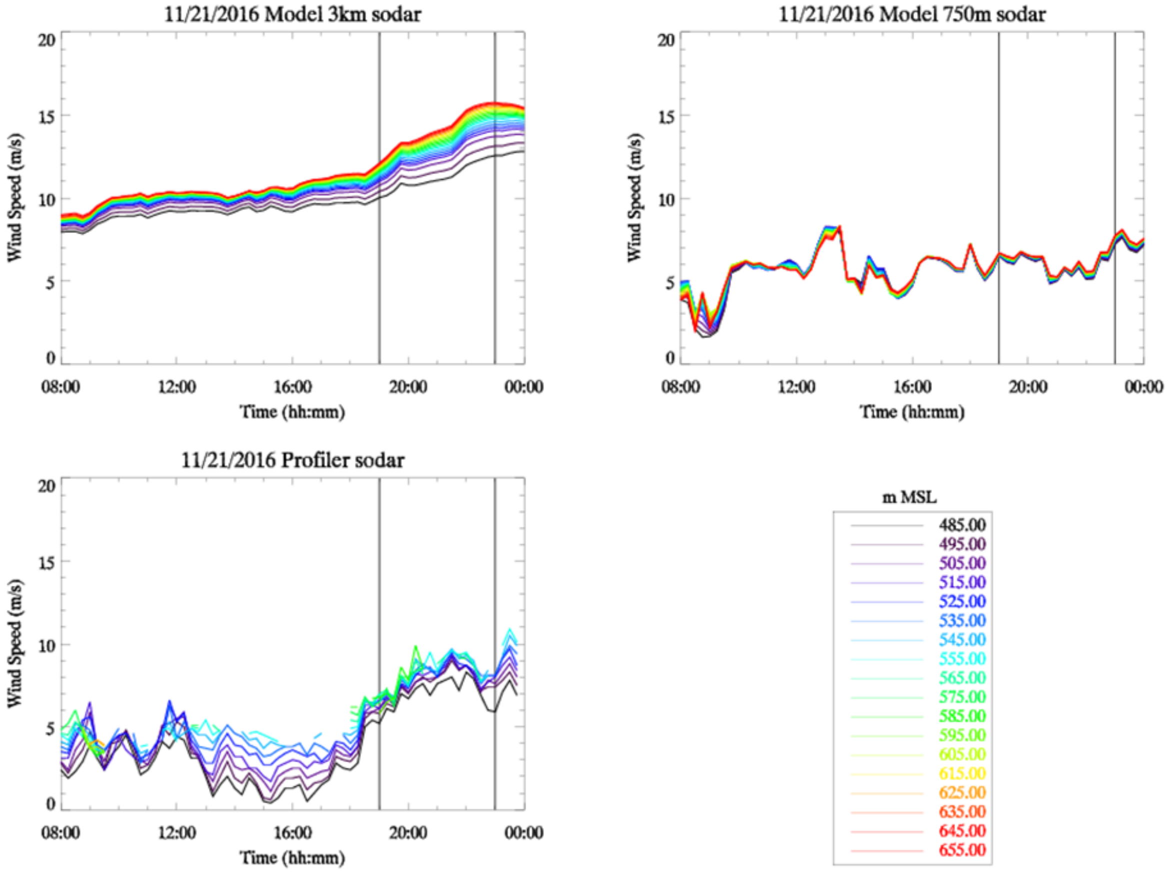

Figure 2.20. Time series of wind speed forecasts at Wasco for the 21 November 2016 case with matching observations from the sodar.

Profiles of wind speed for 21 November 2016 are shown in Figure 2.21. These diagrams confirm that the 750-m version of the model reproduced the observed profile better than the 3-km version at the beginning and end of the period of interest (i.e., 1900–2300 UTC). At 2100 UTC, the *terra incognita* predictions are smaller than those observed by about 3 m s^{-1}, while the 3-km predictions are too large by an equal amount.

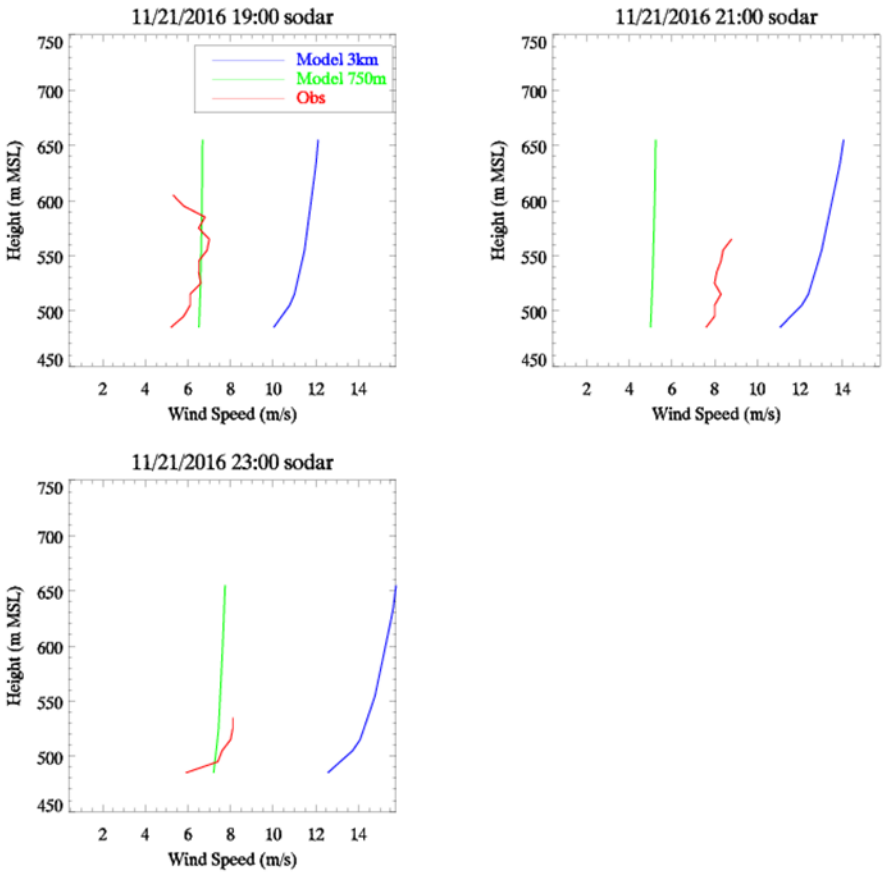

Figure 2.21. Vertical profiles of wind speed forecasts and observations at Wasco for the 21 November 2016 case with matching observations from the sodar.

2.3.2.3 Wind Direction

Time series of forecast and observed wind direction for the 21 November 2016 case are shown in Figure 2.22. This figure indicates that the two versions of the model provided quite different predictions of wind direction across the entire period, but less so during the wake period of interest (i.e., from 1900–2300 UTC). Moreover, predictions from both model versions were more similar to the observations during this period than during earlier times in the series. The 750-m predictions appear to better capture the observed variations in wind direction exhibited by the sodar observations, which is again in agreement with the analysis of Section 2.2.1, indicating that the oscillations are not spurious. The 750-m predictions also better capture the veering of the winds at the beginning of the wake period.

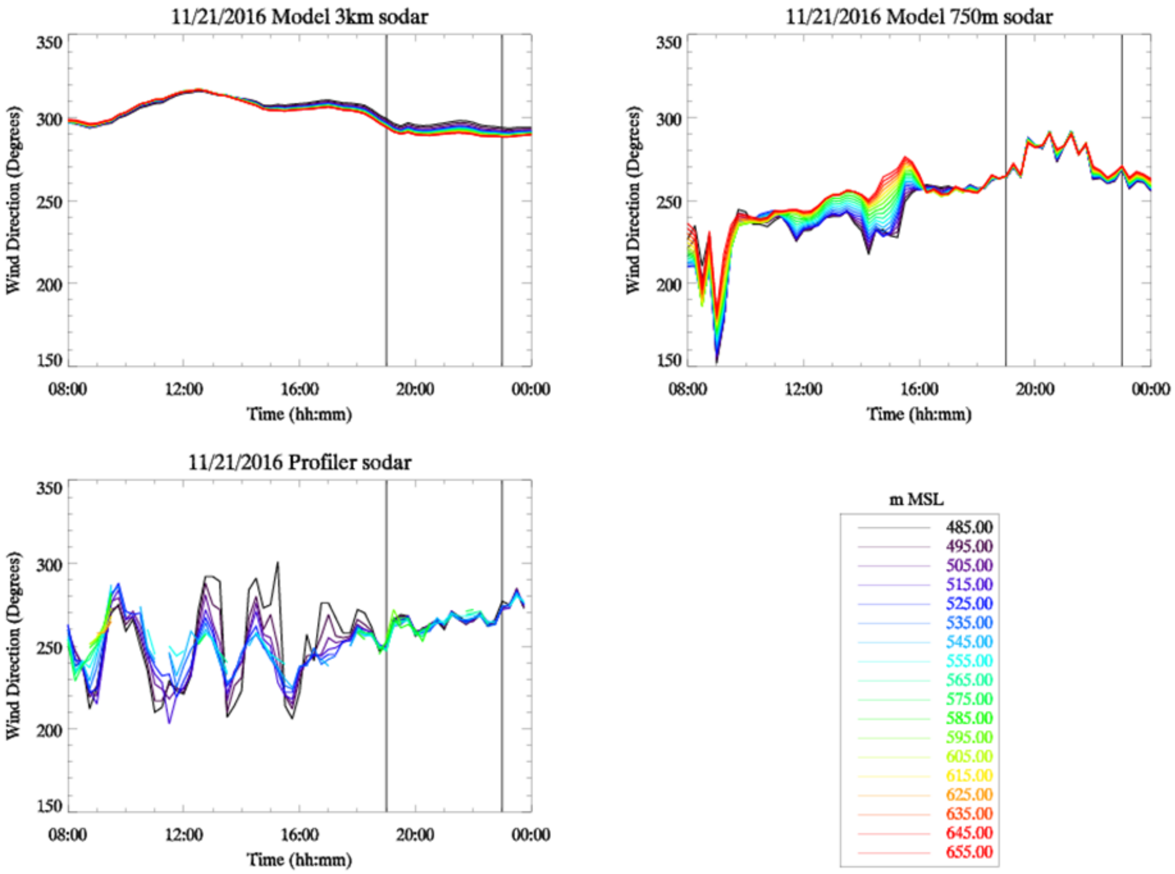

Figure 2.22. Time series of wind direction forecasts at Wasco for the 21 November 2016 case with matching observations from the sodar.

The vertical profiles of wind direction for 21 November (Figure 2.23) indicate that the 750-m predictions more closely match the observed wind directions than do the mesoscale (3-km) predictions at the three selected times. The differences between the model versions are quite small at 2100 UTC and quite large at 1900 UTC.

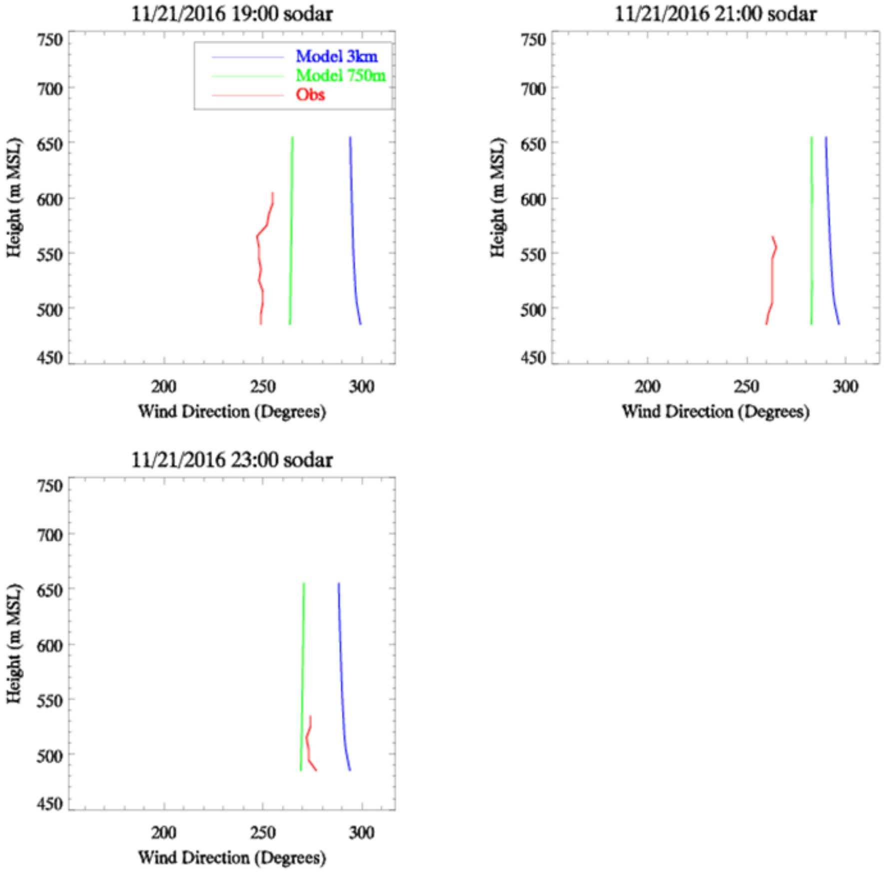
11/21/2016 19:00 sodar

11/21/2016 21:00 sodar

11/21/2016 23:00 sodar

Figure 2.23. Vertical profiles of wind direction forecasts and observations at Wasco for the 21 November 2016 case with matching observations from the sodar.

2.3.2.4 Summary Statistics

Table 2.3 shows summary verification statistics for the 21 November case aggregated across all times and levels. The ME values indicate that both model versions are biased negatively overall for temperature and positively for wind speed. This result is consistent with findings for the 12 November case. The 750-m version of the model appears to have much smaller wind speed biases than the 3-km version. MAE and RMSE both indicate similar overall errors for temperature for the mesoscale and *terra incognita* versions of the model, whereas the 750-m MAE and RMSE values for wind speed are larger than those for the 3-km version of the model. All of the CC values are quite large except for the value for the wind speed forecasts by the 750-m version of the model, indicating overall good correlation for temperature and wind speed predictions.

Table 2.3. Summary statistics for the 21 November 16 case across all pairs of model predictions and observations. Temperature results are based on the profiler observations, and wind speed results are based on the sodar measurements.

Variable	Grid Spacing	Mean Error (ME)	Mean Absolute Error (MAE)	Root Mean Squared Error (RMSE)	Correlation Coefficient (CC)
Temperature	3 km	-2.05	2.05	2.10	0.94
	750 m	-2.01	2.01	2.08	0.93
Wind speed	3 km	5.37	5.37	5.54	0.80
	750 m	0.40	1.95	2.40	0.23

2.3.3 Summary of Results

The results of these two case studies provide mixed indications regarding the impact of configuring the model to capture phenomena at *terra incognita* spatial scales. In some cases (e.g., wind direction profiles for 12 November 2016 and wind direction and speed profiles for 21 November 2016), the 750 m version of the model appeared to capture observed variations across time and altitude better than the 3-km mesoscale model version. However, these differences were not consistent.

Overall, the 3-km mesoscale model, which is typically used to force a microscale model, did not capture trends as well for many of the comparisons as the 750-m model did for the *terra incognita* scale. Although only two cases were analyzed here, and the trend was not consistent, these results give some indication of the utility of pursuing model development at this scale for microscale applications.

To truly evaluate these differences will require a larger set of cases and locations, and, most importantly, consistent observations for all of those cases. Limitations in the sample of observations clearly hindered the breadth of analyses that could be undertaken during this study. Further efforts will focus on adding more observations and corresponding predictions to the sample. With a larger sample of observed and modeled profiles it will also be possible to break the statistics into meaningful subsets related to forcing, level, time period, and other relevant factors to identify more precisely under which conditions the *terra incognita* resolutions provide meaningful results for these kinds of variables.

3.0 Large-Eddy Simulation Inflow Perturbations

This section addresses downscaling from a mesoscale flow, which does not contain resolved scales of the classical 3-D turbulence spectrum, to a LES, within which the energy-producing scales of the turbulence spectrum are explicitly resolved. Under most meteorological conditions, formation of the turbulence spectrum within the LES domain, triggered by small heterogeneities within the mesoscale flow field, is slow, incurring significant computational overhead in the form of long fetches upstream of the location of interest upon which turbulence may develop.

Several approaches to accelerating turbulence development are being examined under the MMC project, including (1) methods that perturb the inflow, either with spectral turbulence information or stochastically, and (2) precursor methods, for which turbulence information is computed from a separate offline simulation, either run for a specific case or archived in a library. Each of these different turbulence-generation methods has a different set of benefits and drawbacks that are being examined by the MMC team. Precursor simulations and synthetic approaches can, in principle, eliminate the upstream fetch entirely, because the turbulence information is imparted immediately at the inflow location(s). Drawbacks include potentially significant computational overhead, associated either with the precursor method from which turbulence information is harvested, or with the turbulence-generation method itself. Xie and Castro (2008), for example, achieved a significant reduction of overhead by computing correlations in two-dimensional planes. However, the method requires a priori knowledge of several flow parameters (e.g., PBL height, mean velocity, variances) that likewise require either high-frequency observational data or, more generally, precursor simulations.

Although application of the turbulence spectrum from either method provides turbulence immediately at the inflow plane, if the conditions from which the turbulence was generated do not exactly match extant flow conditions, some fetch will then be required for the specified turbulence field to equilibrate. This fetch can be quite large depending upon the departure of flow conditions from the specifications, because a correlated turbulence field can be quite robust. Experimentation will be required to determine at what interval the inflow turbulence conditions need to be updated within an evolving simulation.

Additionally, the precursor simulations themselves, either used to populate the library, or to obtain parameters for synthetic methods, will necessarily rely upon idealizations themselves, such as uniform, steady forcing and periodic lower boundary conditions, restricting their applicability to real-world forcing conditions. A further constraint using synthetic methods is that current techniques (e.g., Xie and Castro 2008) have been developed thus far only for neutral conditions over flat terrain. A further constraint when using the library method is how the turbulence content or other flow information would be harvested from the precursor simulation and applied to the mesoscale inflow in order to conserve energy, mass, or other considerations.

Given the nontrivial computational overhead and other restrictions inherent in each of the above methods, a simpler approach based on the superposition of small amplitude perturbations onto the resolved inflow variables has shown promise as an efficient and general method for instigating turbulence upon inflow into an LES domain. The approach is motivated by the idea that perturbations of the flow field at optimal spatiotemporal scales and magnitudes will trigger turbulence development through the nonlinearities inherent in the governing flow equations. Given that these perturbations and resulting correlations are developing within a given flow environment, defined, for example, by surface roughness and flux, PBL structure, and wind speed and direction profiles, the perturbations may more quickly lead to a turbulence state that is consistent with that environment than to adding a correlated turbulence field that is not in balance with the environment. A drawback of this approach is that some fetch is still required even for relatively simple and steady cases for which a library or synthetic method could provide an exact, and therefore instantaneous, inflow.

Although the main line of development of the perturbation methods, the stochastic cell-perturbation method (SCPM) (Muñoz-Esparza et al. 2015), has focused on the potential temperature field, the MMC team is also examining perturbations to the horizontal and vertical velocity components, as well as combined velocity and temperature perturbations. Because buoyancy-generated accelerations, which develop correlated structures, require some time to develop, the hope is that combining them with velocity perturbation will achieve a further acceleration of the stochastic perturbation method.

Herein we describe our progress to date and planned future work involving five different methods: a precursor simulation method for matching an observed wind speed profile (Section 3.2), an asynchronous precursor coupling method (Section 3.3), spectral perturbation method (Section 3.4), stochastic temperature perturbations (Section 3.5), and stochastic velocity perturbations (Section 3.6).

3.1 A Method for Coupling Mesoscale Data to Microscale Simulations in Complex Terrain Using Mesoscale-Driven Precursor-Generated Turbulence

When performing mesoscale-coupled microscale simulations in complex terrain, the MMC team has focused much effort on inflow/outflow simulations that superimpose some sort of fluctuations on the WRF-generated mesoscale inflow such that realistic turbulence forms with as little fetch as possible in the microscale domain. Good progress is being made with the use of either stochastic temperature or velocity perturbations. Such methods are useful for situations in which the microscale domain is nested within the mesoscale domain running within a single solver, as is the case for WRF. These methods continue to suffer from the fact that even with a lot of tuning, kilometers of fetch are necessary for the turbulence to come to some sort of equilibrium state. This is likely because the largest turbulent scales in the PBL are on the order of a kilometer, and they have a long-time memory of their origin at the inflow boundary.

As an attempt to circumvent the need for superimposed stochastic perturbations in flat terrain, we have developed a method in which we run periodic microscale simulations that have internal source terms derived from the mesoscale solver. For example, these sources may be the extracted driving pressure gradient and large-scale advective tendencies from WRF. Alternatively, these sources may be computed within the microscale solver such that they drive the plane-averaged solution to match that of the mesoscale solver. In that case, a simple P-controller with height-time varying gains is used to compute the source terms. This method is attractive in that the domain is periodic, and realistic turbulence naturally forms as in any other periodic atmospheric LES, but the mesoscale influence is present. The drawback of this method is that one is constrained to a periodic domain that has either flat or periodic terrain. Neither of these assumptions works well with realistic terrain.

This section describes a method for bringing together the advantages of both methods outlined above for the case of complex terrain using a standalone microscale solver. The idea is simple. The microscale simulation in complex terrain is not periodic, but rather has distinct inflow and outflow boundaries. In the most general case, boundaries can be a mix of inflow and outflow, which might very well be the case as wind direction changes with height or on upper boundaries over hills. Velocity and temperature data from the mesoscale solver are interpolated in space and time to create the “base” part of the inflow boundary conditions of the microscale simulation. Rather than add velocity or temperature perturbations from stochastic methods, a separate periodic microscale LES is run with driving mesoscale sources, like the pressure-gradient force. The idea is that the conditions simulated, although over flat terrain with periodic boundary conditions, will be similar enough to the terrain case that the turbulence developed will be similar to that which the terrain case should include. The fluctuating field from this mesoscale-informed precursor LES are extracted and superimposed on the WRF-derived inflow of the inflow/outflow terrain case. Mathematically, for velocity, this equates to

$$U_{inflowMicro} = U_{inflowMeso} + \left(U_{precursor} - \langle U_{precursor} \rangle\right),$$

where $U_{inflowMicro}$ is the field being used as inflow boundary conditions for the microscale simulation, $U_{inflowMeso}$ is the "base" mean inflow profile from the mesoscale solver, $U_{precursor}$ is the precursor LES-generated boundary data, and the angle brackets are the mean of the precursor flow.

The quantity in parentheses on the right-hand side of the equation is the fluctuating precursor field. Basically, we are replacing the stochastic perturbations with LES-generated perturbations in hope that less fetch is needed to create turbulence that has lost memory of the inflow boundary conditions. This method comes with the cost of being performed offline from the mesoscale simulation and of requiring a precursor LES, but the precursor fluctuating field can be saved for reuse. This method is, in many ways, similar to the library approach.

To test the idea, we selected terrain just north of the WFIP 2 Physics Site that includes the Columbia River and is shown in Figure 3.1. This case is pertinent to the wind-energy application because in reality, the Biglow Canyon Wind Farm lies just south of the site and wind turbines are situated on the ridge north of the Columbia River. The computational domain is 15 km × 15 km in the horizontal and 4 km in the vertical directions. The vertical resolution is uniform for 20 m in the lowest 1 km of the domain. Above that, the mesh coarsens to 40-m, and then 80-m resolution. The mesh is generated as a Cartesian block, and then a solid-body deformation solver is used to deform the mesh to the terrain in a way that provides terrain-normal mesh lines that are very orthogonal to the terrain.

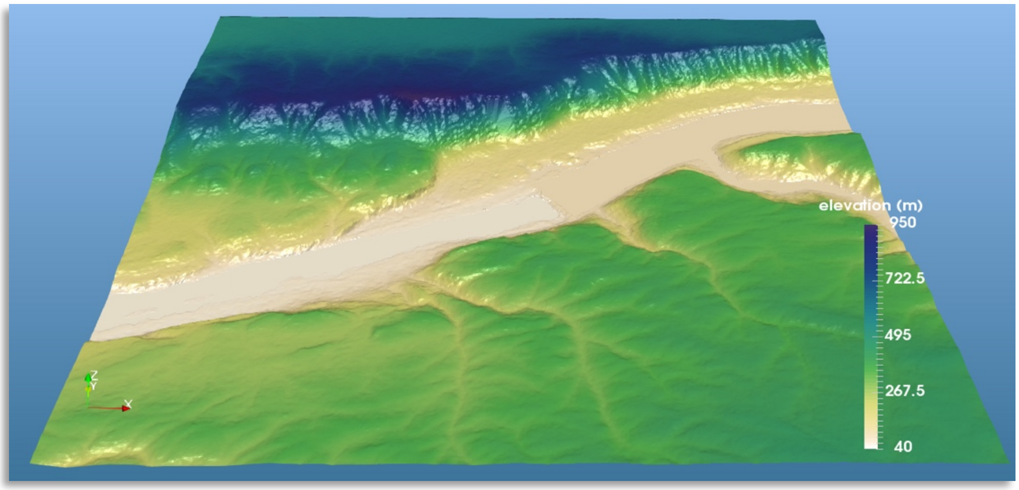

Figure 3.1. Terrain used for testing the mesoscale-microscale coupling strategy. The terrain includes the Columbia River (region shown in light color) and is just north of the WFIP 2 Physics Site.

We used mock mesoscale data rather than real mesoscale data to avoid complexity as we incrementally tested this approach. This mock mesoscale inflow is from the northwest so that it comes over the ridge to the north of the Columbia River. At 80 m above the surface, this inflow is always at 8 m s^{-1} speed 80 m above the surface, but the direction changes in time shifting from 315 degrees to 300 degrees and back. The time-height history of the mock mesoscale inflow is shown in Figure 3.2.

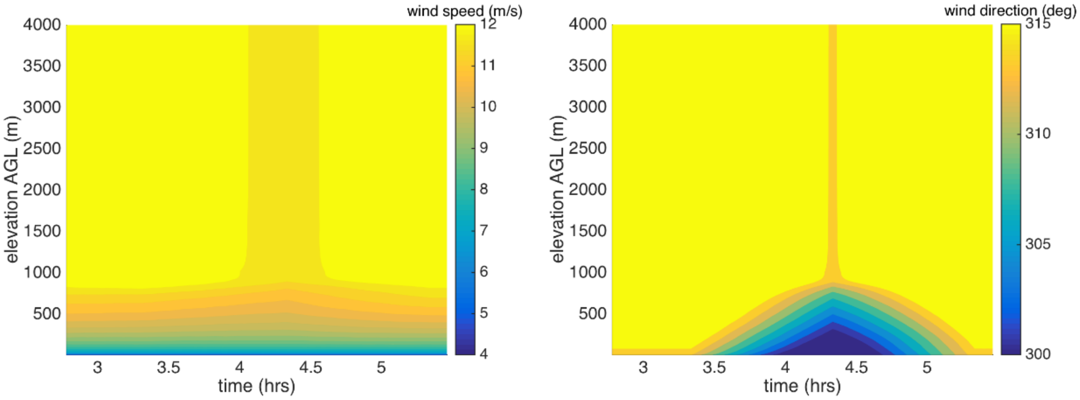

Figure 3.2. Time-height plot of "mock" mesoscale inflow used in this study.

The mesoscale-informed precursor uses a pressure-gradient force that creates the same wind direction and speed time history as the mock mesoscale data. That precursor domain is 15 km × 15 km × 4 km with the same resolution as the terrain case, although it need not have the same resolution. Velocity and temperature data on the north and west sides of the precursor domain are sampled at each time step starting and ending at times corresponding to the terrain case simulation. For simplicity, we set the surface heat flux to zero with an idealized capping inversion starting at 750 m above the surface. In the future, this information will come from the mesoscale simulation.

Because the mesoscale-influenced precursor has a flat bottom boundary, the turbulence data extracted from it are simply mapped geometrically to the terrain-conforming inflow boundaries of the terrain case. Here, a very simple mapping procedure was used because the precursor and terrain case had the same number and layout of inflow boundary cell faces. A simple one-to-one mapping from the precursor inflow plane to the terrain case inflow plane in grid coordinates was used, and the result for a single instance of the inflow velocity field on the west boundary is shown in Figure 3.3.

In this test case, the initial solution was created by performing a simple one-to-one mapping in grid coordinates, not physical coordinates, of the precursor full-field solution, similar to the boundary mapping. In cases using real mesoscale data, the microscale terrain case could be initialized to the smooth solution, which would not contain turbulence, but the turbulence would advect in from the boundaries.

At this point, our results are qualitative but promising. Figure 3.4 shows contours of instantaneous wind speed in a surface 80 m above the terrain, a height typical of wind turbine rotor hubs. One can see that the turbulence that enters the domain from the north and west is already realistic LES turbulence, so there is no need to transition from stochastic to physical turbulence. That does not mean, though, that the turbulence does not need to adjust to the terrain and the specific mesoscale conditions it then encounters. Flow separates over some of the steeper parts of the ridge to the north of the Columbia River and the wind speed becomes very low over the river. By the time the flow has crossed the river, it is horizontally non-homogeneous and clearly influenced by the terrain. Another view of the flow is shown in Figure 3.5, which also shows a contour of instantaneous wind speed, but in a vertical plane aligned with the mean wind direction and cutting through a particularly steep ridge to the north of the Columbia River. Flow separation is clearly visible past this ridge. That separation influences the flow a significant distance past the river.

In FY18, we are continuing this work by centering our domain of interest on the 80 m meteorological mast of the WFIP 2 Physics Site. We are also in the process of extracting WRF data from the November 21 topological wake case to use to drive the microscale simulation. We will place virtual meteorological masts at locations within the domain corresponding to the actual WFIP 2 Physics Site masts and sensors so that we can compare the simulated to field data.

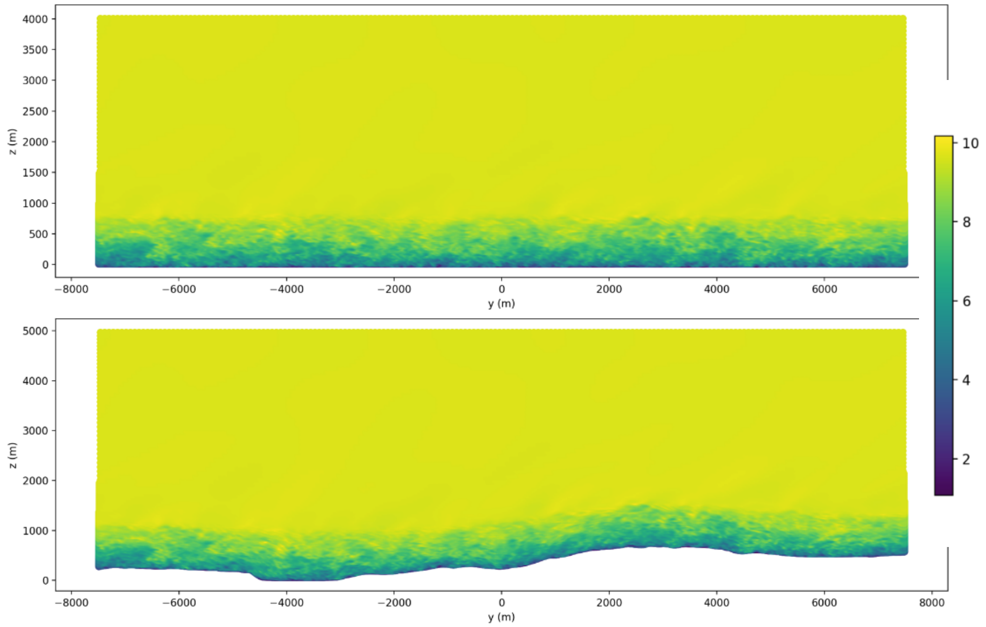

Figure 3.3. Mapping of the inflow turbulent velocity field as generated by the precursor LES (top) to the west inflow plane of the terrain case (bottom). The contours are in meters per second.

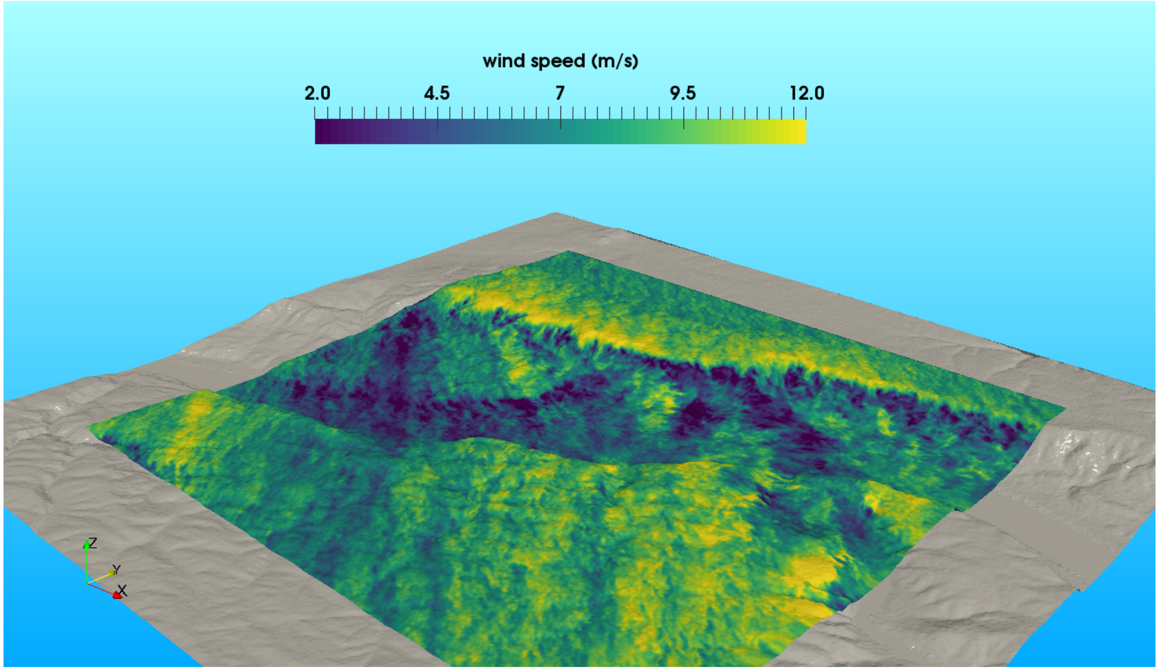

Figure 3.4. Contours of instantaneous wind speed in a surface 80 m above the terrain from the terrain microscale case. In this view, the reader is looking upwind toward the inflow boundaries.

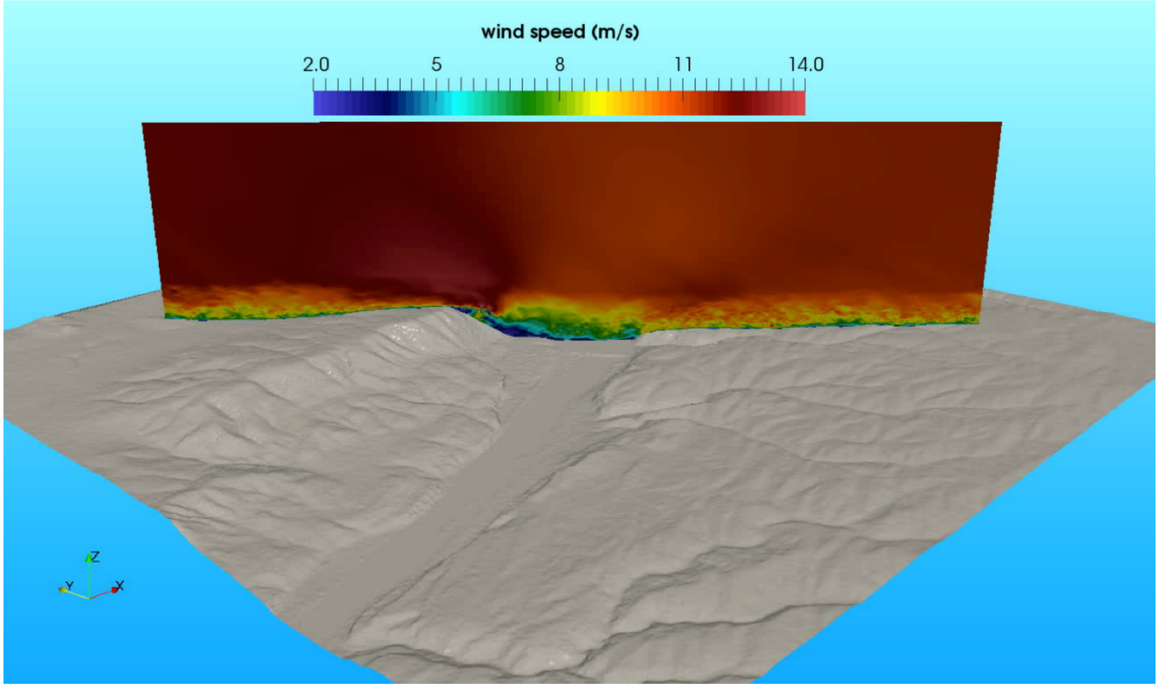

Figure 3.5. Contours of instantaneous wind speed in a vertical plane parallel to the mean wind direction from the terrain microscale case. Flow is from the left to the right.

3.2 Asynchronous Coupling

Setting time-varying turbulent inflow boundary conditions and initial conditions for a microscale simulation that is designed to produce an internal boundary layer is one of the aspects investigated by the MMC team in FY17. Improper inflow turbulent conditions could lead to transient conditions near the inlet (or inflow) boundary that persist several boundary-layer depths into the model domain (Lund et al. 1998). The minimum information about inflow conditions required for initializing the LES simulation of wind fields over a region includes the mean velocity profile, TKE profile, and a measure of the TKE (Thomas and Williams 1999). The team is working on moving well beyond this, as discussed in the rest of this chapter. The most often adopted method for overcoming this problem is to use an outer mesh that nests to the finer desired mesh. Operating an outer domain could be expensive, add computational burden, and lead to slower turnaround of the computational job. Further, the exact requirements for such an outer domain in terms of size and distance from the inner domain are arbitrary and developed using trial-and-error processes.

To avoid this outer domain, two separate processes are sometimes used. The first one is based on the use of an auxiliary (precursor) simulation discussed above and the second uses a random perturbation applied to the boundary (Lim et al. 2009) and discussed later in this chapter. The idea of using an auxiliary simulation was first proposed by Spalart (1988) and later implemented by Lund et al. (1998) for a spatially developing boundary-layer simulation. In the auxiliary simulation method, the spatial growth in the inflow conditions is accounted for by adding a source term, and by adding growth terms to the Navier-Stokes equation after performing a coordinate transformation to align the mean flow in the direction with the lowest inhomogeneity in flow, thus making it feasible to apply periodic boundary conditions to this auxiliary simulation. A method that avoids the coordinate transformation and simplification in the growth terms to make it a useful implementation for LESs was proposed (Lund et al. 1998). Another modification of the auxiliary simulation is known as the precursor simulation (Thomas and Williams

1999). Building a library of LES simulations for conditions similar to that encountered during the simulation of a selected problem was proposed by Thomas and Williams (1999). A modification of this method for a realistic PBL simulation using WRF-LES (Figure 3.6) was tested by Gaudet et al. (2012). A modification of this precursor simulation method where the precursor model and the wind farm model are run concurrently and share data was adopted by Stevens et al. (2014) and Bokharaie et al. (2016). In this case, (Figure 3.7) a portion at the boundary of the precursor simulation outflow serves as the inflow for the wind farm model with turbines. The advantages and disadvantages of these approaches is discussed in Section 3.1.

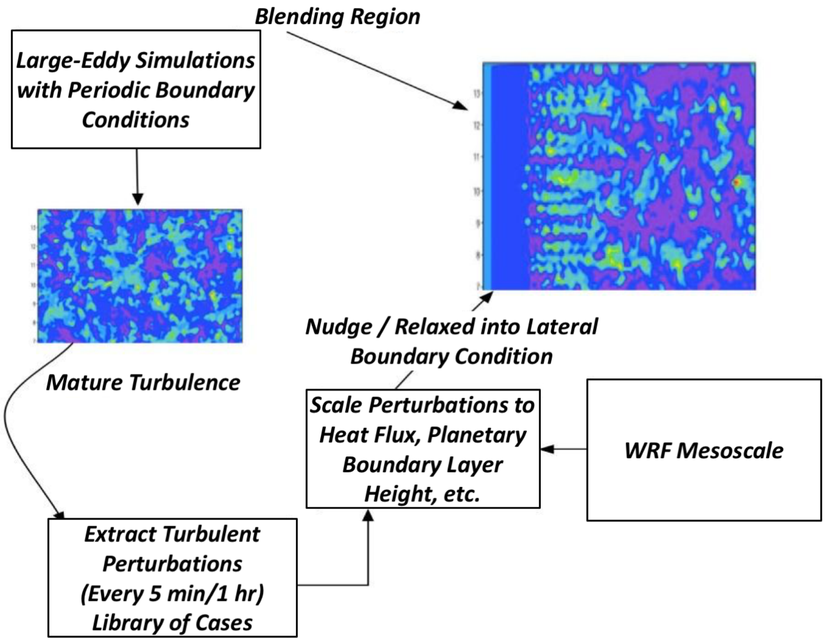

Gaudet et al., 2012

Figure 3.6. A proposed turbulent blending scheme for inflow in a coupled WRF-LES simulation with time-varying boundary conditions (based on Gaudet [2012]). This precursor method is based on building a library of pre-calculated precursor simulations.

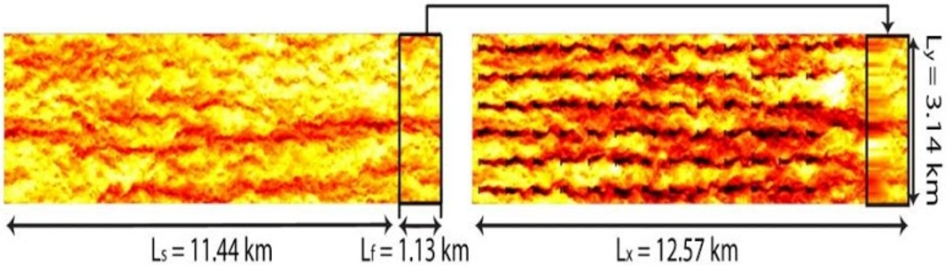

Figure 3.7. Instantaneous zonal velocities at hub height. Data from each time step are copied from the precursor simulation (left) to the inflow of the wind farm simulation before the turbines (Stevens et al. 2014).

Here we propose to build a library of precursor simulations and use the library to couple the WRF (mesoscale) to WRF-LES (microscale) with the mean flow characteristics of the flow conditions obtained from the WRF simulations matched with appropriate data extracted from the library of simulations (Figure 3.8). The challenge is to generate a library of simulations that could be useful for most expected cases of meteorological conditions that would influence the PBL development at the microscale. An initial test of the approach mostly focused on regions away from the coast and in flat terrain.

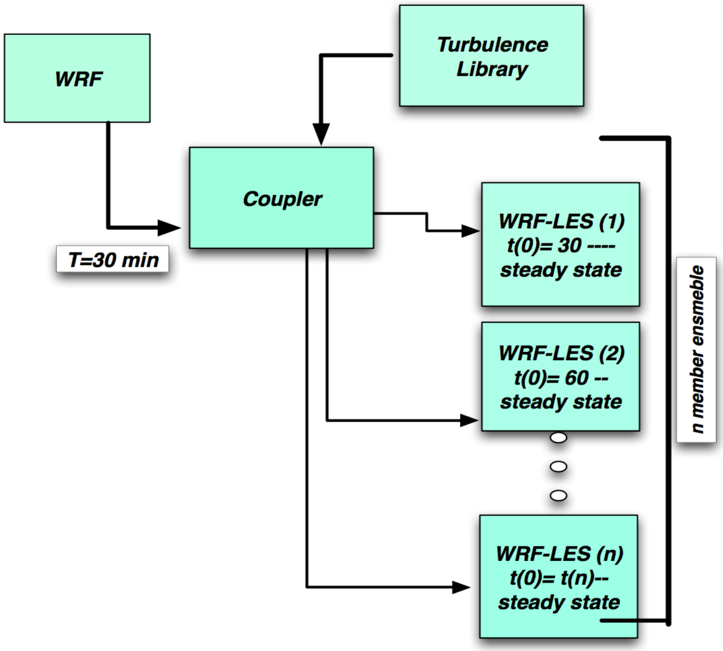

Figure 3.8. Representation of the workflow for the proposed asynchronous coupling of WRF and WRF-LES using the library.

A second coupling strategy was also tested. This method used the perturbation recycling of Mayor et al. (2002). In this mode, we recycled the outflow of the WRF-LES model to the inflow, as depicted in Figure 3.9.

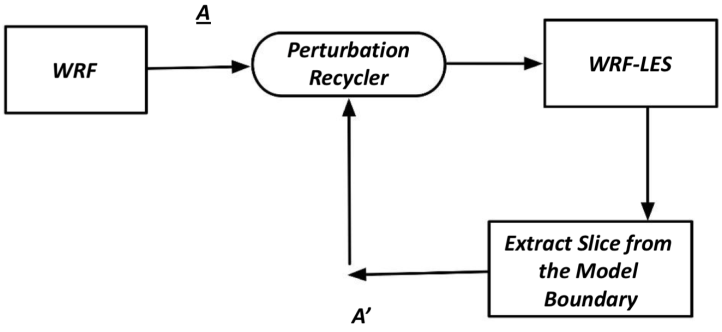

Figure 3.9. Perturbation recycling method for coupling WRF to WRF-LES. The recycler combines mean fields from WRF (A) with instantaneous/turbulence fields (A') from the WRF-LES simulations.

3.2.1 Approach and WRF-LES Simulation Configuration

To test the approach, we first build a set of simulations for a neutral case that was evaluated by the MMC team the previous year using data from the SWiFT site. The model setup and results from these simulations using WRF-LES are described next. The WRF model is configured in LES mode to perform idealized simulations. The high-resolution simulations use a horizontal resolution of $\Delta x = \Delta y = 25$ m. The vertical domain has 176 layers with vertical resolutions ranging from $\Delta z = 7.5$ to ~ 25 m. A relatively coarse $\Delta x = \Delta y = 100$ m grid resolution and 100 vertical layers are used for the low-resolution simulations. A domain size of 2.5 × 2.5 × 2 km is specified in the x, y, and z dimensions. Revised MM5 Monin-Obukhov surface-layer and thermal diffusion schemes are enabled. The model is initialized with doubly periodic boundary conditions to allow the turbulence field to develop within the short simulation domain. Random perturbations are added on the mean temperature field at the lowest four vertical levels to aid with turbulence spin up. The 1.5 order TKE scheme is used to compute the subgrid-scale (SGS) turbulent motions. The model is integrated for 16 h, with a time step of 0.5 s. Additional 1-h integrations are performed to output data at 5-minute intervals to set a basis for turbulent library development.

Figure 3.10 shows the neutral vertically uniform sounding used to initialize the simulations. The sounding was obtained for the SWiFT site in Lubbock, Texas, at 0000–0100 UTC (7:00–8:00 p.m. Central Daylight Time) on 17 August 2012. The sounding had a base potential temperature profile of 300 K and an inversion layer at 1 km. As a preliminary exercise, we chose flat-terrain and basic physics dry-flow conditions to eliminate complex flow interactions and additional lateral boundary issues.

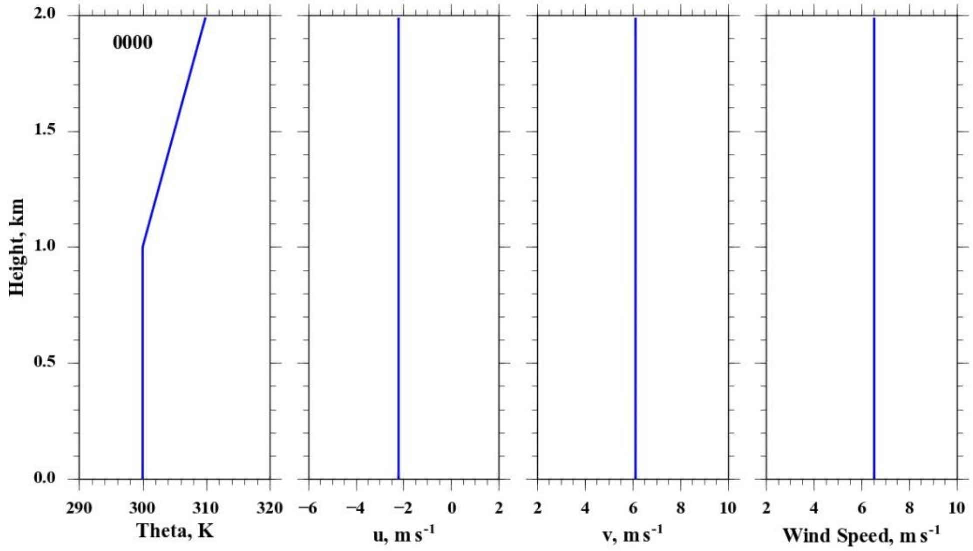

Figure 3.10. Vertical profiles of potential temperature and wind speed from an ideal dry neutral boundary layer at model initialization. The sounding data were collected at the SWiFT site at 0000–0100 UTC (7:00–8:00 p.m. Central Daylight Time) on 17 August 2012.

3.2.2 Results

3.2.2.1 Turbulence Library Development

A large number of potential use cases (or WRF-LES model run possibilities) are necessary for the library to be useful. We performed 108 simulations for each high- and low-resolution setup. Three variations in the entire layer of potential temperature (295, 300, 305 K), wind speed (low: 4.1, mid: 6.5, high: 9.1 m s^{-1}, which is constructed by 2-m s^{-1} decrements/increments of *u* and *v* winds, respectively), and surface roughness (0.1, 0.2, 0.5, 1.0 m) were simulated. The entire permutations of this set resulted in 3×3×3×4 = 27×4 = 108 unique simulations. The high-resolution setup produced ~ 33 GB × 4 = 132 GB of data, while the low-resolution setup produced ~ 1.7 GB × 4 = 7 GB. Approximately 2× lossless data compression can be achieved with an initial level compression option using the "nccopy" utility. The high-resolution setup requires ~ 8500 × 4 = 34000 compute hours (with an additional 550 × 4 = 2200 hours for 1-h restart runs). The low-resolution setup requires ~ 200 × 4 = 800 h, which is more than 40 times more computationally efficient than the high-resolution setup. Adding the complexity of physical processes (e.g., moisture and radiation) and varying additional input parameters (e.g., surface fluxes) can necessitate up to 10 times or more computational resources.

Select cases from the simulated suite are described to highlight variations in flow behavior under different atmospheric conditions and resolutions. Figure 3.11 shows the differences between vertical velocity structures at 500 m between the high- and low-resolution setups at hour 16. In both setups, updraft patterns align with the main background flow, which varies from southeasterly to southerly. With increasing wind speeds, stronger updraft/downdraft regions are produced. Although there are qualitative similarities between the results, the high-resolution simulations can resolve flow elements in much finer detail.

Vertically averaged profiles of TKE are shown in Figure 3.12 for the same set described in the previous figure. These profiles show more distinct differences between the fine- and coarse-resolution setups compared to the vertical velocity profiles. The magnitude of TKE increases with increasing temperatures and wind speeds due to enhanced buoyant/shear production of turbulence. Low-resolution simulations show large averaged turbulence values because of energy accumulation at coarse grids. Turbulent energy can dissipate more efficiently at high resolutions.

We compared the flow evolution over relatively smooth (low Z_0 = 0.1 m) and rough surface (high Z_0 = 1.0 m) conditions for high-/low-resolution simulations (Figure 3.13). High surface roughness simulations show slower wind speeds at the surface due to increased friction. In addition, flow features are more organized and more tractable within 5-minute intervals when Z_0 = 1.0 m. The same trends are apparent for the low-resolution simulations.

Despite the large variations in turbulence structures, an ideal dry simulation setup yields similar horizontally averaged wind profiles (Figure 3.14). The profiles are in better agreement under low wind conditions compared to the higher wind simulations. Discrepancies near the surface may be due to differences in the number of vertical layers. Because there are no heat fluxes entering into the domain, potential temperature profiles do not deviate throughout the simulations, and show identical results in high-/low-resolution setups.

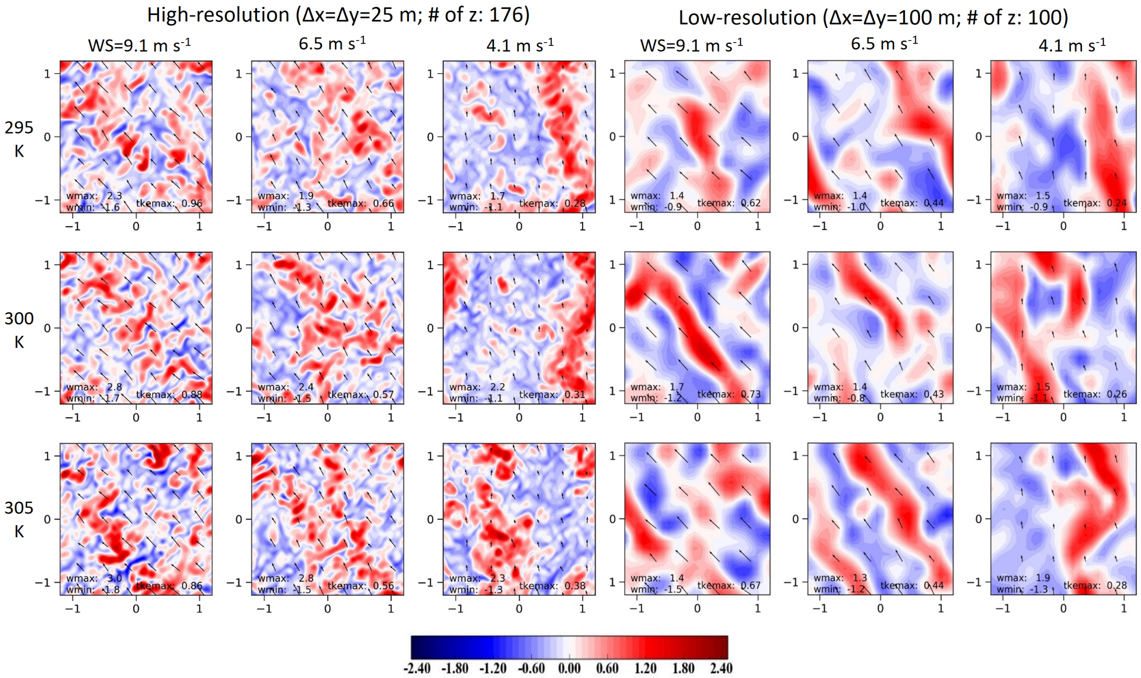

Figure 3.11. Horizontal view of vertical velocity (-2.5 to 2.5 m s^{-1}) at 500 m from nine sets of simulations (t = 16 h) for initial surface values of 295, 300, and 305 K potential temperature (top-to-bottom rows), and 9.1, 6.5, and 4.1 m s^{-1}vertically uniform wind speed (left-to-right columns) for high-/low-resolution simulations. The surface roughness is set to 0.1 m.

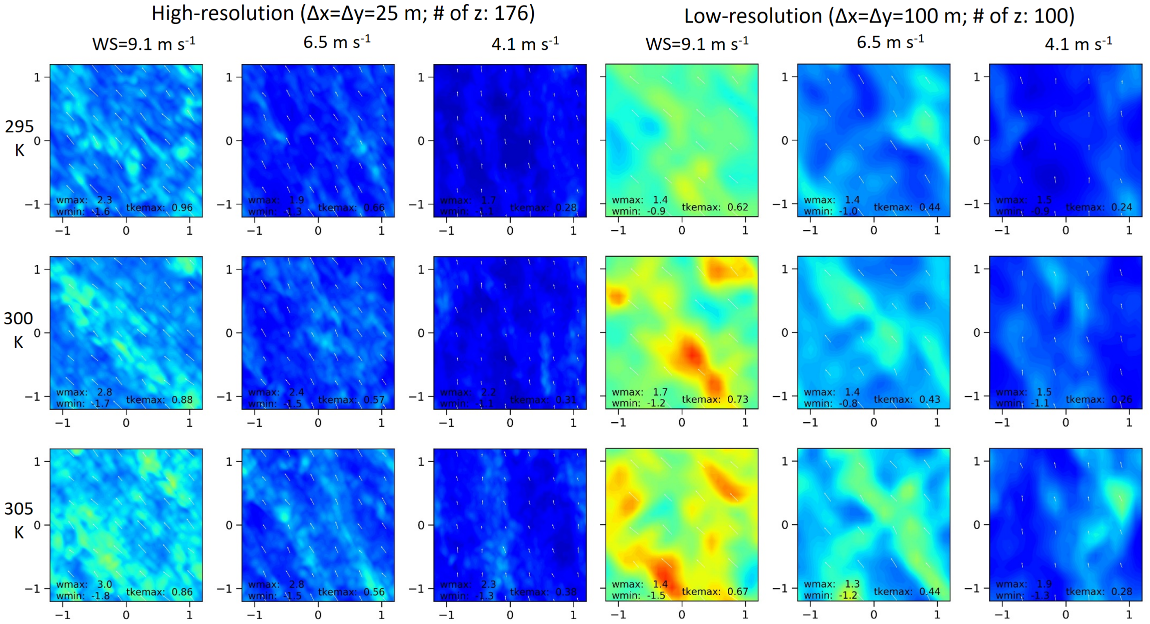

Figure 3.12. Vertically averaged turbulence kinetic energy (0 to 0.1 1 m^2 s^{-2}) from nine sets of simulations (t = 16 h) for initial surface values of 295, 300, and 305 K potential temperature (top-to-bottom rows), and 9.1, 6.5, and 4.1 m s^{-1} wind speed (left-to-right columns) for high-/low-resolution simulations.

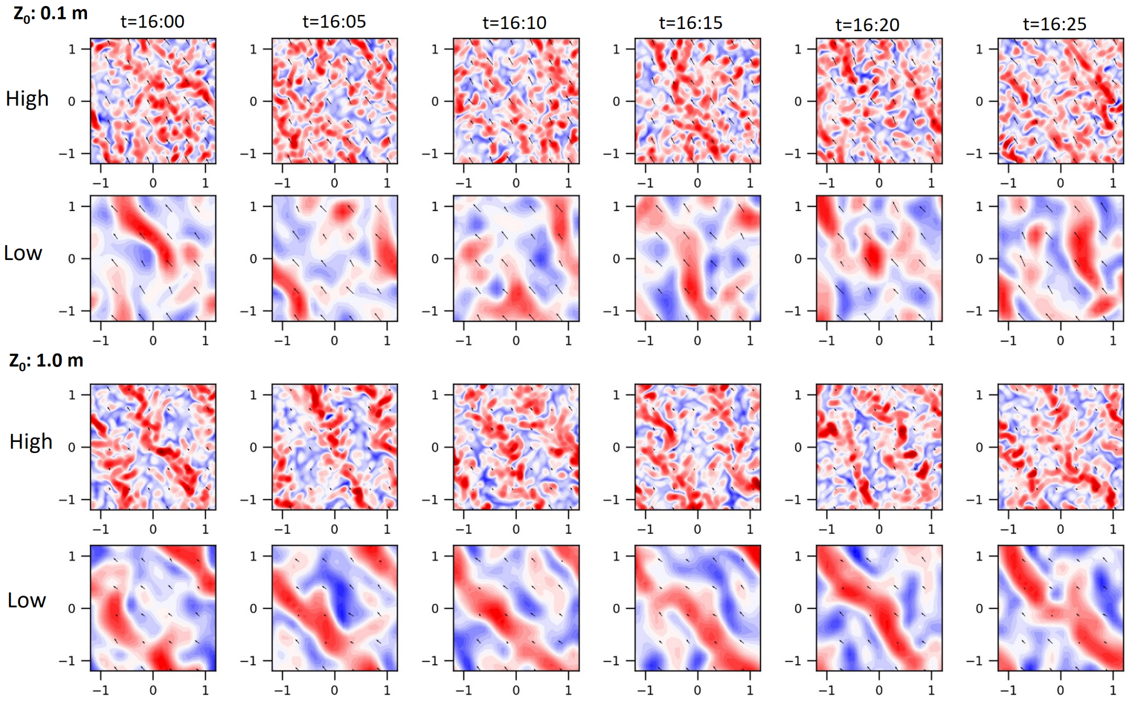

Figure 3.13. 5-minute evolution of vertical velocity (-2.5 to 2.5 m s^{-1}) at 500 m from the initial theta = 300 K and wind speed = 6.5 m s^{-1} setup for high-/low-resolution simulations and two settings (Z_0 = 0.1 and 1.0 m) of surface roughness.

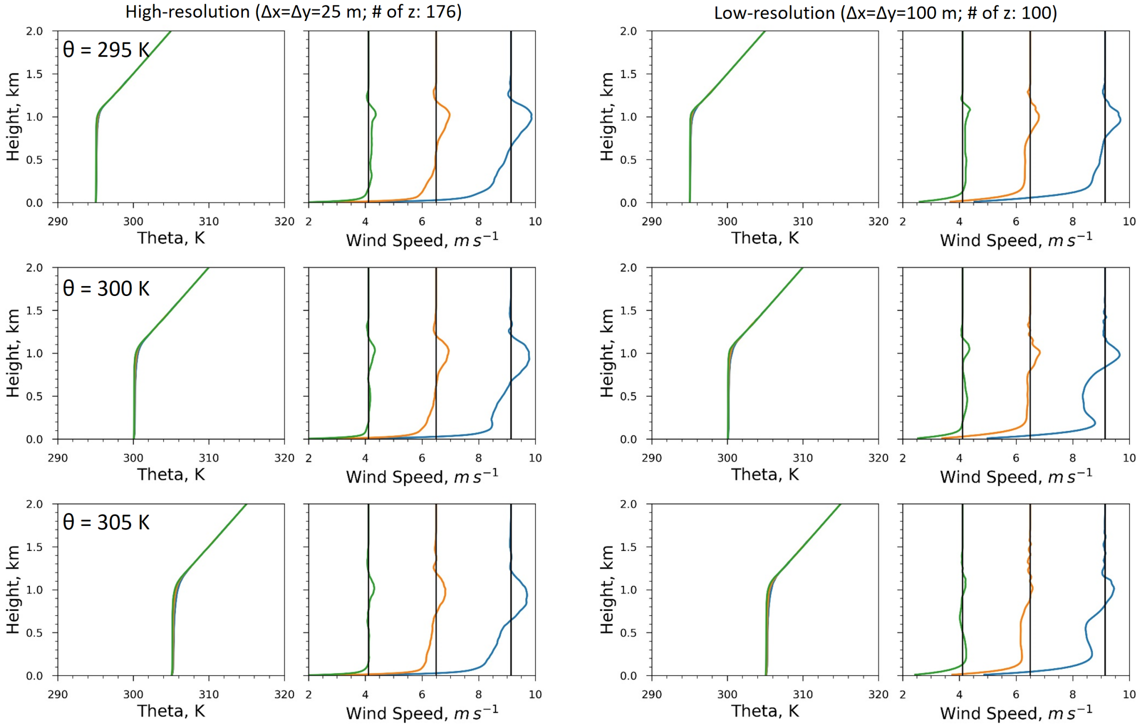

Figure 3.14. Horizontally averaged vertical profiles of θ and wind speed profiles from high-/low-resolution simulations for Z_0 = 1.0 m at 16 h.

3.2.2.2 Sensitivity to Boundary Conditions

In this section, we describe some attempts to test the sensitivity of results to initial and boundary conditions before testing the offline-coupling method. Although the simulations described in the previous section were run for 16 h, for ease of comparison, the simulations here were tested at more arbitrary integration periods. The time required for a simulation to reach a steady state depends on the flow configuration and surface roughness values. For example, Figure 3.15 shows turbulent eddies developing at about 1 h into the run. Regions of concentrated updrafts/downdrafts align with the mean flow further in the simulation similar to cloud streets observed in visible satellite imagery.

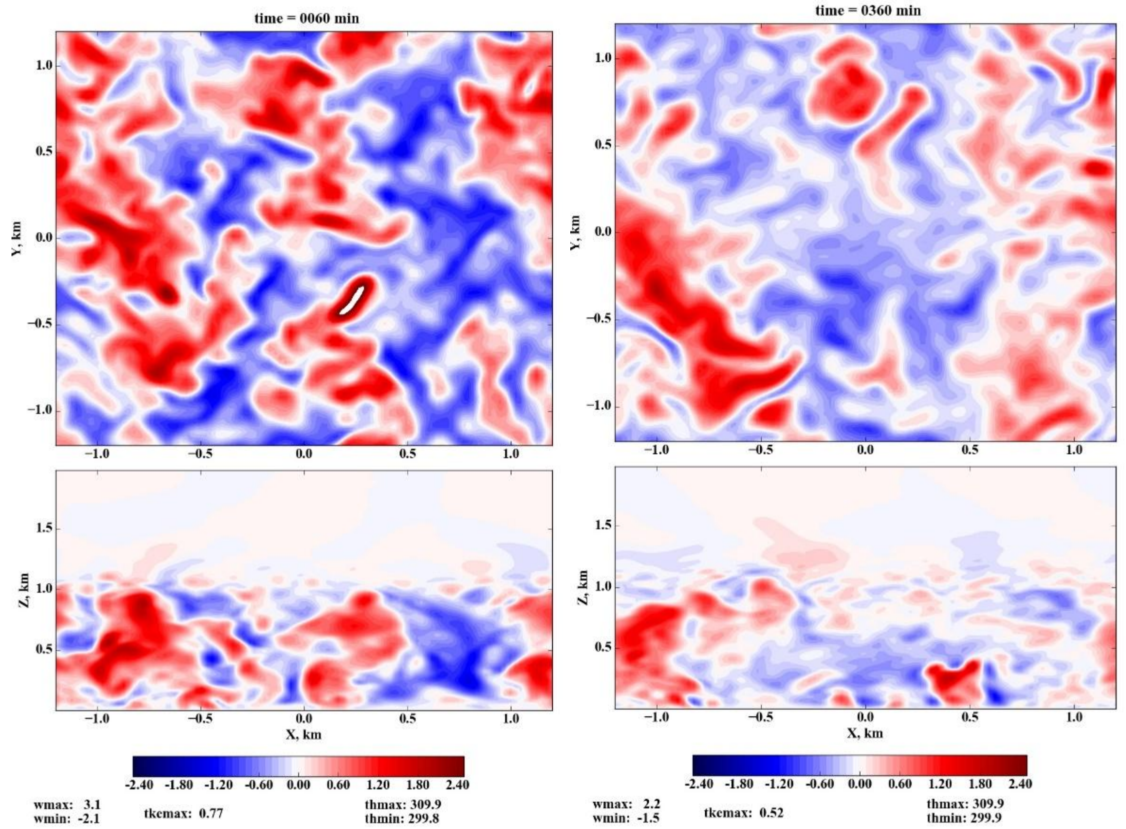

Figure 3.15. Vertical velocity profiles from periodic boundary simulations with $Z_0 = 0.1$ m (initial theta = 300 K, wind speed = 6.5 m s^{-1}). Top panels show horizontal cross sections at 500 m and bottom panels show vertical cross sections at y = 0 at 1 h (left) and 6 h (right).

When simulations are run with open boundary conditions, the flow cannot recycle within the domain, thus turbulent eddies do not develop as indicated in Figure 3.16 without the addition of perturbations. Periodic boundary conditions allow recycling of flow in a way that provides an infinite medium for flow to develop turbulent structures. However, in open boundary conditions, lateral boundaries are updated with the same input conditions at every time step, thus producing unrealistic flow behavior. The small-scale velocity couplets displayed in the bottom panels for 1 h into the run are manifestations of random perturbations included in the initial temperature field. As is apparent in the 6-h result (right panel), unrealistic numerically produced artifacts begin to appear in the domain. Although it is not shown here, running the simulation beyond about 9h results in an unreasonable Courant-Freidrichs-Lewy criterion.

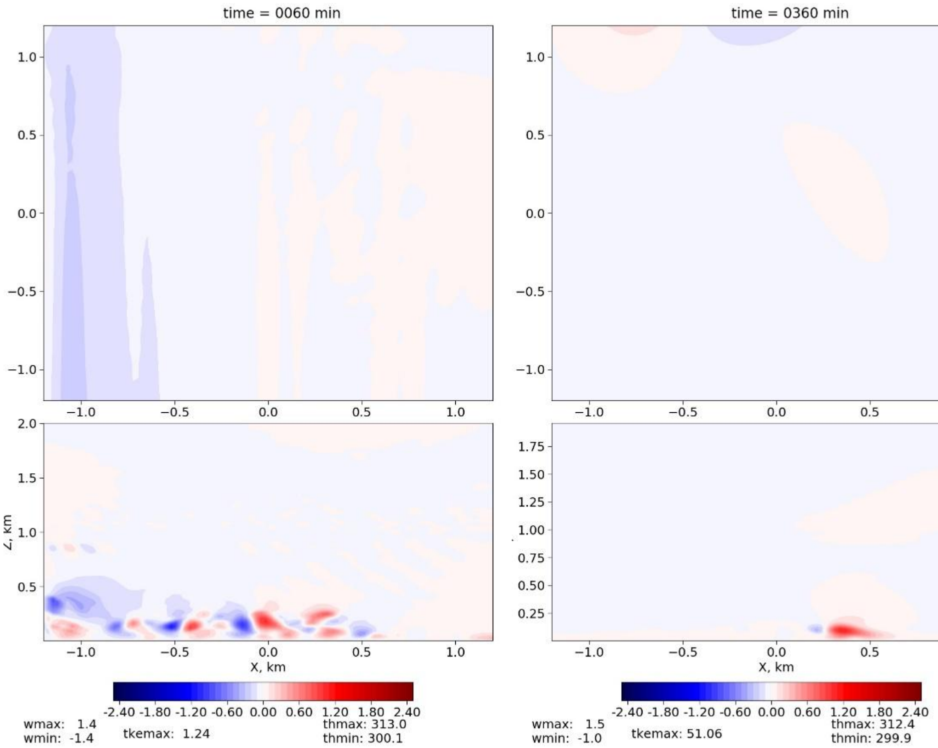

Figure 3.16. Same as Figure 3.15, but for open boundary initial conditions.

Although the potential temperature profiles for the two simulations are similar, substantial differences exist in terms of wind profiles (Figure 3.17). Although periodic boundary conditions capture the log-law evolution of wind within the lower boundary layer, open boundary conditions have large deficits of kinetic energy right above this region. Unrealistic upper-level wind profiles appear in the open boundary case 1 h into the simulation. Additionally, potential temperature is much higher in upper levels under open boundary conditions. This behavior might be indicative of inaccurate mass conservation in the modeling system.

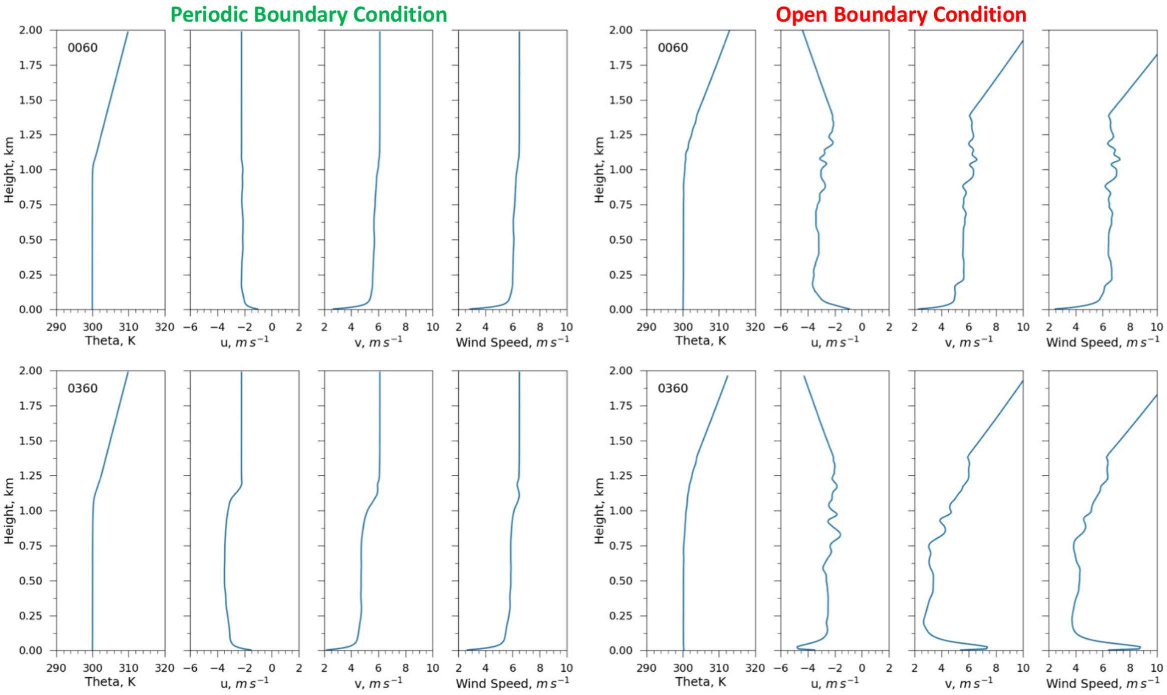

Figure 3.17. Horizontally averaged vertical profiles of θ and wind speed profiles from high-resolution periodic (left panels) and open (right panels) lateral boundary simulations for $Z_0 = 0.1$ m at 1 h and 6 h.

3.2.2.3 Single Sounding Initializations

One of the difficulties of simulating flow evolution within a small model domain is that turbulent structures do not have sufficient extent to evolve in a short domain. To alleviate this problem, the domain is extended by a factor of five in the streamwise direction. To keep the problem computationally feasible, the domain is initialized with a vertically uniform constant westerly wind of $u = 5$ m s^{-1} sounding. Figure 3.18 shows the vertical velocity profiles under three different scenarios. The first panel shows the result from a control run with the periodic boundary conditions at 1 h. Because the domain is five times larger than the previous setup, the simulations are only integrated for 1 h. For the second trial, we used the same domain configuration, but changed to open boundary conditions. In this case, turbulent flow is evident far away from the western boundary. However, further westerly advection of flow would disrupt the region with unrealistic features. Lastly, the open boundary simulation is initialized with a single sounding that is extracted from the periodic boundary case. Distinct differences are present in the flow structures compared to the laminar flow initialization case. However, the turbulent inflow case seems to be numerically more stable. A further extension of the domain is needed to better establish turbulent structures. Vertical profiles of wind speed show small differences within 100 m of the boundary layer. Both open boundary condition setups produce slower winds than the periodic boundary condition case.

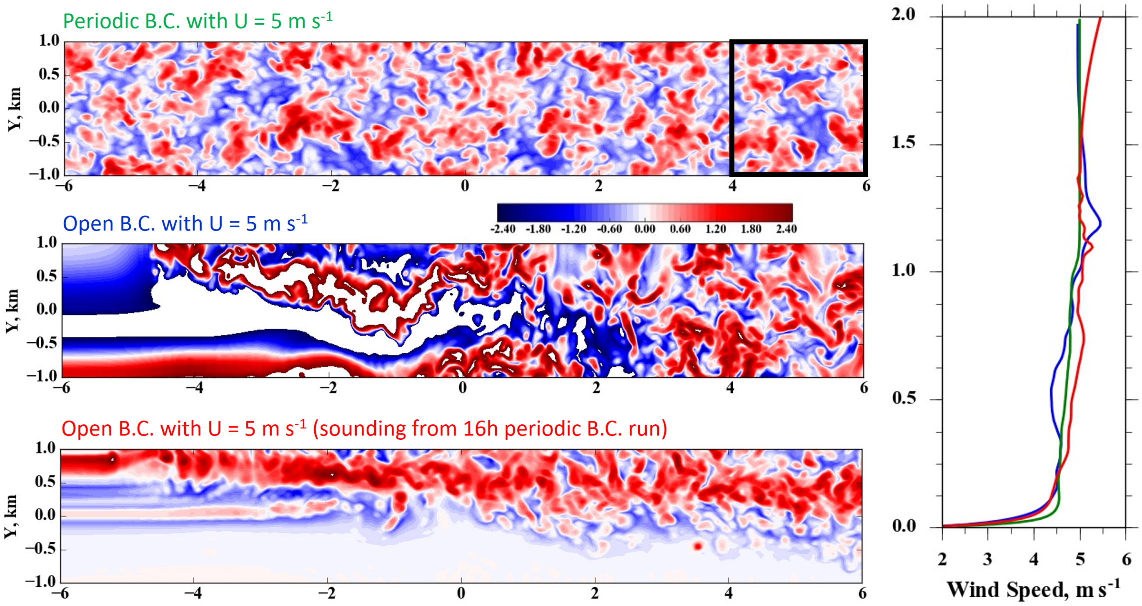

Figure 3.18. Horizontal view of vertical velocity (-2.5 to 2.5 m s^{-1}) at 500 m from vertically uniform u = 5 m s^{-1} simulations at 1 h for periodic and open boundary conditions. Note that the last simulation is initialized with a turbulent flow condition output from the 16-h periodic boundary simulation. The right panel shows the horizontally averaged wind speed profile within the last 2 km of the domain for each corresponding simulation.

3.2.2.4 Full 3-D Field Initialization

A single sounding initialization does not properly capture the turbulent flow features of well-established periodic boundary condition simulations. Therefore, we tested the idea of initializing open boundary condition simulations with full 3-D fields obtained from periodic boundary condition runs. Such an approach requires the use of identical domain lengths in both cases. This approach is based on the restart mechanism of the WRF model. We allowed the simulation to run 1 h, and then started another simulation by changing the boundary conditions to open without making any other change in the input parameters. Figure 3.19 shows the flow evolution for periodic and open boundary condition cases. Smeared flow features are present 10 minutes into the simulation in the middle panel. Further integration (bottom panel) results in unrealistic wave structures and stronger upward motion dominating the simulation. Given the 5-m s^{-1} westerly advection, flow features traverse about 3 km in 10 minutes; thus, the turbulent flow elements are advected out of the domain.

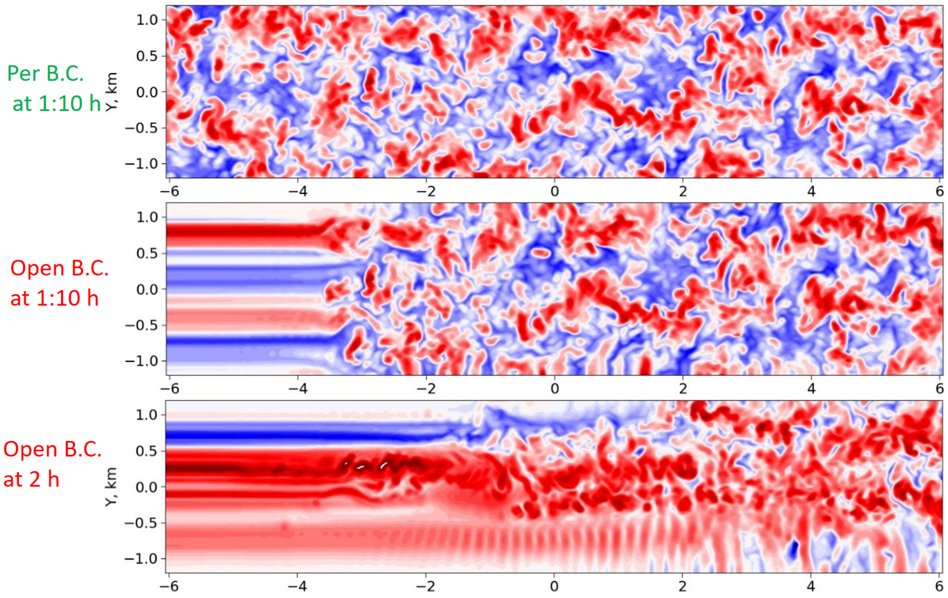

Figure 3.19. Vertical velocity at 500 m from vertically uniform $u = 5$ m s^{-1} simulations for a long (12-km) streamwise domain using periodic (at 1:10 h) and open (at 1:10 h and 2 h) boundary conditions.

3.2.3 Conclusions

A turbulent library development exercise was presented covering various atmospheric background states as well as sensitivity to model resolution. Preliminary results indicate that variations in surface roughness produce significant changes in flow structure especially near the surface. Although high-/low-resolution flow patterns and statistics are quite different, horizontally averaged vertical profiles of wind speed show good agreement due to ideal model setups. We highlighted some of the issues pertaining to the open boundary condition simulations and described the differences in flow characteristics. It was shown that domain size should be extended to allow eddies to be fully established. The extent of domain size is expected to be sensitive to incoming flow speed and model configuration. Despite the laminar incoming flow, open boundary condition simulation can produce turbulent eddies within an elongated domain. To make the problem computationally more feasible, wind direction and domain need to be rotated to reduce the two-dimensional complexity of the incoming flow. Additional experiments are ongoing to feed more frequent data slices into secondary simulations that are cycled from periodic boundary setups. Because it involves performing prior ensemble simulations to create a turbulence database and frequent data read/write to subsequent simulations, this approach may be slower than online coupling techniques. Asynchronous coupling is a viable approach to producing turbulence, yet we need to perform further experiments to demonstrate the practicality of the idea in more realistic modeling setups, such as simulating diurnal cycle variability. Detailed TKE analyses are required to assess the feasibility of the offline-coupling approach. The high-/low-resolution turbulence library can be a useful data set for machine-learning studies—to infer the relationship between low- and high-resolution features, for example.

3.3 Spectral Perturbations

The work discussed in this section builds upon the verification effort from year two of the MMC project (Haupt et al. 2017). Previously, our focus had been on developing a verification framework and velocity perturbation strategy within the SOWFA toolkit (Churchfield et al. 2012). To date, an optimal, code-agnostic inflow turbulence strategy remains to be determined. Therefore, our emphasis here is on evaluating and optimizing strategies that have previously been tested with SOWFA-LES and have shown reasonable success.

We started with an idealized precursor LES of a neutrally stratified PBL over flat terrain. The precursor is characterized by a horizontally periodic domain, which allows for the most energetic scales of turbulence to develop rapidly at the microscale but is not necessarily suitable for mesoscale-coupled simulation due to the periodicity constraint (unless additional internal forcings are applied from mesoscale tendencies). For the purposes of this study, the statistics from the precursor simulation were considered reference values for idealized MMC simulations on an aperiodic domain.

Idealized MMC simulations discussed herein are described by inflow-outflow boundary conditions under statistically stationary atmospheric conditions, where the pseudo-mesoscale inflow is a mean velocity profile extracted from the precursor as seen above. This inflow has been considered representative of a mesoscale inflow because it does not have any resolved turbulence at the microscale. For MMC purposes, synthetic velocity fluctuations have been superimposed on the mean flow to provide an enhanced mesoscale inflow with turbulence content. These perturbations in the mean field can be generated using a variety of methodologies, all of which modify the spectral content of the inflow and are expected to facilitate development of realistic turbulence within the LES.

An engineering approach to generating the velocity fluctuations is to specify a representative velocity spectrum and apply an appropriate model for spatial coherence. These capabilities are provided by the open-source TurbSim software (Kelley 2011). A more physically rigorous approach is to enrich the spectral content of the inflow using a kinematic simulation (KS) (Ghate and Lele 2017). Such an approach requires no empirical modeling and depends on the same parameters as the well-established Mann model (Mann 1994). Furthermore, the Gabor KS from Ghate and Lele (2017) is a more efficient, nonperiodic (and therefore less restrictive) application of rapid distortion theory than the original Mann model, and can model heterogeneous atmospheric conditions. However, this methodology was formulated with the assumption that the largest eddies have already been resolved in the flow field a priori, and the limitations of extending this spectral enrichment strategy from the quasi-homogeneous equilibrium range into the energy-containing range is explored in the study described here.

3.3.1 Application of Synthetic Velocity Perturbations

The current study focuses on neutral atmospheric conditions with an 8 m s^{-1} hub-height wind speed. Prior to evaluating purely mesoscale-driven conditions, stationary conditions were considered with the expectation that they represent a best-case scenario for inflow turbulence development. To promote the development of microscale turbulence, synthetic fluctuations were calculated by both TurbSim and Gabor KS, and superimposed onto the mean precursor inflow. Calculations were performed on an inflow-outflow domain with lateral and vertical dimensions identical to the precursor (3 km × 1 km) but extended in the streamwise direction (increased from 3 km to 15 km).

Precursor turbulence statistics were used for synthetic turbulence generation under the assumption that these data will be available from a mesoscale model or local measurements at the site of interest. Variances were used to the scale fluctuations with height to introduce vertical inhomogeneity (Figure 3.20). The Kaimal spectral model in TurbSim, appropriate for neutral atmospheric stability, was applied with the default parameters according to the International Electrotechnical Commission (IEC) 61400-1 standard (2014). In addition, spatial coherence in the u-component of velocity alone was imposed, also using IEC standard parameters (Jonkman and Buhl 2007). For Gabor KS, the input length scale and shear parameters were tuned to achieve a specified streamwise velocity gradient and cross-correlation in u- and w-velocity components. These specified values were taken to be the gradient and spatial average <uw> at hub height.

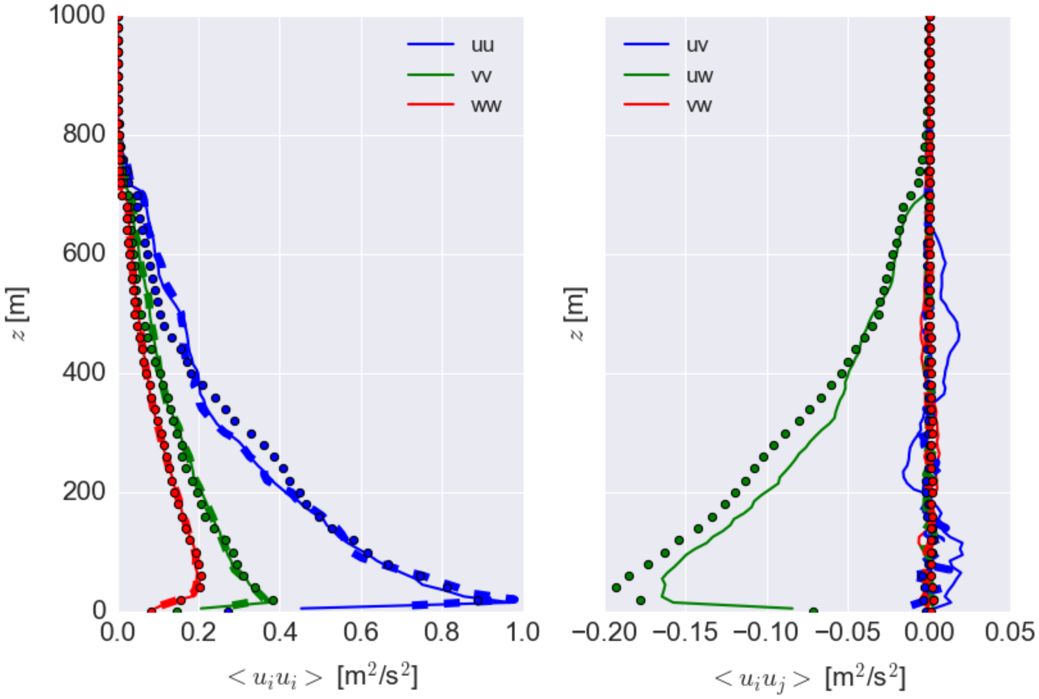

Figure 3.20. Variances and covariances for the reference precursor (solid lines), scaled TurbSim inflow (dashed lines), and scaled Gabor KS inflow (symbols) cases.

From the inflow-outflow simulations, the streamwise evolution in TKE indicate that the fetch for the idealized case (with LES-resolved precursor inflow) is approximately 3 km to 4 km (Figure 3.21). If synthetic velocity fluctuations are superimposed in an idealized MMC case, the observed fetch is not well-defined. For TurbSim-enhanced inflow, the fetch may be considered to be approximately 5 km based on TKE, but the energy is seen to gradually decay with distance from the inlet. In the case of Gabor KS-enriched inflow, the turbulence appears to be developed at about 8 km, but then the flow transitions to another quasi-equilibrium state after 12 km. Moreover, the TKE is underpredicted throughout most of the computational domain in both cases.

A possible cause of this discrepancy in the TurbSim-enhanced inflow simulation is the lack of correlation between *u*- and *w*-fluctuating velocity components. Because there is no spatial coherence in *v*- or *w*-components, the cross-correlations responsible for TKE production are effectively zero at the inlet (Figure 3.20). As a result, the proper correlations are not guaranteed to develop in a manner that is consistent with the precursor, and the resulting inflow-outflow solution may reach a different quasi-equilibrium state.

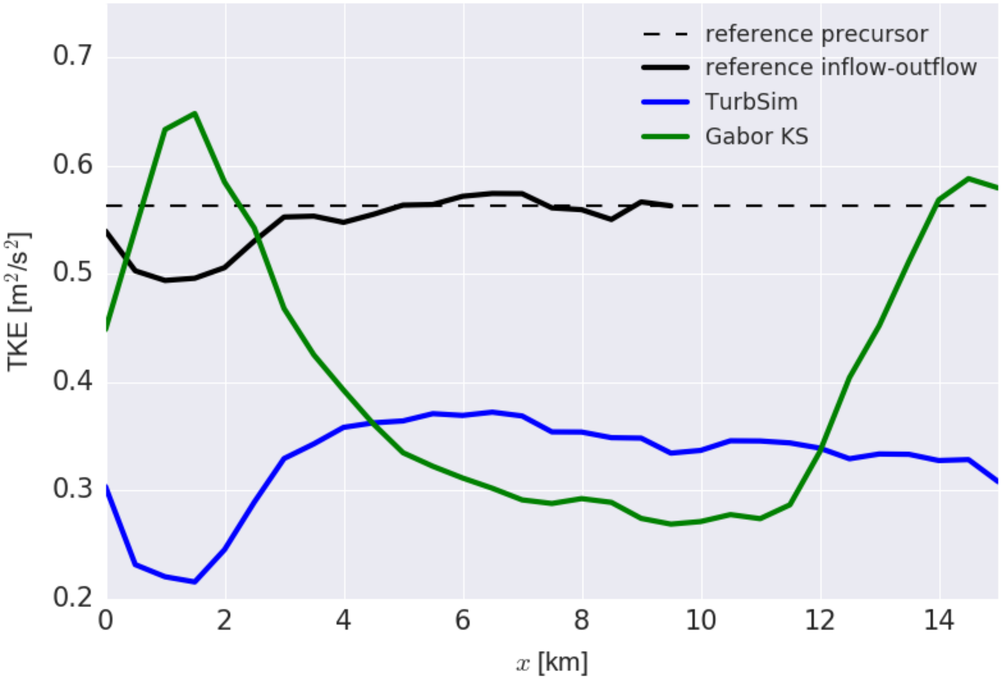

Figure 3.21. Streamwise evolution of turbulence kinetic energy in LES with idealized MMC.

A visual assessment of the flow fields shows the fetch to be approximately 10 km in the TurbSim-enhanced case (Figure 3.22) and approximately 4 km in the Gabor KS-enriched case (Figure 3.23). These qualitative estimates differ from the previous analysis of TKE. In addition, the nominally developed fields differ significantly in observed length scales; the Gabor KS tends to promote development of very large turbulence structures very quickly, indicating that the Gabor KS inputs should be further tuned. These inconsistencies between quantitative and qualitative analyses also motivate a more rigorous analysis based on two-point statistics in order to adequately quantify fetch.

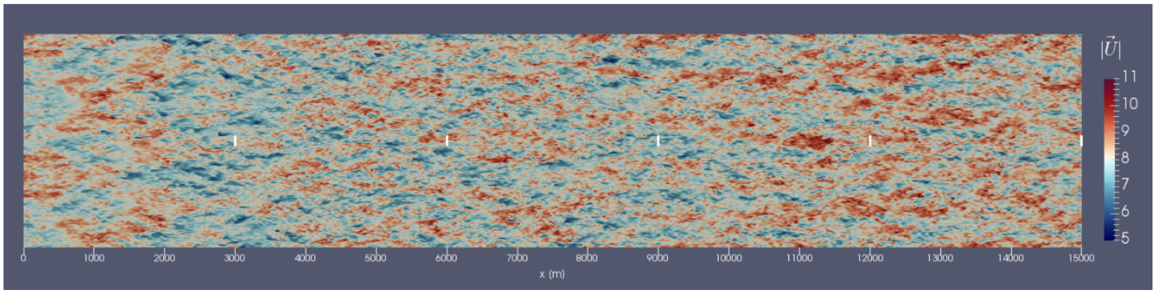

Figure 3.22. Idealized MMC with TurbSim-enhanced inflow; vertical lines indicate sampling locations for the aeroelastic study using FAST.

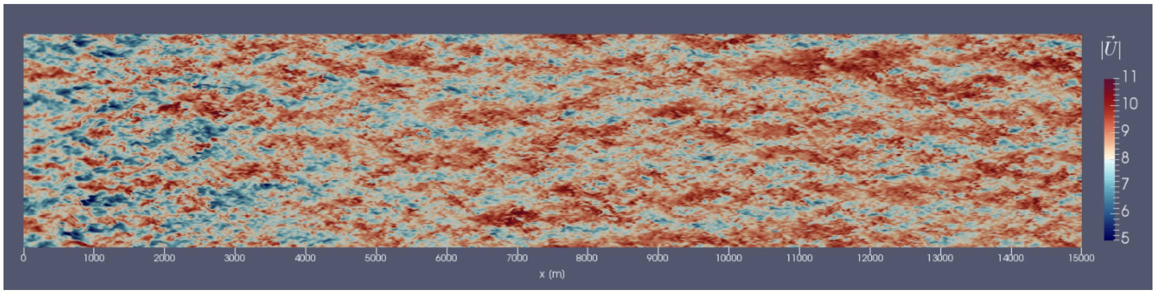

Figure 3.23. Idealized MMC with Gabor KS-enriched inflow.

3.3.2 Aeroelastic Simulation of Generated Inflows

To directly assess the impact of inflow at varying stages of turbulence development on wind turbine performance and loads, the flow field driven by the LES mean flow and superimposed synthetic turbulence has been sampled to provide inflow to the FAST aero-hydro-servo-elastic engineering model (Jonkman and Buhl 2005), in a framework similar to the FAST.Farm wind-plant multiphysics analysis (Jonkman et al. 2017). OpenFAST, the latest and currently supported version of FAST, was then run to calculate turbine performance and loads. The quantities of interest (QOIs) relevant to wind turbine and wind-plant design considered here include the following:

- maximum rotor power, to measure turbine performance;
- maximum blade root bending moment (from the vector sum of flap- and edgewise moments), a measure of the ultimate load experienced by a blade;
- standard deviation in blade root flapping moment, a proxy for fatigue loading; and
- standard deviation in blade root edgewise moment.

Each of the QOIs was averaged over an ensemble of 30 samples. In the case of standalone OpenFAST, 30 random seeds were used to generate 30 different TurbSim synthetic inflow fields. In the case of LES inflow, 30 different inflow planes were sampled from the SOWFA precursor at equally spaced streamwise locations. The sampling was also equally spaced in the lateral direction to further decorrelate the velocity fields. OpenFAST was then run for 10 minutes of simulation time, and the initial 30 s were excluded from the statistics calculations to remove startup transients from the statistical analysis.

The convergence of the four selected QOIs is illustrated in Figure 3.24 and Figure 3.25 for the reference TurbSim and SOWFA-LES cases, respectively, where each QOI has been normalized by the mean including all 30 samples. The statistics converge to within 2% of the final value after 12 simulations in all quantities for the synthetic TurbSim-generated inflow. In comparison, the inflow provided by LES results in a larger range of QOI values and all statistics converge to within 2% after 24 simulations.

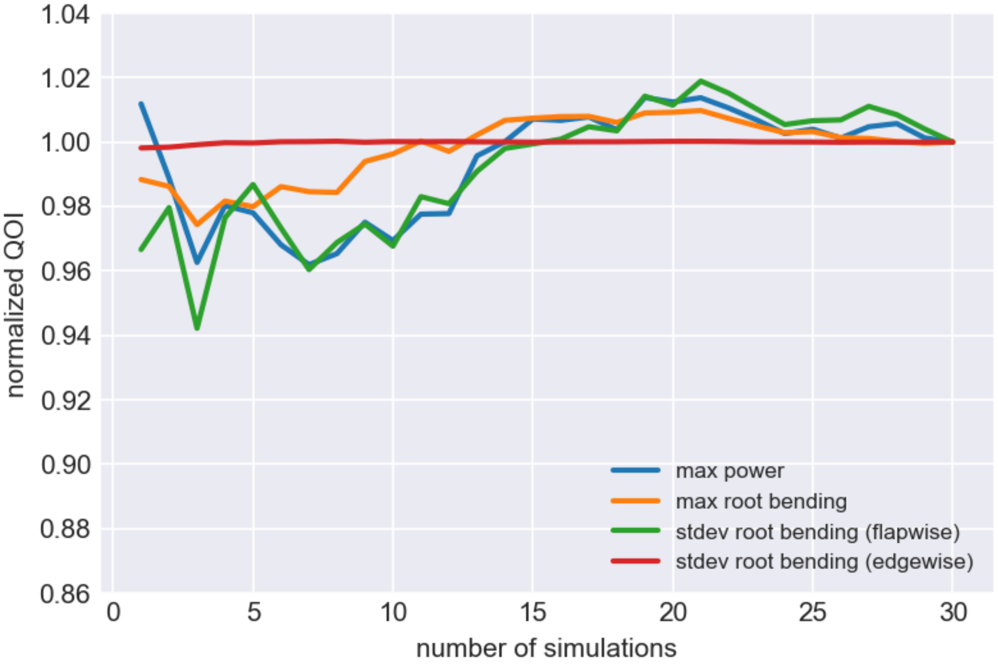

Figure 3.24. Averaged QOIs from FAST simulations with TurbSim inflow.

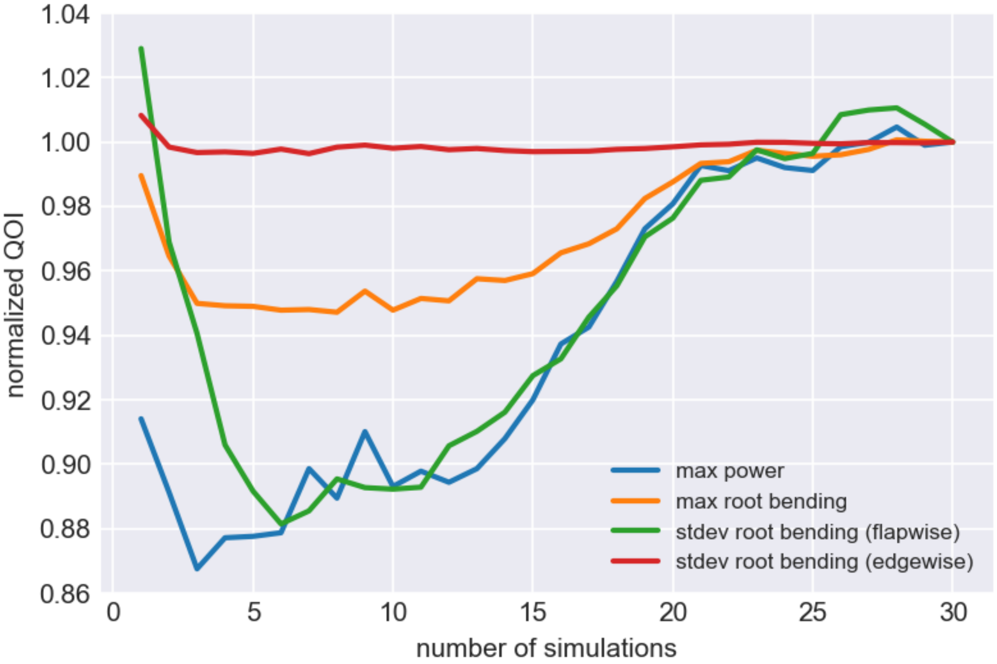

Figure 3.25. Averaged QOIs from FAST simulations with SOWFA-sampled inflow.

To evaluate the impact of fetch on turbine performance and loads, rotor inflow planes were sampled within an idealized MMC simulation (with TurbSim-enhanced inflow) at the locations indicated in Figure 3.22. The impact of the streamwise variations in the developing flow has been characterized in terms of the previously specified QOIs (Figure 3.26). For all metrics shown, there is reasonable agreement between the ranges of observed reference values, and the LES results consistently have a larger range and lower mean. For the cases with steady inflow, both the uniform case and nominal shear cases have been included to distinguish the effects of turbulence from shear. The steady inflow results indicate that the maximum rotor power has little dependence on the turbulence field under these conditions (the cases with and without shear produce identical power due to the action of the torque controller) compared to the reference case with TurbSim inflow. Although edgewise moments are driven primarily by cyclic variations in the mean flow due to shear, the flapwise bending moments are more significantly augmented by turbulence (17% and 52% for the maximum and standard deviation in flapwise root bending moments, respectively).

At the farthest distance downstream of the inlet, the idealized MMC flow field produces rotor power output similar to both the TurbSim and SOWFA reference simulations. However, for the QOIs based on blade-bending moments, the MMC field converges to downstream values that are consistently lower than the reference TurbSim simulations; in the case of blade root flapwise bending moment, the MMC flow produces moments that are more than a standard deviation less than both reference simulations.

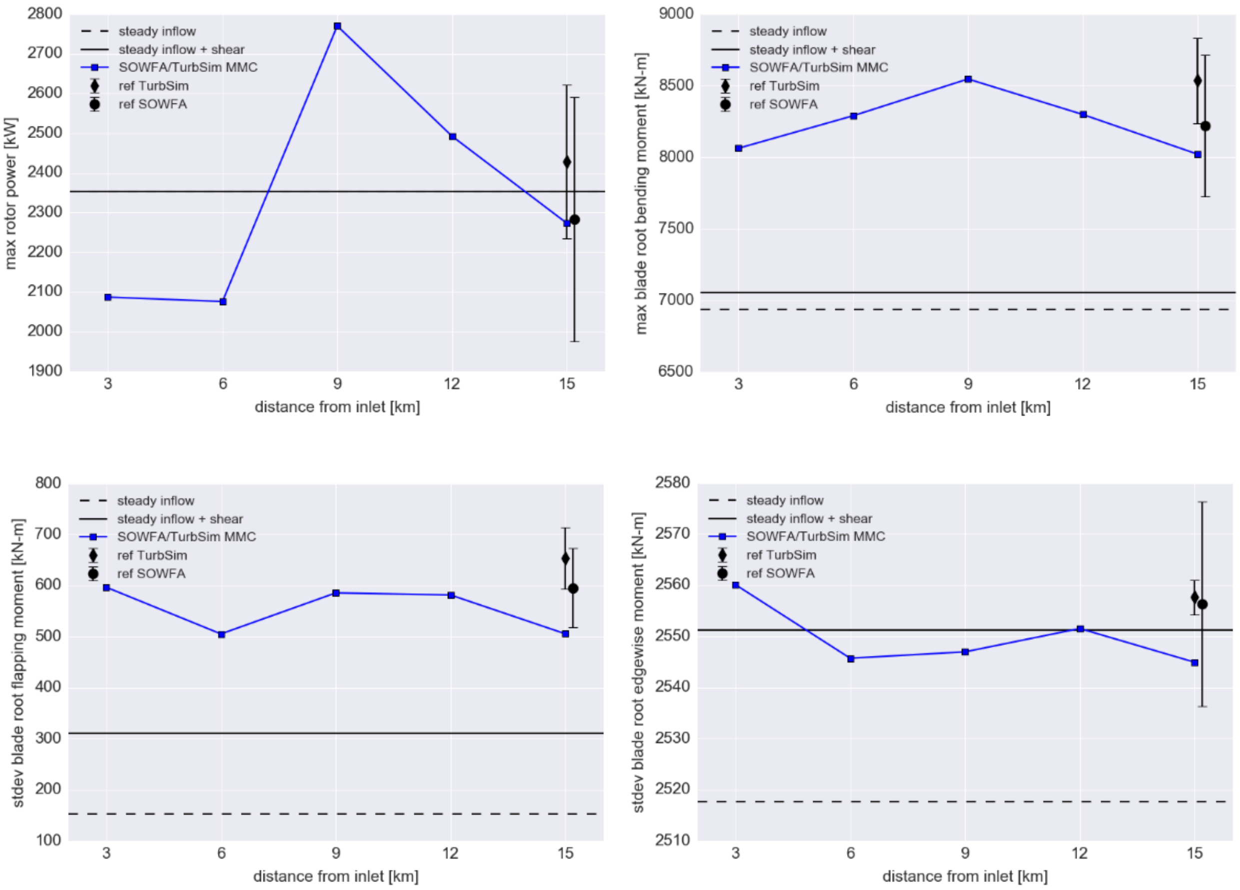

Figure 3.26. Streamwise variation in QOIs from FAST simulation driven by various inflows.

3.3.3 Conclusions

We have demonstrated in this year's work that a fully developed turbulent flow driven by an idealized MMC inflow may be simulated using SOWFA with observed fetches of approximately 10 km or less. From a turbulent flow perspective, a more sophisticated perturbation strategy may be needed to ensure that realistic physics—comparable to a standalone LES precursor simulation—are developed. For the TurbSim-enhanced inflow, modeling of spatial coherence in all velocity components may be essential to develop the correct amount of TKE in the flow. If not, naïvely imposing a coherence model may in effect modify the inflow in an unpredictable manner. For the Gabor KS-enriched inflow, it is also possible that forcing the variances of the synthetic turbulence to conform to the precursor profile through scaling may also effectively modify the inflow in an unpredictable manner and drive the solution to a different quasi-equilibrium as well.

From an engineering perspective, we have demonstrated that the maximum power output may be reasonably predicted based on the mean flow alone. This suggests that the mesoscale impact on wind-plant performance may be reasonably captured at the microscale with a fully developed flow, even given differences in turbulence characteristics. However, accurate prediction of loads will require more careful treatment of the microscale turbulence, especially within the context of fatigue and turbine life as indicated by the calculated standard deviation in blade root flapwise bending moment. This is especially challenging because of the large degree of variability in the simulated flow, both with and without MMC. To obtain representative statistics, more repetitions or longer time series may be needed, thus requiring additional computational expense.

3.4 Stochastic Temperature Perturbations in Real-Data Cases

3.4.1 Computational Setup

In this section, performance of the stochastic cell-perturbation method (SCPM) of Muñoz-Esparza et al. (2015) (referred to here as ME15) is examined in a real-data case consisting of a portion of a diurnal cycle occurring on 8–9 November 2013 at the SWiFT site near Lubbock, Texas, and spanning the convective late morning through the evening transition and into the nocturnal nighttime period. Figure 3.27 shows contours of terrain height from the WRF simulation in and surrounding the site location. The positions of the two nested LES domains, d02 and d03, within the parent domains, are indicated by the blue squares. The terrain contours indicate generally uniform terrain with shallow slopes in and around d02 and d03.

WRF was run with one mesoscale domain and two LES domains nested within the mesoscale. The simulations were forced with the Global Forecast System analysis and used a full suite of physical process parameterizations, including microphysics, radiative transfer, PBL, surface layer, and land-surface physics. The LES domains used the nonlinear backscatter and anisotropy (NBA) SGS turbulence model (Kosović 1997) that does not use SGS TKE (NBA1; Mirocha et al. 2010). Table 3.1 contains parameters specifying the physical characteristics of the nested domain configurations.

The SCPM of ME15 applied herein used three rows of 8×8 gridcells in each horizontal direction at each inflow plane. A unique perturbation value was applied at each model vertical index up to a height of $0.667z_i$, where the PBL depth, z_i, was passed down to the LES domain(s) from the mesoscale domain, which used the MYNN 2.5 PBL scheme, both to specify turbulence fluxes and to diagnose z_i. The inflow planes were determined by evaluating the wind direction along each lateral boundary at a height of $1.1z_i$, which was taken to represent a geostrophic wind speed V_g. The perturbation magnitude was determined to be $\acute{\theta} = V_g^2/(E_T C_p)$, following ME15, where $E_T = 0.16$ is the optimal value of the turbulent Eckert number. The perturbations were refreshed over an advective timescale determined from $\Delta t_p = (0.875/\cos \emptyset) n_{gc} n_c \Delta x/V_{SL}$. Here, $n_{gc} = 8$ is the number of grid cells composing each perturbation cell, $n_c = 3$ is the number of cells in the transverse direction to the boundary, $0 \leq \emptyset \leq \pi/4$ is the angle of the inflow with respect to either lateral boundary, which elongates Δt_p to provide additional time for flow to advect across a square perturbation region at any non-right angle. $0.875 = 21/24$ accounts for the relaxation zone used along the interior grid points adjacent to the lateral boundaries on nested domains, over which the impacts of the perturbations are diminished due to relaxation toward the Dirichlet boundary condition specified along each edge. The simulations herein used a Dirichlet boundary condition on the one gridpoint defining the perimeter of the nested domain, and applied linear relaxation over grid points 2 through 5 into the nested domain interior. Scaling by $21/24$ assumes that the Dirichlet point, and the first 2 of the 4 relaxation points, will be compromised by the relaxation.

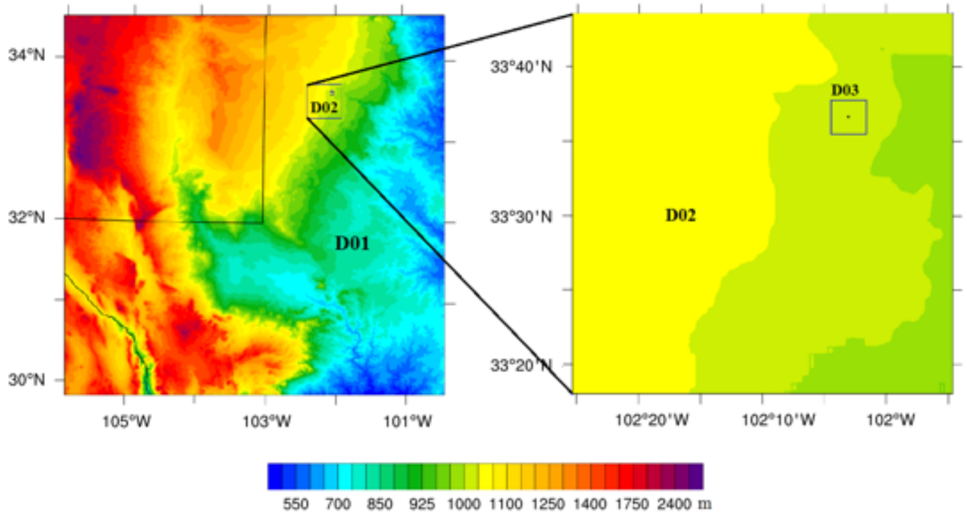

Figure 3.27. WRF nested domain setup for MMC simulations at the SWiFT site.

Table 3.1. WRF domain setup for the 8–9 November 2013 simulations at the SWiFT site.

D01			D02			D03			*nz*
nx	*Ny*	Δx [m]	*nx*	*ny*	Δx [m]	*nx*	*ny*	Δx [m]	
529	529	990	529	529	90	433	433	10	160

3.4.2 Results

Figure 3.28 shows instantaneous contours of horizontal wind speed V_h from 1800 UTC (12:00 p.m. Central Standard Time) from the SWiFT case at 100 m above the surface. The left panels are from the coarsest LES domain nested within the mesoscale domain (mesoscale solution not shown), while those to the right show the finer LES domain nested within the coarser LES. The location of the fine domain is indicated by black dotted lines within each panel. The top row shows simulations with no SCPM on the coarsest LES domain, d02.

Even in the absence of the SCPM, turbulence develops spontaneously due to convective forcing (heat fluxes of about 200 W m^{-2}). The top middle panel shows the finer LES domain with no SCPM applied on either domain, while the rightmost top panel shows the SCPM applied to d03 only. The bottom left panel shows the effect of SCPM applied to d02, which accelerates turbulence development relative to the convective forcing alone. Not only does the turbulence form more quickly, the strong correlations in the streamwise direction are reduced by the SCPM. The lower middle panel shows the effects of the SCPM d02 only, while the rightmost panel uses the SCPM on both d02 and d03. Because of the strong convective forcing, application of the SCPM to d02 makes little difference to the flow structures within d03, due to the large upstream fetch. However, application of the SCPM to d03 does accelerate the formation of smaller-scale turbulence within d03.

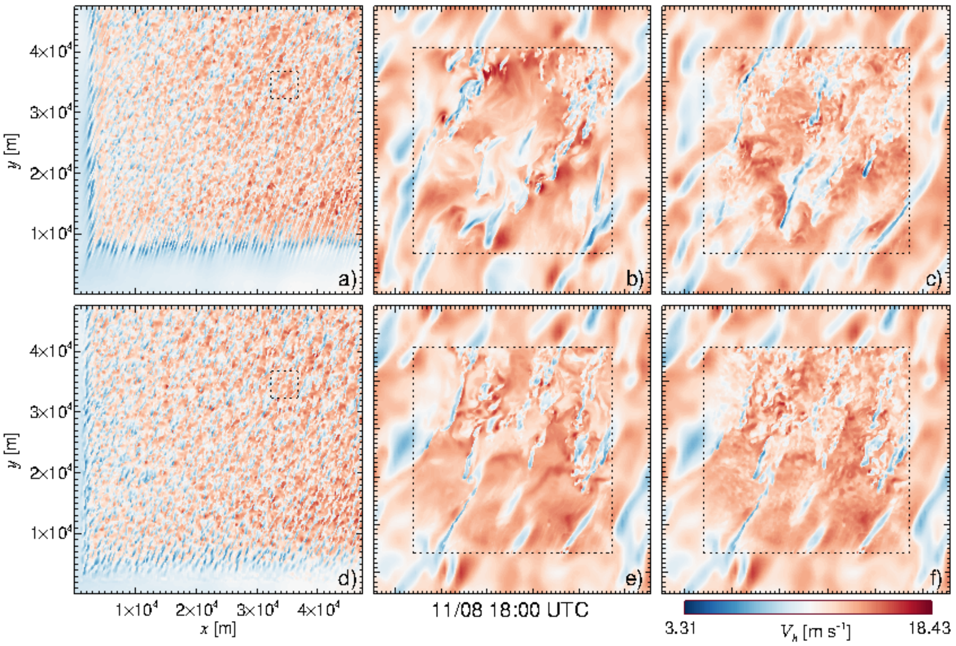

Figure 3.28. Instantaneous plan view of wind speed at 100 m above the surface from the SWiFT simulation during convective conditions. Left panels (a,d) show d02, middle and right panels show d03 located within a portion of d02. Top row: SCPM not applied on d02, (b) no SCPM on d03, (c) SCPM on d03 only, (e) SCPM on d02 only, and (f) SCPM on d02 and d03.

Figure 3.29 shows data from the same simulation a few hours later, during the evening transition, when the atmospheric heat flux transitioned from small positive to small negative values. In spite of the near neutrality near the surface, weak convective roll features persisted within the residual PBL. However, the formation of smaller-scale turbulence was delayed relative to the convective conditions a few hours earlier. As with the earlier time, the smaller scales resolvable within the LES meshes appeared on d02; however, application of the SCPM considerably accelerated the formation of smaller scales within d03. Although the application of the SPCM on d02 did not appear to strongly influence the turbulence on d03, it is clear that a smaller d02 could be used in the presence of the SPCM to ensure turbulent inflow into d03.

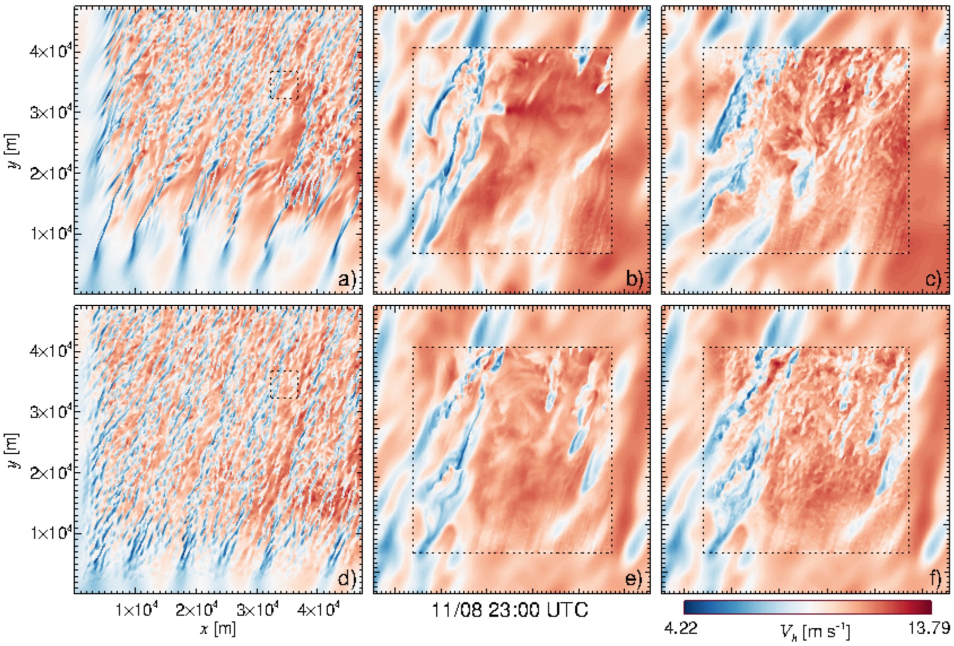

Figure 3.29. As in Figure 3.28, but 5 h later during the evening transition.

Figure 3.30 shows data from the same simulation a few hours after local sunset, after which the PBL has transitioned to being stably stratified, with surface heat fluxes of around -10 W m^{-2}. It is clear that application of the SCPM on d02 is irrelevant, due to the 90-m mesh spacing on d02 being insufficient to maintain turbulence during the stably stratified conditions. It is likewise clear that, in the absence of the SCPM, turbulence does not spontaneously develop on the finer 10-m mesh spacing on d03.

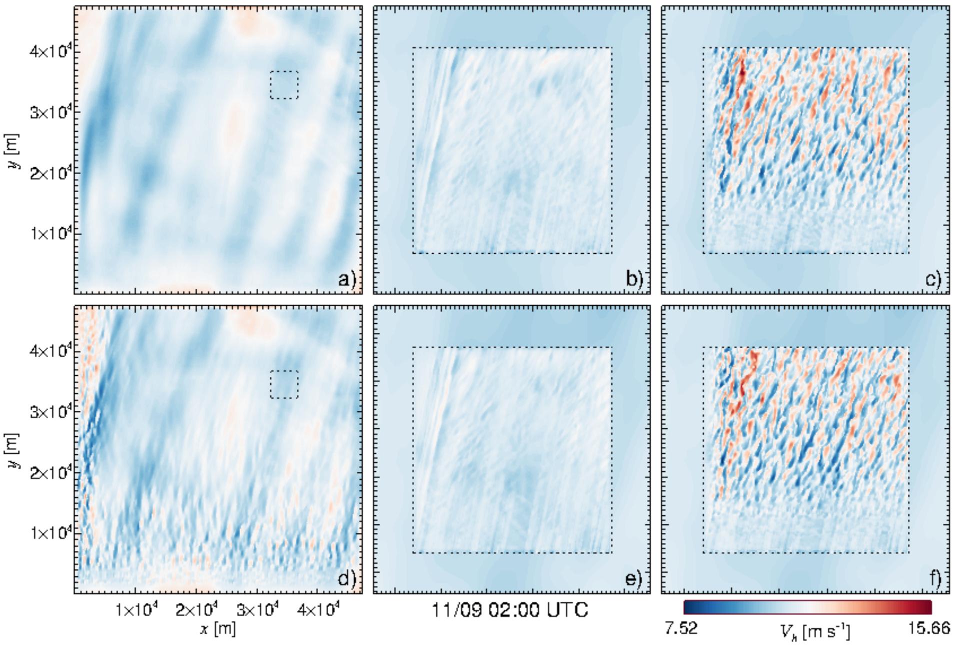

Figure 3.30. As in Figure 3.29, but 3 h later during stable nocturnal conditions.

Although application of the SCPM on d03 is seen to generate a turbulent flow field, the fetch required is still rather large. In such a case, it would be prudent to either reduce the size of d02, reduce its mesh spacing until turbulence is supported (following application of the SCPM), or eliminate it entirely, and instead increase the size of d03 to allow sufficient upstream fetch for the turbulence field to fully form upstream of the area of interest.

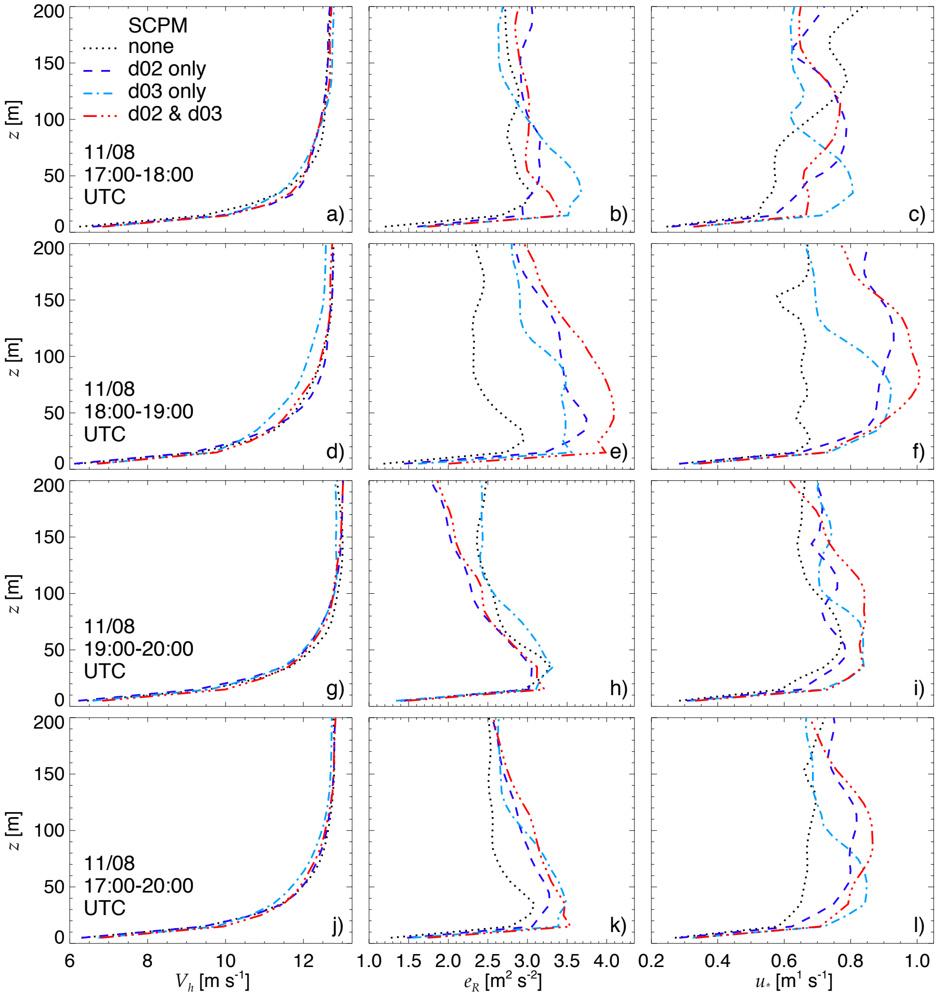

Figure 3.31. Time-averaged profiles of wind speed V_h, resolved turbulence kinetic energy e_R and resolved friction velocity u_* from the d03 grid point nearest the SWiFT facility.

Figure 3.31 shows profiles of time-averaged wind speed $V = \left(\overline{u_i^2}\right)^{1/2}$, and resolved components of the TKE, $e_R = \left(\overline{\acute{u}_i\acute{u}_i}\right)/2$, and the friction velocity $u_* = \left[\left(\overline{\acute{u}_1\acute{u}_3}\right)^2 + \left(\overline{\acute{u}_2\acute{u}_3}\right)^2\right]^{1/4}$ from the simulations. Here, $i = 1,2,3$ denotes zonal, meridional, and vertical velocity components, and primes denote departures from time-averaged values, with time averaging denoted by overbars. The profiles shown in Figure 3.31 and similar profiles were obtained from output at 1 Hz from the WRF model grid point nearest to the meteorological tower at the SWiFT facility (which was not used in the analysis that follows). An averaging time of 20 minutes was used to compute the departures. Profiles are shown from d03 of simulations with no SCPM, SCPM on d02 only, SCPM on d03 only, and SCPM on both d02 and d03, as identified in the legends. As demonstrated in Figure 3.31, which shows profiles obtained during convective conditions, there is significant time variability in the flow due to the presence of large convective rolls. As such, the top three rows of Figure 3.31 show quantities averaged over 1 h (averages over three 20-minute averages), while the bottom row shows the average over all 3 h.

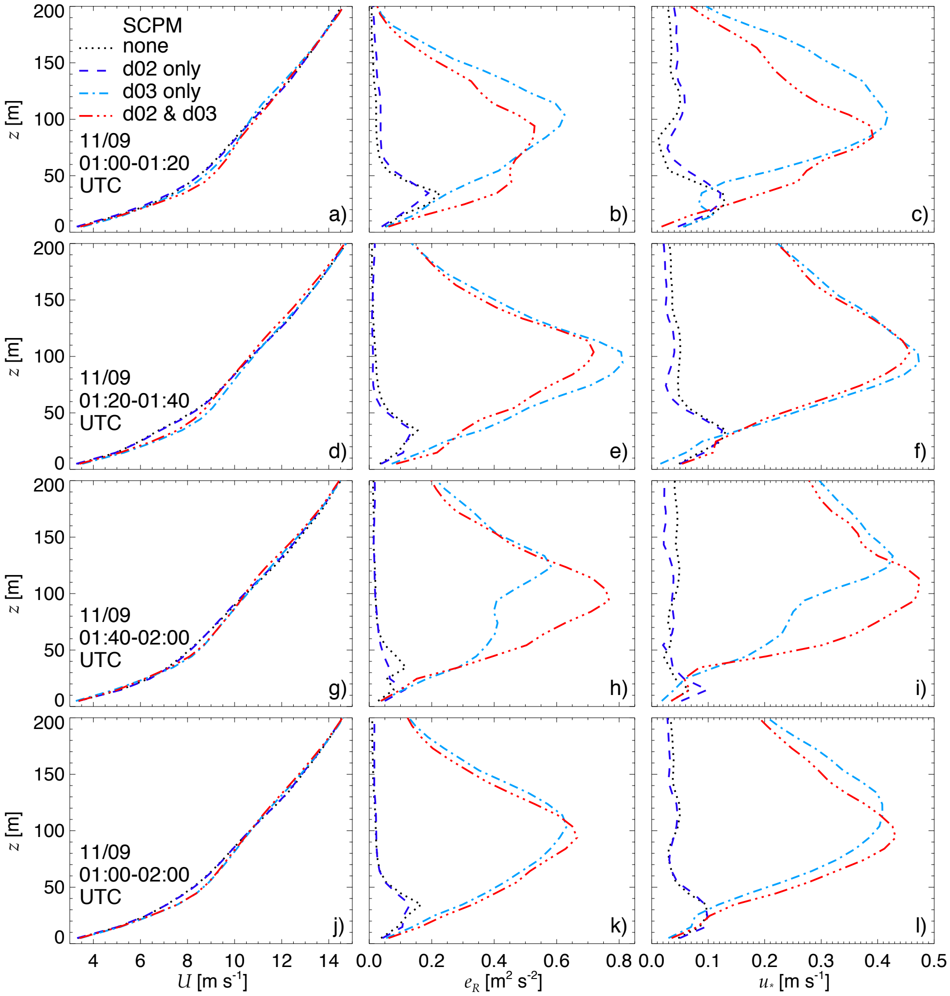

Figure 3.32. As in Figure 3.31, but during stable conditions.

Application of the SCPM has little impact on V_h, but not using it on either domain yields considerably smaller magnitudes of e_R and u_*. Simulations using the SCPM on d03 produce the largest magnitudes of e_R and u_*. Application of the SCPM to d02 in addition to d03 does not change the profiles considerably from application to d03 only, due to strong convection leading to turbulent flow on d02, regardless of the SCPM.

Figure 3.32 shows the same information as Figure 3.31 but for stable conditions, for which the surface sensible heat flux was around -10 W m^{-2}. Here, the top three rows show 20-minute average values, and row four shows the average over 1 h. As also seen in the instantaneous velocity contours of Figure 3.30, application of the SCPM on d02 has little influence on the profiles, due to the stability relative to the grid spacing. Application of the SCPM to d03 is seen to generate realistic distributions of e_R and u_*.

3.4.3 An Additional Case Study at the WFIP 2 Site

Performance of the SCPM was also examined over the WFIP 2 site, spanning the late morning through afternoon of 12 November 2016, the same case described in Chapter 5. Figure 3.33 shows contours of terrain height from the WRF simulation in and surrounding the site location, as in Figure 3.27, showing the much more complex terrain within the Columbia Gorge. Table 3.2 indicates the domain configurations of the WRF model, similar to those used at the SWiFT site, but with a slightly larger and more elongated d02, in order to include Mount Hood within it.

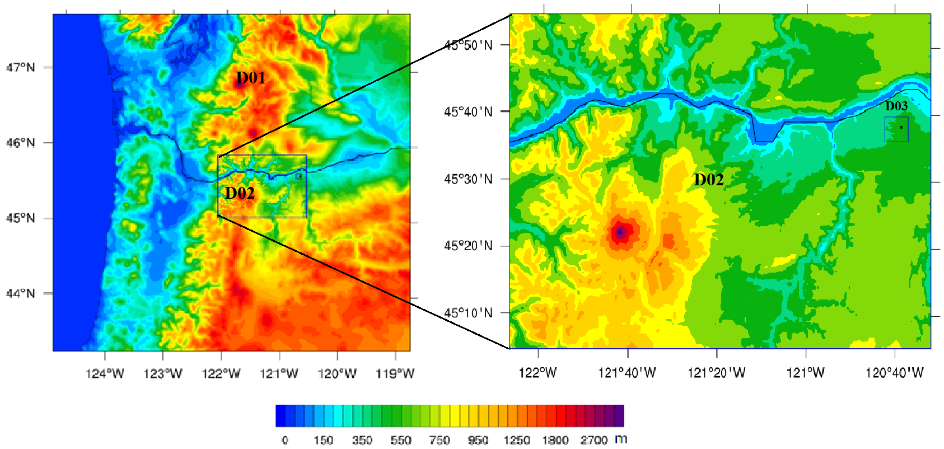

Figure 3.33. WRF nested domain setup for MMC simulations at the WFIP 2 site.

Table 3.2. WRF domain setup for the 11 November 2016 simulations at the WFIP 2 site.

D01			D02			D03			*nz*
nx	*Ny*	Δx [m]	*nx*	*ny*	Δx [m]	*nx*	*ny*	Δx [m]	
389	389	1287	865	649	143	529	529	13	180

Figure 3.34 and Figure 3.35 show instantaneous contours of horizontal wind speed V_h from 17:00 and 1800 UTC (9:00 and 10:00 am Local Standard Time) at 100 m above the surface. Here the left panel is again from the coarsest LES domain, while the panels at right show the fine LES (d03) both with (top) and without (bottom) the SCPM. Here, the SCPM was not used on d02. Due to small values of z_i occurring at 1700 UTC, and the SCPM being formulated to only apply perturbations of up to 0.667z_i, application of the SCPM does not result in turbulence penetrating to a height of 100 m, resulting in a nearly laminar flow. However, as z_i grows over the following hour, the effects of the perturbations on the developing flow field at 100 m are observed, resulting in more rapid development of turbulence than the simulation without the SCPM.

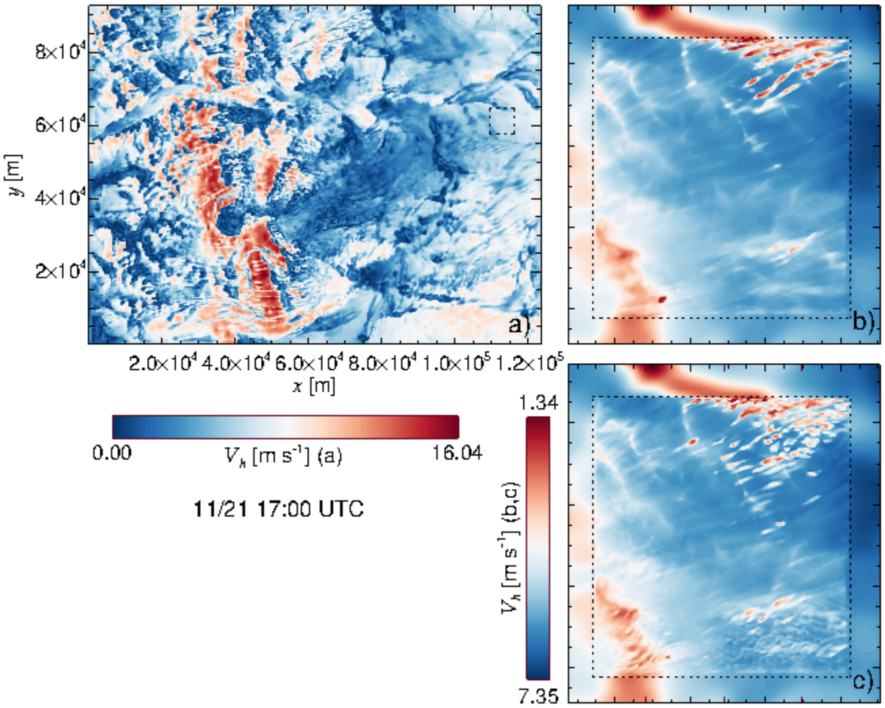

Figure 3.34. Instantaneous contours of wind speed at 100 m above the surface at 11/21 1700 UTC at the WFIP 2 site, in the coarse LES domain d02 (a), and the fine LES domain d03 both without (b) and with (c) the SCPM.

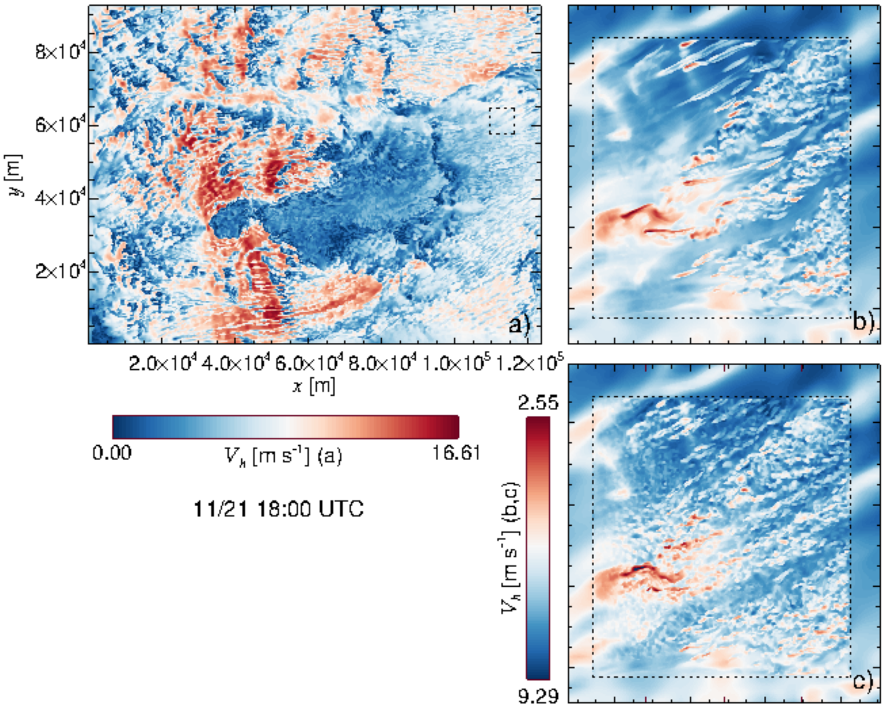

Figure 3.35. As in Figure 3.34, but 1 h later.

The use of $0.667z_i$ as the SCPM height was determined from idealized neutral setups with a strong capping inversion, in which the perturbations grew rapidly to the height of the inversion. However, in the more stable lower atmosphere at the WFIP 2 site during the case study, the turbulence does not penetrate upward to z_i, leaving the upper third of the PBL laminar. This observation suggests that during stable conditions, the height over which the SCPM is applied should be a larger fraction of the PBL height. Such examination is planned for FY18.

3.4.4 Conclusions

Use of the SCPM method in real-data case studies showed the effectiveness of the technique in accelerating turbulence formation in LES domains nested within mesoscale simulations during near neutral and stable conditions. A more rigorous assessment and comparison against measurements from the SWiFT and WFIP 2 field sites is planned for FY18. In particular, increasing the height to which the SCPM is applied during stable conditions will be evaluated. Further, using cells with uniform stochastic perturbations over several vertical levels, rather than using a unique value at each vertical level, will also be examined to further accelerate the method. Finally, we will examine a combination of temperature and velocity perturbations, the latter of which is discussed in the following section.

3.5 Comparison of Force Perturbations to Temperature Perturbations

In mesoscale-to-LES grid-nesting cases, the nested domain inflow from the parent domain often does not contain turbulent motions. Therefore, the highly resolved, nested domains must be large enough to allow for the small-scale turbulent motions to develop. Long turbulence-generation fetches can pose high computational cost requirements in MMC situations. To reduce computational expenses, turbulence-generation methods have been developed to allow for more rapid turbulence generation within nested domains. These methods work by introducing perturbations to the flow near the nested domain inflow boundaries. The perturbations can be random, or they can be generated from precursor simulations, which are representative of the expected turbulence. In this study, we implemented a new random perturbation method in the WRF model (Skamarock et al. 2008), which uses random forces near the inflow boundaries of the nested domain to trigger small-scale motions and thus accelerate turbulence development. This new method is tested in the context of a neutral PBL and is shown to improve turbulence generation in this context.

The new force-perturbation method is compared with the cell-perturbation method (Muñoz-Esparza et al. 2015), which applies potential temperature perturbations at the inflow boundaries of the nested domain. The motions caused by the potential temperature perturbations have been found to aid in the generation of turbulence for the nested domains, but a significant fetch is still required for temperature gradients to develop into small-scale turbulent flow structures. The force-perturbation method uses random forces to directly accelerate/decelerate the flow near the inflow boundaries. The net acceleration/deceleration of the perturbed flow is zero, ensuring that the perturbations have no effect on the mean characteristics of the incoming flow. The structure of the perturbations matches the optimal structure recommended by Muñoz-Esparza et al. (2015): each perturbation is applied over a rectangular cell of size $[L_x,L_y,L_z] = [8,8,1]$ grid points. Three rows of cells perturb the inflow boundaries of the nested domains (Figure 3.36).

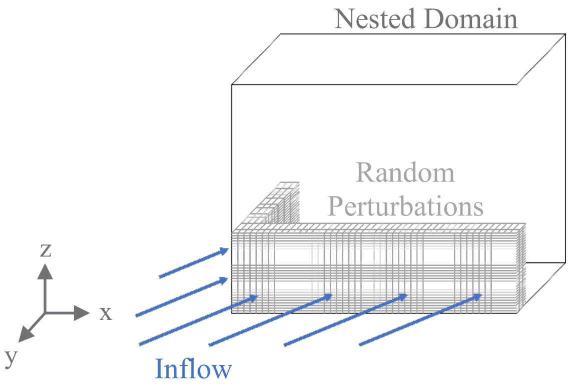

Figure 3.36. Diagram showing the implementation of temperature and force perturbations in a rectangular, nested domain with an incoming mesoscale inflow (not to scale).

Each perturbation was selected from a uniform random distribution with a predetermined maximum possible value. The entire perturbed field was refreshed with a temporal frequency of ~1 minute, as determined by Muñoz-Esparza et al. (2015). The forcing is applied at every modeled time step through WRF's tendencies [kg s^{-4}].

A nested mesoscale-to-microscale configuration was used for this study. The mesoscale, periodic parent domain has a grid-cell size of $\Delta_x = \Delta_y = 90$ m, and is forced by a geostrophic wind of $[u_g, v_g, w_g] = [10,0,0]$ m s^{-1}. The nested LES domains are centered within the mesoscale parent domain. Both parent and nested domain dimensions are shown in Figure 3.37. The turbulence closure schemes used are the MYNN (Nakanishi and Niino 2009) for the parent mesoscale PBL scheme, and the NBA model (Kosović 1997; Mirocha et al. 2010) for the nested LES turbulence closure scheme.

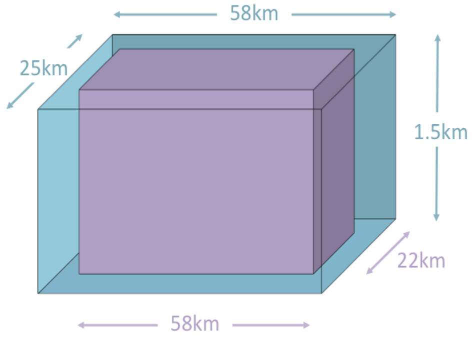

Figure 3.37. Dimensions of the simulated parent mesoscale and nested LES domains (not to scale).

Different maximum amplitudes were tested in a neutral PBL to determine the optimal strength of both vertical and horizontal force perturbations (Table 3.3). The force-perturbed simulations were compared to a reference standalone, periodic LES simulation. Additionally, the performance of this new perturbation method was compared to that of the potential temperature perturbations ($\theta_{0.33}$).

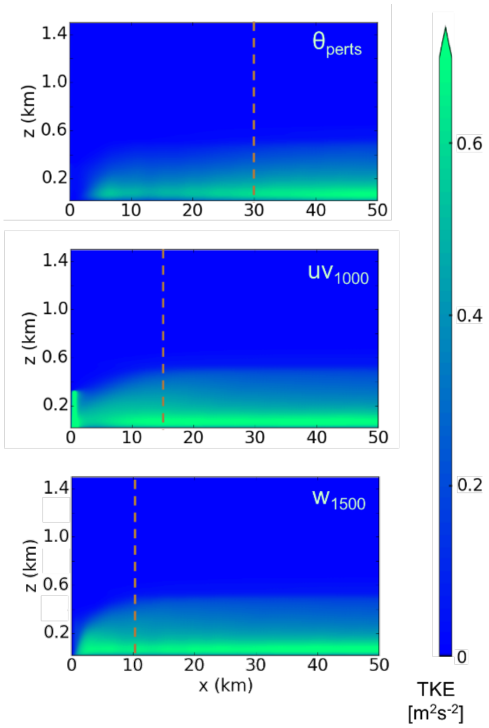

Figure 3.38. y- and t-averaged evolution of TKE in the x-direction for the three perturbed simulations.

Table 3.3. Reference standalone and nested simulations.

Perturbed Variable	Label	Amplitude
NA	ref	NA
θ	$\theta_{0.33}$	0.33 K
u,v	uv_{500}	500 kg s^{-4}
	uv_{750}	750 kg s^{-4}
	uv_{1000}	1000 kg s^{-4}
	uv_{2500}	2500 kg s^{-4}
	uv_{5000}	5000 kg s^{-4}
w	w_{1000}	1000 kg s^{-4}
	w_{1500}	1500 kg s^{-4}
	w_{2000}	2000 kg s^{-4}
	w_{2500}	2500 kg s^{-4}

Each force-perturbation amplitude was at first roughly evaluated by comparing the x-evolution of resolved TKE between the perturbed and the reference simulations (Figure 3.38). The values of TKE presented have been averaged over 4 h of simulation. From this analysis, u_{1000} and w_{1500} were chosen as optimal configurations of the force perturbations for the current case, and were used for further comparisons.

The x-evolution of TKE was analyzed for all heights in the boundary layer (Figure 3.39). The fetch of turbulence generation was defined as the x-location where TKE varies by less than ±5% for all heights within the boundary layer (Figure 3.39). This fetch was found to be ~15 km for the horizontal force perturbations, ~10 km for the vertical force perturbations, and ~30 km for the potential temperature perturbation method, representing a fetch reduction of ~50–66 % when using the new method.

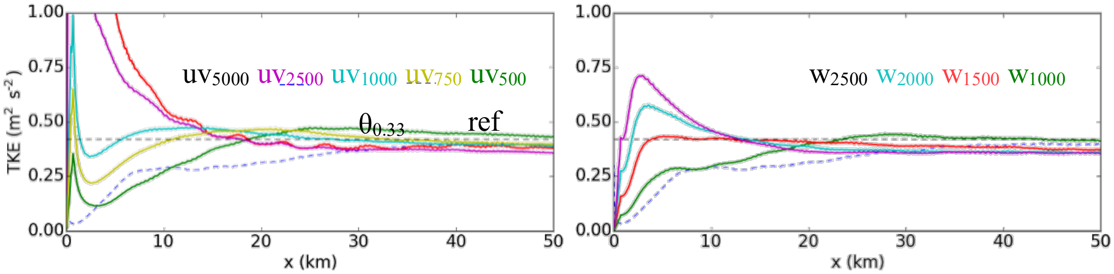

Figure 3.39. y- and t-averaged, resolved TKE at z = 250 m for all of the nested simulations, compared to the standalone, periodic reference LES.

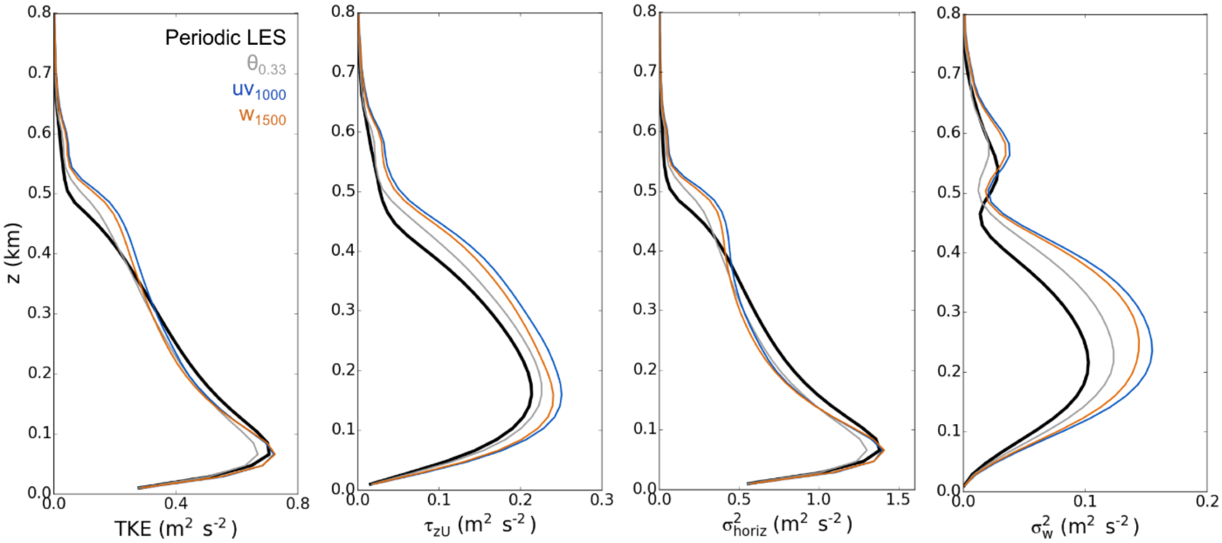

Figure 3.40. y- and t-averaged vertical profiles of resolved TKE, Reynolds Stress (τ_{zu}), horizontal variance (σ_{horiz}^2), and vertical variance (σ^2) at x = 40 km.

The developed turbulence characteristics of the perturbation methods and the reference simulation were also compared. Vertical profiles of resolved turbulent statistics were computed at a distance $x = 40$ km from the inflow boundary. Vertical profiles of resolved TKE, Reynolds stress (τ_{zU}), and vertical and horizontal variances (σ^2_{horiz} and σ^2_w) (Figure 3.40) show good general agreement between the perturbed and the standalone simulations. In the lowest 100 m of the PBL, TKE is closest to the reference simulations for the case of force perturbations, uv_{1000} and w_{1500}, while $\theta_{0.33}$ shows a slightly underestimated TKE in this region. This underestimation is caused by a low σ^2_{horiz} in this region for $\theta_{0.33}$.

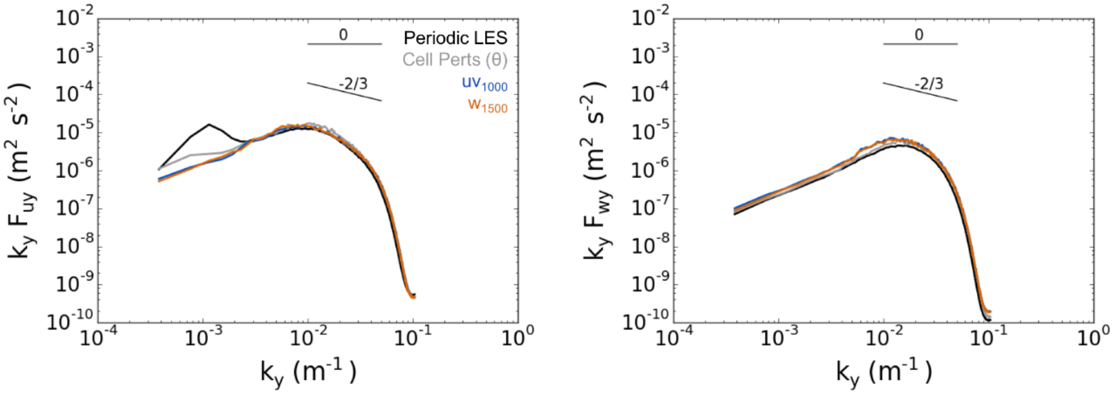

Figure 3.41. y- and t-averaged turbulent spectra of horizontal (KyFuy) and vertical (KyFwy) velocity at x = 40 km.

The more direct effect of the force perturbations on the flow has been shown to shorten the fetch of nested LES turbulence generation in the case of a neutral atmospheric boundary layer. Using the structure of boundary perturbations presented in this study, vertical force perturbations perform better than horizontal force perturbations. Additionally, both force-perturbation setups have a lower fetch than the θ-perturbed simulations by ~55–60%. This significant improvement results in a decrease in the required domain size for a highly resolved, nested domain, and thus reduced computational costs. Further analysis is under way to assess the performance of the force-perturbation method in the context of convective and stable boundary layers.

4.0 Improved Surface-Layer Approaches for LES

Atmospheric LESs require specification of surface boundary conditions for momentum, heat (if buoyancy effects are to be considered), and any scalars exchanged between the surface and the atmosphere. Typically, the Monin-Obukhov similarity theory (MOST; Monin and Obukhov 1954) is used to parameterize exchange coefficients that modulate the fluxes of quantities at the surface. A standard treatment for the fluxes of momentum and heat (with other scalars treated similarly) is

$$\tau_{i3}^{s} = -C_D V(z_1) u_i(z_1) \text{ and} \tag{4.1}$$

$$H_S = -C_H[\theta_S - \theta(z_1)], \tag{4.2}$$

where C_D and C_H are exchange coefficients for momentum and heat; V is the scalar wind speed; $\theta = T(p_0/p)^{R/c_p}$ is the potential temperature, with T the temperature, p the pressure, $p_0 = 1 \times 10^5$ Pa is a reference value, R is the gas constant for dry air, and c_p is the specific heat of dry air at constant pressure; θ_S is the surface value of the potential temperature; and z_1 the lowest height above the surface at which velocity and potential temperature are computed.

Exchange coefficients

$$C_\alpha = \kappa^2 \left[\ln\left(\frac{z_1}{z_{0,\alpha}} - \psi_\alpha\left(\frac{z}{L}\right)\right)\right]^{-2} \tag{4.3}$$

in Equations (4.1) and (4.2) are determined using a roughness length $z_{0,\alpha}$ and stability function $\psi_\alpha\left(\frac{z}{L}\right)$ for quantity α. Here $L = [\,-u_*^3\theta_{v0}]/[\kappa g H_S]$ is the Obukhov length, with

$$u_* = [(\tau_{13})^2 + (\tau_{23})^2]^{1/4}, \tag{4.4}$$

with τ_{13} and τ_{23} computed at the surface, $\theta_{v0} = 300$ K a reference value of the virtual potential temperature, and $\theta_v = \theta(1 + 0.61q_v)$, where q_v is the water vapor mixing ratio, $\kappa = 0.4$ is the von Kármán constant, and g is the gravitational acceleration in the limit of neutral conditions, for which $L = \infty$, $\psi\left(\frac{z}{L}\right) = 0$. Due to the interdependence of C_α, u_*, and H_S, their values must be determined iteratively (Moeng 1984).

Although MOST is commonly used for atmospheric flows in many applications and scales, its applicability is restricted to homogeneous surface cover under steady flow conditions, for which it provides an ensemble average relationship between surface exchange and the flow speed near the surface. Hence, the applicability of MOST locally to the instantaneous fluctuating velocity values resolved in LES is tenuous, even in homogeneous and steady applications, and increasingly so in more complex settings. In addition, for large roughness values, such as those representing tall vegetation canopies with heights greater than the vertical grid spacing of the simulation (hence permitting explicit resolution of the vertical distribution of canopy elements), the standard MOST implementation cannot recover observed profile characteristics or mean bulk drag within the lower PBL.

Canopies may be crudely accounted for in the traditional MOST framework using a displacement distance d that shifts the log layer to the top of the canopy. However, when the vertical resolution is high enough to resolve the canopy structure and flow within it, up to the roughness sublayer (up to $z/h_c = 2$ or 3, where h_c is the canopy height), the resolved canopy model provides superior results. Such resolved canopy models (see review by Patton and Finnigan 2012) achieve superior performance through the addition of a drag force, distributed over depth h_c, to the momentum equations (e.g., Shaw and Schumann 1992; Patton et al. 2001). Further improvements can be obtained from simulations using SGS turbulence parameterizations based upon SGS TKE, for which additional terms can be added to account for canopy effects on SGS dissipation (e.g., Shaw and Patton 2003).

Although resolved canopy models were originally designed for specific surface features such as forest canopies, modified versions have been employed to improve the agreement of LES velocity profiles with log-law theory near the surface. Brown et al. (2001) originally implemented such a model in their study of turbulent flow over ridges. More recently, Chow et al. (2005) and Kirkil et al. (2012) have used a similar modified canopy model to augment the SGS stresses calculated by dynamic LES closure schemes, which produce too little resolved stress near the surface in finite-difference numerical schemes.

Herein, canopy models implemented into LES are investigated to provide improved near-surface flow characteristics of relevance to wind-energy research and operational needs.

4.1 Explicit and Pseudo-Canopy Models Implemented in WRF

Two canopy model frameworks were implemented into the WRF model (Skamarock et al. 2008) and investigated in LES, with a view toward improving lower PBL velocity characteristics of relevance to wind-energy applications, including wind speed, TKE, and stresses. First, the resolved canopy model of Shaw and Patton (2003) was implemented for resolved canopy applications, and validated against an idealized test case over a forested canopy corresponding to a surface roughness length of $z_0 = 1.0$ m. Additionally, a “pseudo-canopy” approach, based on a modified form of the resolved canopy framework, was developed to improve the representation of PBL velocity characteristics over surfaces characterized by smaller roughness lengths of $z_0 = 0.1$ and $z_0 = 0.01$. This approach, for which coefficients of drag are prescribed as decreasing functions of height within a shallow layer above the surface, was shown to improve agreement of simulated wind speed profiles with the expected logarithmic similarity solution, while also increasing the magnitudes of resolved TKE and model stresses.

4.1.1 A Resolved Canopy Model for Large Surface Roughnesses

Following Shaw and Patten (2003), a drag force F_i representing effects of the resolved canopy on the flow is incorporated into the WRF model’s momentum equations, as

$$F_i = -\mu\left(C_d + C_{sf}\right)a u_i V, \tag{4.5}$$

where $i = 1,2,3$ are the zonal, meridional, and vertical directions; μ is the dry air mass in each vertical column at each model grid point; C_d is the form drag coefficient; C_{sf} is the skin friction drag coefficient; a is the area density of drag elements; u_i is the resolved velocity; and $V = \left(u_i^2\right)^{1/2}$ is the magnitude of the resolved velocity. The skin friction drag coefficient is defined as $C_{sf} = 1.328/Re$, where $Re = V l_c \nu$ is a Reynolds number based on the canopy element length scale l_c, and ν is the kinematic viscosity of air.

In addition to the explicit drag terms represented by Equation (4.5), SP03 also includes modifications to the traditional 1.5-order SGS TKE model of Deardorff (1970), which parameterizes the SGS stresses as

$$m_{ij} = -2K_M\tilde{S}_{ij}, \text{ where} \tag{4.6}$$

$$K_M = C_e l (e_{SGS})^{1/2}.$$

where $\tilde{S}_{ij} = \frac{1}{2}\left(\frac{\partial \tilde{u}_i}{\partial x_j} + \frac{\partial \tilde{u}_j}{\partial x_i}\right)$ is the resolved strain-rate tensor with $\tilde{a}$ denoting a resolved component of variable a, $C_e = 0.1$ is a constant, $l_\Delta = (\Delta x \Delta y \Delta z)^{1/3}$ is the length scale (as parameterized in WRF using the mix_isotropic option), and e_{SGS} is the SGS TKE.

Shaw and Patton (2003) partitions e_{SGS} into two components—the traditional grid scale, as in Deardorff (1970), corresponding to the scale of the grid spacing l_Δ, and the wake scale, e_W, corresponding to the scale of the canopy elements l_c, yielding

$$K_m = c_e\left(l_\Delta (e_{SGS})^{1/2} + l_c (e_w)^{1/2}\right).$$

The evolutions of e_{SGS} and e_W in SP03 are given by

$$\frac{\partial(\mu e_{SGS})}{\partial t} = -A_{SGS} + \mu\left(P_{SGS} + B + D_{SGS} - T - \epsilon - \epsilon_{sf}\right) \text{ and} \tag{4.7}$$

$$\frac{\partial(\mu e_W)}{\partial t} = -A_W + \mu(P_W + D_W + T - \epsilon_W) \tag{4.8}$$

where $A, P, B, D,$ and ϵ represent advection, shear production, buoyancy production, subgrid turbulent diffusion, and dissipation, as in Deardorff (1970). Terms in Equation (4.8) arising from the canopy model are T, which represents the transfer of TKE from the subgrid to the wake scale, and new dissipation terms ϵ_{sf}, which represents augmented dissipation of e_{SGS} via viscous dissipation on canopy surfaces, such as branches and leaves, as well as a parameterized wake-scale dissipation, ϵ_W. Thus, implementation of SP03 into WRF involved adding Equation (4.5) to WRF's momentum equations, terms T and ϵ_{sf} to WRF's native e_{SGS} Equation (4.7), and Equation (4.8).

4.1.1.1 Validation of the Implementation into WRF

The implementation of SP03 into the WRF model was validated through comparison to the idealized test case conducted in Shaw and Patton (2003), which consists of a flat and horizontally homogeneous domain using periodic lateral boundary conditions. Their validation used very fine grid spacing of $\Delta x = \Delta y = \Delta z = 2$ m, using $(nx, ny, nz) = (192{,}192{,}60)$ grid points, yielding a domain size of $(Lx, Ly, Lz) = (384{,}384{,}120)$ m forced by a uniform driving force such that V at h_c was 1 m s^{-1}. To examine the applicability to wind energy, we instead forced the simulation with a larger geostrophic wind of $V_g = (u_g, v_g) = (10.0)$ m s^{-1}, with a coarser grid spacing over a larger domain. We used $\Delta x = \Delta y = 8$ m, with $(nx, ny) = (128{,}128)$ grid points, yielding a domain of size $(Lx, Ly) = 1024$ m. The vertical grid spacing used $\Delta z = 4$ m from the surface up to $z = h_c = 20$ m, above which it was stretched by a factor of 1.025 up to $z = 175$ m, above which $\Delta z = 8$ m. Figure 4.1 shows the (horizontally uniform) area density profile $a(z)$ used in both validation simulations. Each simulation used a canopy element length scale of $l_c = 0.1$.

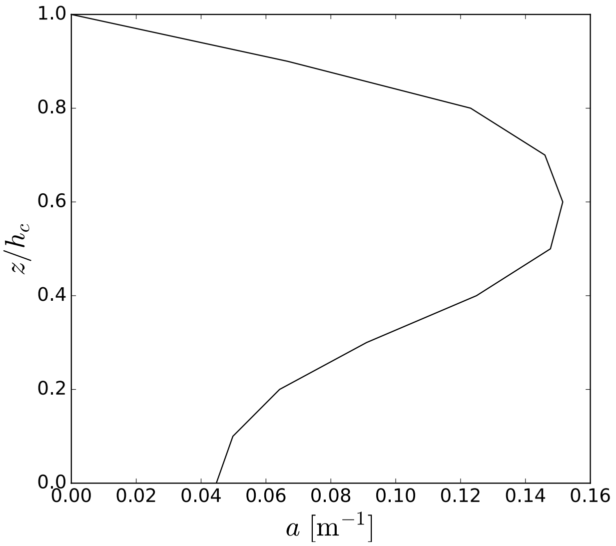

Figure 4.1. The area density $\boldsymbol{a(z)}$ profile used herein and in Shaw and Patton (2003) (taken from Dwyer 1997). The profile integrates to give a leaf area index of 2.

We used a neutral potential temperature profile up to $z = 1$ km, above which an inversion layer with $\partial\theta/\partial z = 0.003$ K m^{-1} was added to limit the vertical extent of the PBL. A Rayleigh damping layer was used for $z > 1$ km to dampen waves. Simulations were run for 18 h with data output every 30 s. In the analysis that follows, all quantities were both planar averaged (denoted by an overbar) and time-averaged over the last hour of the simulation (between hours 1700–1800, denoted by $\langle\cdot\rangle$).

Figure 4.2a shows the profile of horizontal velocity magnitude $\langle\bar{V}_h\rangle$, indicating that the canopy drag restricts the flow below $z < h_c$, resulting in a velocity profile that has an inflection point near the canopy top. Figure 4.2b shows profiles of the total TKE and its components. The resolved component is computed as $e_R = \langle\overline{\acute{u}_\iota\acute{u}_\iota}\rangle/2$, where the primes denote departures from planar-average values. The two SGS components, traditional SGS $\langle\overline{e_{SGS}}\rangle$ and wake scale $\langle\overline{e_W}\rangle$, are computed from Equations ((4.7–(4.8) during code execution. The total is then calculated as $e_T = e_R + e_{SGS} + e_W$. The friction velocity u_* is calculated at the canopy height h_c from Equation (4.4) using $\tau_{ij} = \langle\overline{\acute{u}_\iota\acute{u}_\iota} + m_{ij}\rangle$, with m_{ij} the SGS stress calculated from Equation (4.6).

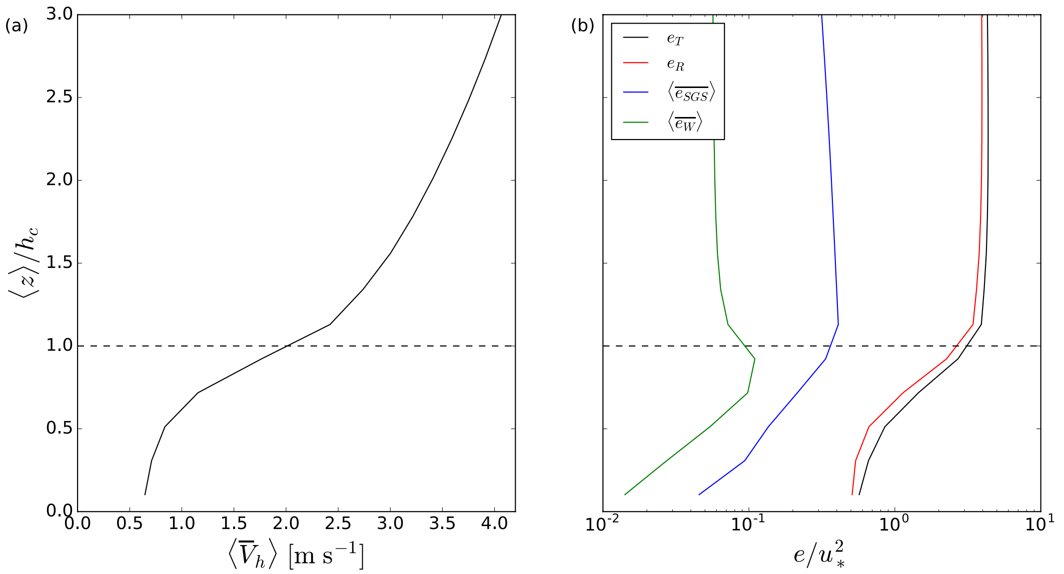

Figure 4.2. The averaged (a) horizontal velocity $\langle \overline{\boldsymbol{V}}_{\boldsymbol{h}} \rangle$ and (b) TKE component profiles for the WRF validation. The friction velocity $\boldsymbol{u}_*$ was calculated at the canopy height $\boldsymbol{h_c}$.

Figure 4.2 shows that canopy-induced drag and shear lead to significant departures of wind speed and TKE relative to the standard logarithmic distribution provided by MOST. Even at the relatively coarse resolutions conducted herein, roughly $85 - 95$ % of TKE production of is resolved. The SGS TKE profile has nearly the same shape as the resolved TKE profile, although it is roughly an order of magnitude smaller. The shape of the wake-scale TKE profile more closely follows that of the area density a, and is slightly smaller than the SGS TKE.

Vertical profiles of the TKE budget terms from Equations ((4.7–(4.8) are presented in Figure 4.3, which shows that resolved shear leads to the production of SGS TKE that is predominantly either dissipated or transferred to the wake scale. The free-air dissipation and transfer terms are nearly equal in magnitude within the canopy, while dissipation is much larger above the canopy. Wake-scale TKE is produced where large velocities overlap with large a values inside the canopy and is primarily dissipated locally. The transfer of SGS TKE to the wake scale is relatively small compared to wake production; thus, the transfer term serves primarily as a sink of SGS TKE.

Overall, the WRF TKE and TKE budget results agree in terms of shape and magnitude with the results of Shaw and Patton (2003) (see Figures 3, 4, and 5 therein). Minor disagreements are likely due to differences in the numerical methods, computational setup, and grid spacing; Shaw and Patton (2003) uses a pseudospectral code in a relatively smaller, more highly resolved domain, and is forced with no Coriolis effect.

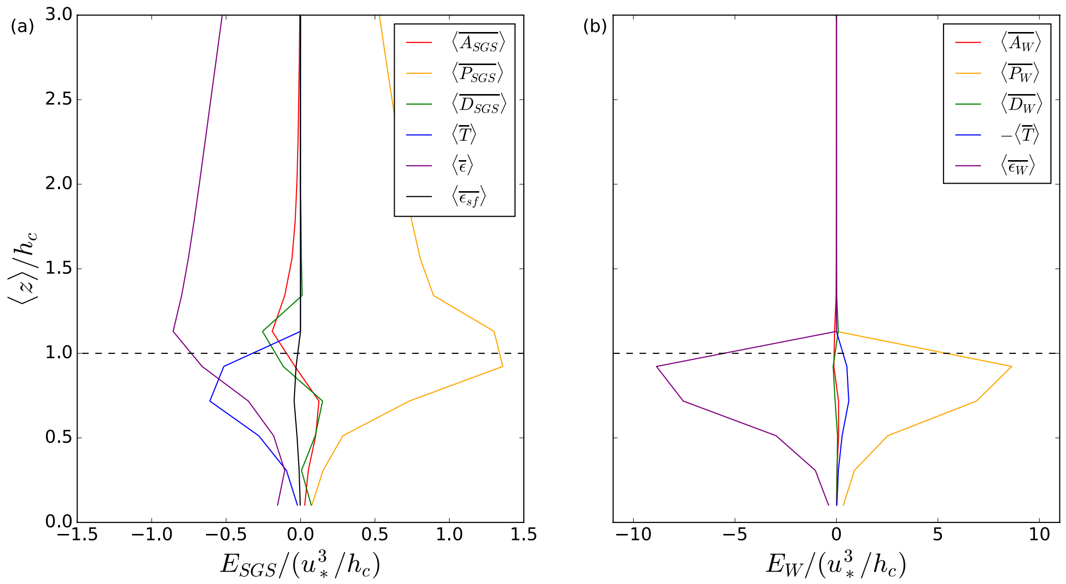

Figure 4.3. The averaged (a) SGS TKE budget terms $\boldsymbol{E_{SGS}}$ from Equation (4.7) and (b) wake-scale TKE budget terms $\boldsymbol{E_W}$ from Equation (4.8) from the WRF validation case. The friction velocity $\boldsymbol{u_*}$ was calculated at the canopy height $\boldsymbol{h_c}$.

4.1.2 A Pseudo-Canopy Model for Small Surface Roughnesses

Although the resolved canopy model described above was designed to represent a forest canopy, a modified approach was formulated to better recover the law-of-the-wall behavior that is typically not well satisfied in LES (e.g., Brasseur and Wei 2010). In this section, the canopy model framework is extended for this purpose, and is denoted as the “pseudo-canopy" model (PCM).

The PCM is a two-part model, combining both standard MOST implementation and elements of the canopy parameterization described above. In the PCM approach, most of the drag is expressed through a drag force function similar to that defined in Equation (4.5),

$$F_i = -\mu C_d a u_i V. \tag{4.9}$$

An additional small background stress is still applied through the standard MOST implementation, Equation (4.3) using a background roughness length of $z_0^{bg} = 0.0001$.

C_d in Equation (4.9) is determined by first specifying a desired “effective” value of the surface roughness length, z_0^{eff}, which, via Equation (4.3), yields an effective drag coefficient,

$$C_d^{eff} = \left(\frac{\kappa}{\ln\left(z_1/z_0^{eff}\right)}\right)^2 - \left(\frac{\kappa}{\ln\left(z_1/z_0^{bg}\right)}\right)^2.$$

Here, $\psi_\alpha\left(\frac{z}{L}\right) = 0$ due to neutral stability, z_1 is the height of the first grid point above the surface, and the second term on the righthand side indicates removal of the drag already accounted for by application of the background MOST parameterization.

We seek to apply this effective drag C_d^{eff} over a layer of depth h_c, as the product of a drag coefficient C_d, and a canopy shape function a,

$$C_d^{eff} = C_d \int_0^{hc} a\, dz.$$

The value of C_d used in Equation (4.9) is therefore obtained as

$$C_d = \frac{C_d^{eff}}{\sum_{k=1}^{k=k_c} a_k \Delta z_k},$$

where the sum in the denominator accounts for the finite representation of the shape function on the model vertical grid. This formulation guarantees that the effective integrated drag depends only on z_0, but allows the actual drag to be distributed over h_c.

Because the objective is to improve flow over roughness lengths representative of surface cover beneath the vertical resolution of the model, $a(z)$ is chosen such that the drag is maximal near the surface. Four different shape functions for the decrease of $a(z)$ with height are implemented;

$$a(z) = \exp(-r_a z) \tag{4.10}$$

$$a(z) = \exp(-r_a z/2)^{1/2} - \exp\,(-r_a h_c/2)^{1/2} \tag{4.11}$$

$$a(z) = \exp(-r_a z)^2 \tag{4.12}$$

$$a(z) = \cos^2(\pi z/2h_c), \tag{4.13}$$

where the exponential decay rate is $r_a = \ln(1 \times 10^{-3})\,/h_c$. Figure 4.4 shows each shape function for various values of h_c, using $z_0^{eff} = 0.1$. The area under the curve, or the effective drag, C_d^{eff}, is the same for each case. The curves in Figure 4.4 would look qualitatively similar for other z_0^{eff} values, although their magnitudes would be different.

4.1.2.1 Validation of the Pseudo-Canopy Model

The effectiveness of the pseudo-canopy implementation is tested in neutral stability conditions using the same numerical setup as that in Section 4.2.1. First, three baseline WRF cases were run for $z_0 = 0.01$, 0.1, and 1.0 using a standard MOST implementation and WRF's standard TKE 1.5 LES scheme.

A suite of PCM simulations was run with $z_0^{eff} = 0.01$, 0.1, and 1.0, four shape functions (defined in Equations (4.10–(4.13), and heights ranging from $h_c = 8$ to $h_c = 56$. The PCM runs were restarted from hour 12 of the corresponding baseline WRF simulation, and run for an additional 6 h, to reduce computational overhead. The results are indistinguishable from those using the PCM from the beginning.

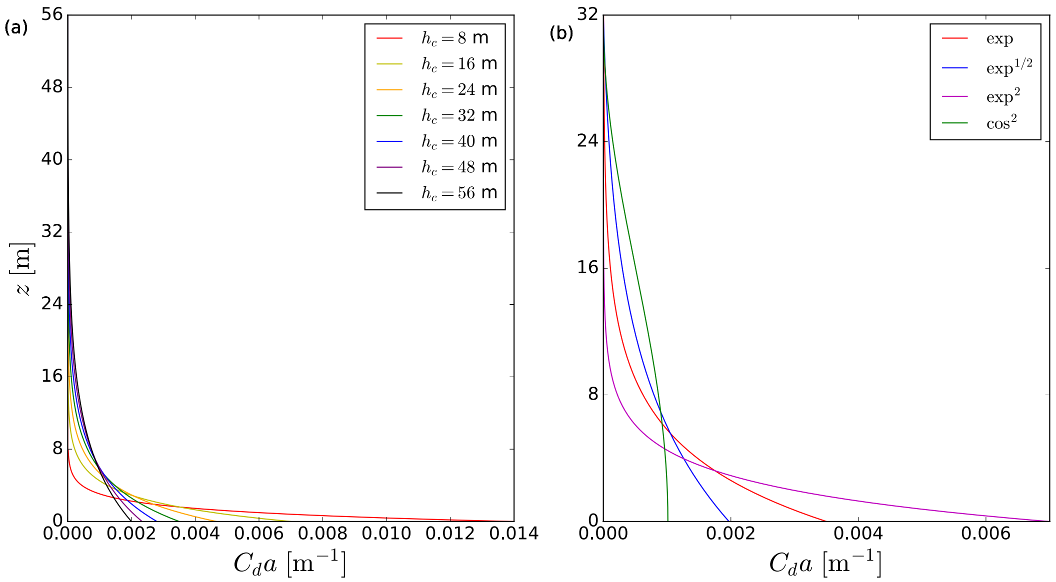

Figure 4.4. The magnitude of the drag term $\boldsymbol{C_d a}$, in Equation (4.9) for the PCM shape functions (a) $\boldsymbol{exp}$ (Equation (4.10)), (b) $\boldsymbol{exp^{1/2}}$ (Equation (4.11)), (c) $\boldsymbol{exp^2}$ (Equation (4.12)), and (d) $\boldsymbol{cos^2}$ (Equation (4.13)) with a range of canopy heights. The effective surface roughness is $\boldsymbol{z_0^{eff} = 0.1}$.

The performance of the PCM was first assessed by comparing the resulting simulated velocity profile $\langle \overline{V_h} \rangle$ against an appropriate "expected" profile, V_{ex}. Figure 4.5 shows simulated $\langle \overline{V_h} \rangle$ profiles relative to their corresponding V_{ex} profiles for three different values of $z_0^{eff} = 0.01, 0.1,$ and 1 m. The left panels show $\langle \overline{V_h} \rangle$ versus z, while those at the right show $\langle \overline{V_h} \rangle$ scaled by $\langle \overline{u_*} \rangle$, permitting comparison to the standard MOST logarithmic profiles, which appear as straight (dashed) lines and are the expected profiles for the two smaller z_0^{eff} cases.

The solid black lines in Figure 4.5 show $\langle \overline{V_h} \rangle$ using the standard MOST implementation described in Section 4.2 for each of the three z_0^{eff} values. The dashed black lines show $V_{ex} = \frac{u_*}{\kappa} ln\left(\frac{z}{z_0}\right)$, with $z_0 = z_0^{eff}$, and u_* equal to $\langle \overline{u_*} \rangle$ from the corresponding MOST simulation. In the calculation of u_* (using Equation (4.4)), the surface stress was computed using $\tau_{13} = -C_{d\tau} u_i(1) V_h(1)$ with, $C_{d\tau} = \left(\frac{\kappa}{ln(z(1)/z_0)}\right)$, where u_i, V_h, and z were taken at the first grid point above the surface.

The $\langle \overline{V_h} \rangle$ profiles (solid black lines) using the standard MOST implementation show significant departures from the corresponding V_{ex} profiles (dashed black lines) calculated from the same z_0 and u_*values. The solid colored lines show $\langle \overline{V_h} \rangle$ from simulations using each of the canopy shape functions, corresponding to the h_c value resulting in the closest agreement with its corresponding V_{ex} profile (dashed), obtained using the same corresponding z_0 and u_*values. Wind speeds using the PCM simulations show much closer agreement with their expected distributions than those using the standard MOST implementation.

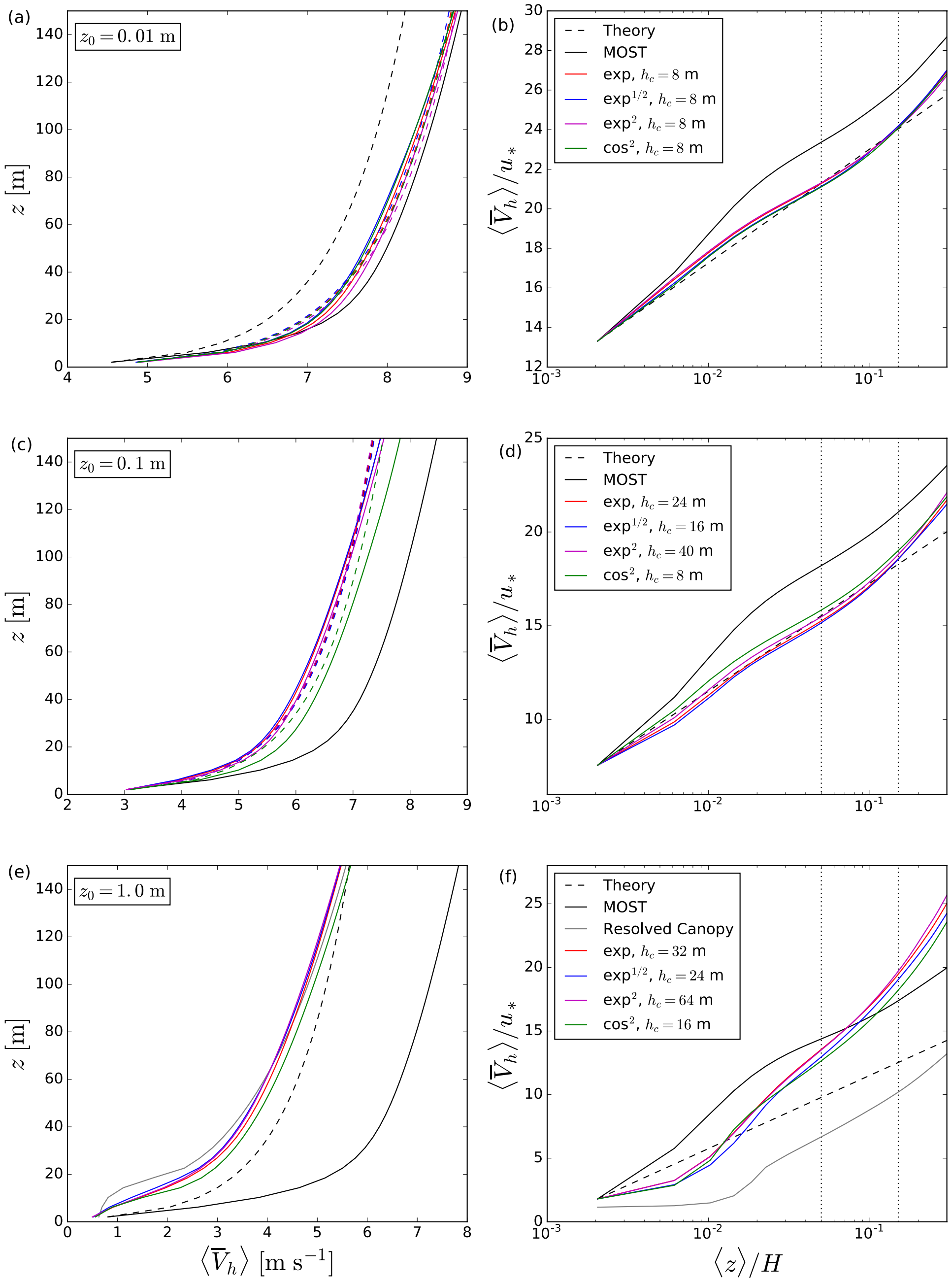

Figure 4.5. Averaged velocity profiles from WRF simulations (solid lines) compared to the corresponding expected profiles $\boldsymbol{V_{ex}}$ (dashed lines) for (a) $\boldsymbol{z_0 = 0.01}$, (b) $\boldsymbol{z_0 = 0.1}$, and (c) $\boldsymbol{z_0 = 1.0}$. Included in each plot are the pseudo-canopy cases with the optimal value of $\boldsymbol{h_c}$ for each shape function (see Figure 4.6), a standard MOST case, and the resolved canopy case for $\boldsymbol{z_0 = 1.0}$. Scaled profiles are shown in (c), (d), and (e), where the theoretical log-law profile is generated using the $\boldsymbol{u_*}$ value from the standard MOST case. For the resolved canopy case, $\boldsymbol{u_*}$ is calculated at the canopy height instead of at the surface.

For the $z_0^{eff} = 1$ m case, while the corresponding logarithmic profile is shown, the expected profile V_{ex} for this case is not logarithmic, due to use of vertical resolution sufficient to resolve the vertical structure of the canopy. Therefore V_{ex} for this case is taken as the simulation using the explicit canopy parameterization, as described in Section 4.2, and denoted as Resolved Canopy. Although none of the PCM simulations are expected to exactly match the resolved canopy case, due to different shapes of the $a(z)$ profiles, the PCM simulations nevertheless produce much better agreement than the standard MOST implementation.

Agreement with the expected profile for each case was evaluated quantitatively using the root mean square difference (RMSD) between an averaged WRF velocity profile, defined as

$$RMSD = \int_{z_a}^{z_b} \sqrt{[\langle \overline{V_h} \rangle (z) - V_{ex}(z)]^2}\, dz \,. \tag{4.14}$$

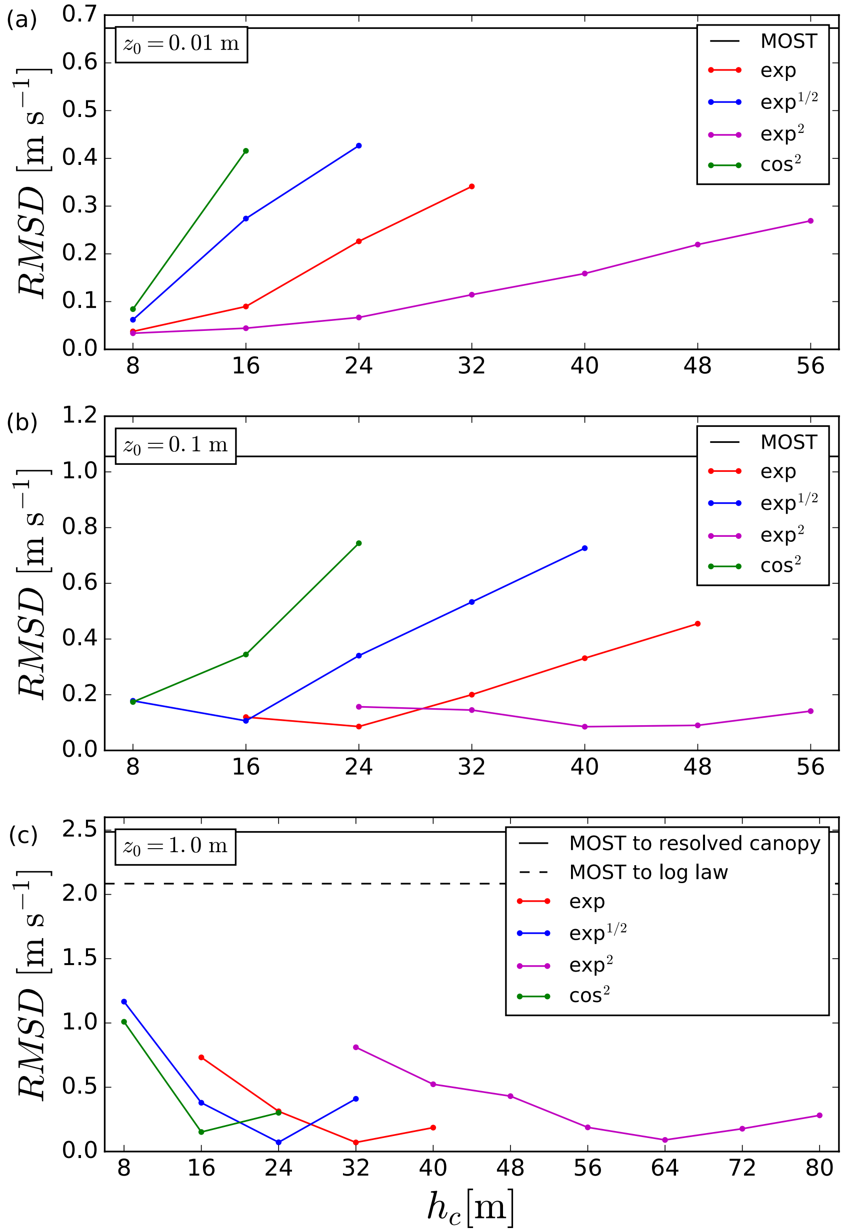

Figure 4.6. Root mean square differences (Equation (4.14)) between WRF velocity profiles and expected profiles (from either the log-law or the resolved canopy model) calculated for (a) $\boldsymbol{z_0 = 0.01}$, (b) $\boldsymbol{z_0 = 0.1}$, and (c) $\boldsymbol{z_0 = 1.0}$.

Here, $z_a = 50$ m and $z_b = 150$, corresponding to the rotor span of a modern utility-scale wind turbine. Figure 4.6 shows $RMSD$ values using both MOST implementations (black horizontal lines) and each of the PCM shape functions (colored) across a range of different h_c values. Although specific values of h_c perform slightly better than others, a range of values provides considerable improvement over the standard MOST values. The consistency in optimal h_c values for each shape function across test cases with $z_0^{eff} = 0.01$ and $z_0^{eff} = 0.1$ indicates the robustness of the PCM to capture near-surface logarithmic velocity profiles.

In addition to modifying the wind speed distributions within the PBL, the PCM also affects profiles of resolved TKE and u_*—important parameters to consider both for wind turbine operation and accumulated fatigue loading. Figure 4.7 indicates a significant increase in each of these two measures of resolved-scale variability within the flow relative to the standard MOST implementation (shown by the solid black lines). The shading in each panel indicates the range of profile mean values corresponding to each profile shape function, using each of the different h_c values from Figure 4.6. The solid colored line within each shaded region corresponds to the simulation achieving the lowest $RMSD$ value for $\langle \overline{V_h} \rangle$.

4.1.3 Conclusions

Implementation of two canopy parameterizations into the WRF model was shown to substantially improve flow over both a resolved forested canopy consisting of roughness elements larger than the vertical grid spacing of the simulation, as well as over flat, rough plates characterized by small roughness lengths. The new parameterizations provided improved wind speed distributions within the lower PBL, including an inflection point in the velocity profile near the canopy top of an explicitly resolved forest canopy, as well as improved agreement with the expected logarithmic similarity solution relative to the standard implementation of the MOST, over small roughness lengths. In addition to improving mean velocity profiles, the new parameterizations also significantly increased the magnitudes of the resolved TKE and friction velocity relative to the standard MOST implementation.

Although comparison of simulations with observations was not performed, comparison with both the expected similarity solutions and profiles from simulations using the explicit forested canopy parameterization indicated that the new PCM may be a simple and efficient way to improve the prediction of atmospheric flow characteristics of relevance to wind-plant operation over terrain characterized by smaller roughness lengths, such as agricultural, savannah, and desert landscapes. Comparison with field data from the SWiFT site, as described in the FY15 DOE-MMC report (Haupt et al. 2015), is the next step in further validating the improvements afforded by the PCM.

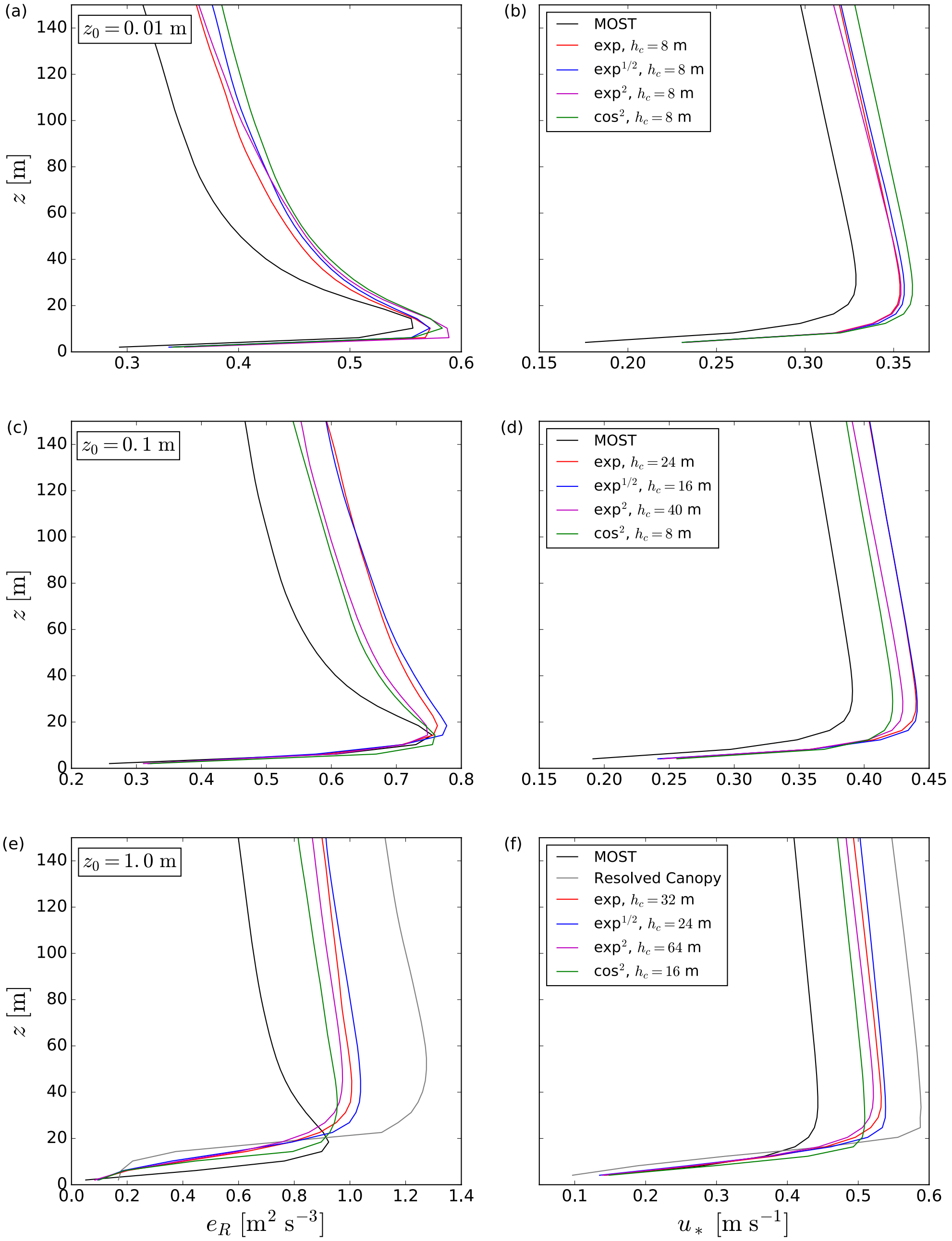

Figure 4.7. Resolved e_R and u_* profiles for (a,b) $z_0 = 0.01$, (c,d) $z_0 = 0.1$, and (e,f) $z_0 = 1.0$. Included in each plot are the pseudo-canopy cases with the optimal value of h_c for each shape function (as in Figure 4.6), a standard MOST case, and the resolved canopy case for $z_0 = 1.0$.

4.2 Impacts of Vegetation Heterogeneity on Atmospheric Turbulence

A boundary-layer flow is formed due to drag force (or friction) from a solid surface, viscosity of the fluid, and turbulent mixing in the flow. In PBL flows, vegetation is one of the sources of surface drag, contributing to the generation of turbulent mixing. In the context of wind-energy resources and the A2e program, turbulent characteristics of atmospheric flows at the height of wind turbine operation are of interest. In FY17, the impact of vegetation heterogeneity on the PBL flow characteristics was explored using LES. This preliminary study showed that the length scale of the heterogeneity has impacts on the turbulence characteristics on a similar length scale; however, further study of this topic is needed to acquire better understanding of how surface heterogeneity affects wind-energy production. This study will aid us in improving MMC, because it will allow us to determine the length scale of heterogeneity that must be resolved in microscale models to capture its impacts.

Although there are many ways to model vegetation drag at the surface, the MOST has been used prominently. However, this theory assumes homogeneous surface conditions, making it unsuitable for studies involving surface heterogeneity. An approach to modeling vegetation canopies as individual momentum sinks and TKE sources has been used in HIGRAD/FIRTEC (referred to as HIGRAD here) for modeling wind within the canopy in the context of wildfires (Pimont et al. 2009).

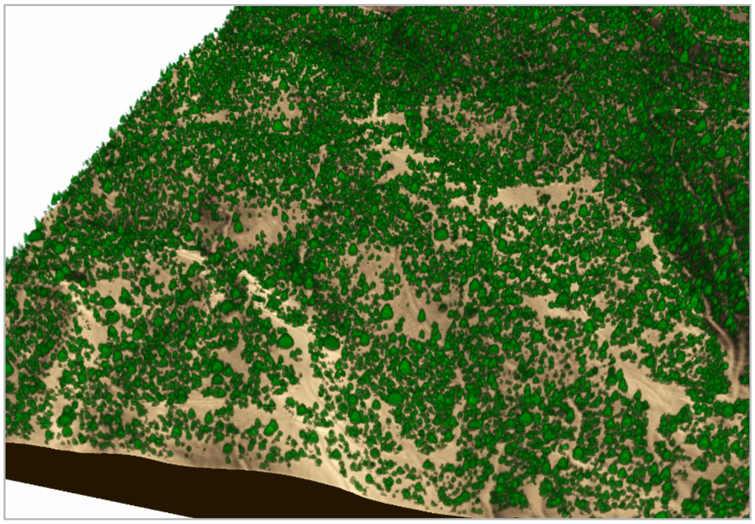

Figure 4.8. Visualization of canopy modeled in HIGRAD for ponderosa pine forest with 2-m resolution in real topography. Average tree height is 10 m. Solid (tree) density is used for visualization.

Typical canopy modeling in HIGRAD uses 2-m horizontal resolution and ~1.5-m vertical resolution near the surface to capture the shape of individual trees. HIGRAD typically uses vertical stretching with terrain-following vertical coordinates. Figure 4.8 shows a visualization of a ponderosa pine forest in real topography modeled when it is resolved in 2-m resolution. With ~1.5-m vertical resolution, a typical tree with average height of 10 m is resolved by 5 to 6 vertical grid points. However, such high resolutions could be computationally prohibitive for wind-plant simulations. To account for this limitation, a 5-m horizontal and vertical resolution was used in this study.

For this study, an idealized domain with periodic boundary conditions was used. The domain dimensions were 3 km × 1 km × 1 km. A neutral PBL was modeled, with a PBL thickness of 650 m and a geostrophic wind of 10 m s^{-1}. Three different vegetation types were modeled: homogeneous forest (PP_uni), forest with 40-m diameter disturbances with an average separation of 80 m (PP_40m), and forest with 80-m diameter disturbances with an average separation of 80 m (PP_80m). Trees were randomly populated based on measurements of a ponderosa pine forest near Flagstaff, Arizona (Linn et al. 2005). The maximum canopy height is 20 m, and the average height is 10 m. The circular-shaped disturbances are populated randomly based on their size and the distances between them. Figure 4.9 shows visualizations of the three different heterogeneous canopies. As shown in the close-up views in Figure 4.9, 5-m resolution is not sufficiently fine to resolve individual trees, but it is high enough to represent heterogeneity at the 40–80-m length scale.

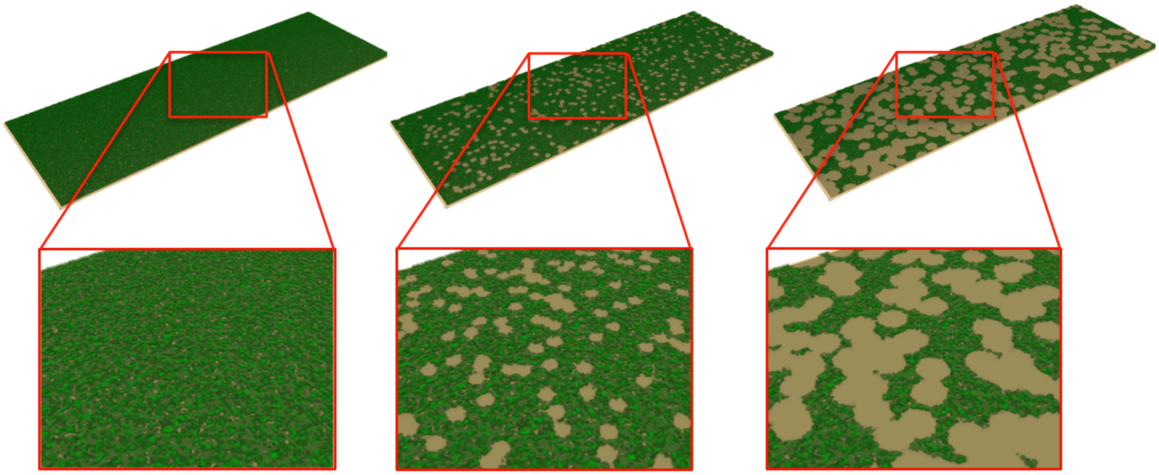

Figure 4.9. Visualization of three different types of vegetation heterogeneity for ponderosa pine forest: (left) homogeneous forest (PP_uni), (center) forest with 40-m diameter disturbances with 80-m separation (PP_40m), and (right) forest with 80m diameter disturbances with 80-m separation (PP_80m).

Figure 4.10 shows vertical profiles of average streamwise wind speed for the three types of vegetation heterogeneity. Wind speed within the canopy (<20 m) is heavily influenced by the canopy drag, which is reduced by the disturbances in the vegetation canopy. Above the canopy height (>20 m), the wind profile follows the log-profile as expected.

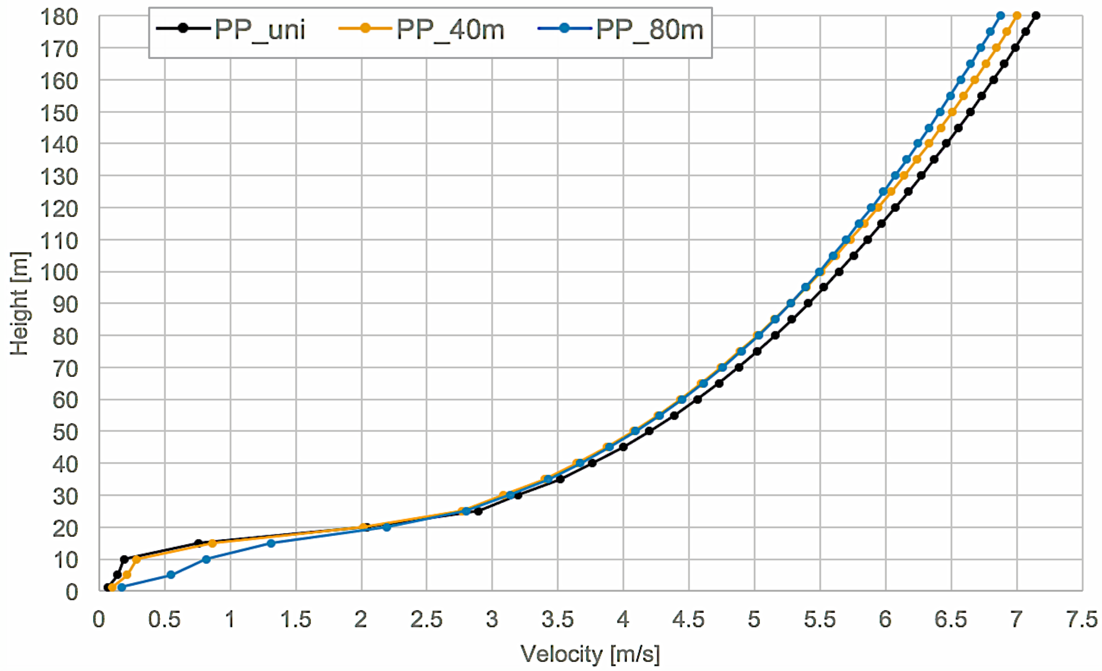

Figure 4.10. Vertical profiles of average streamwise wind speed for three different types of vegetation heterogeneity.

Figure 4.11 shows turbulent energy spectra at different heights, from 20 m to 180 m, for the three different types of heterogeneity. For the 80-m to 180-m heights, there is a notable peak at wavenumbers between 1.00e-2 m^{-1} and 2.00e-2 m^{-1} for the PP_80m case (blue in Figure 4.11). The length scale corresponding to these wavenumbers is close to 80 m, which is the length scale of the disturbances and the mean separation distance between them. In the case of the neutral PBL, we found that the energy at this length scale, generated by the heterogeneous vegetation canopy, propagated into 180-m height without significant dissipation.

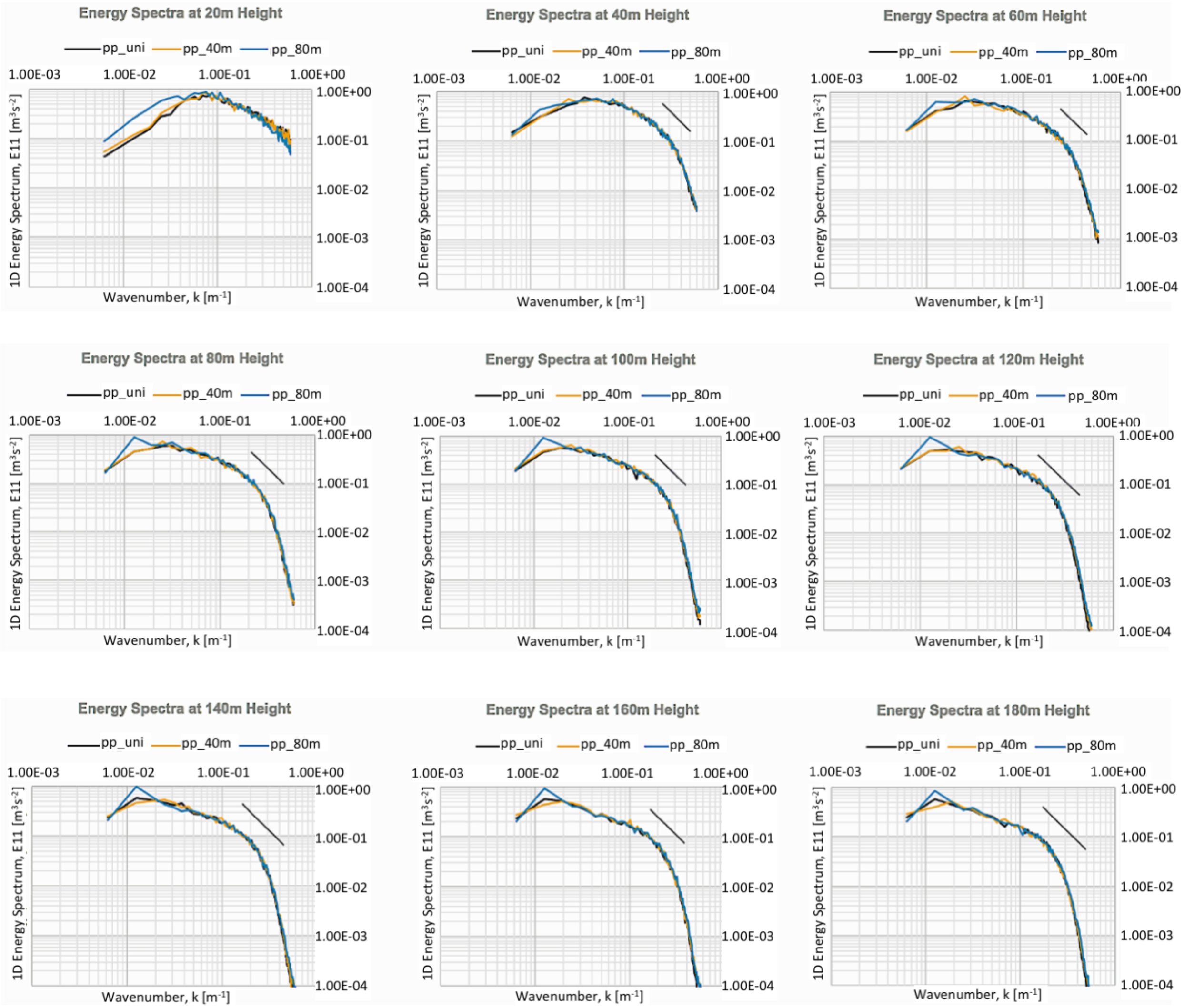

Figure 4.11. Energy spectra at different heights (from 20 m to 180 m) for three different types of vegetation heterogeneity: PP_uni (black), PP_40m (yellow), and PP_80m (Blue). Black lines in the plots indicate -5/3 slope.

This preliminary study showed that the vegetation heterogeneity and its length scale could play a role in the turbulence characteristics, and that this influence can be modeled by a canopy surface model in LES. Further analysis is required to validate this hypothesis and to understand how much impact the vegetation heterogeneity has on the hub-height turbulence characteristics and on wind-energy production.

5.0 Evaluation of Turbulence Statistics Using Online Coupling in WRF

5.1 Case Selection

The MMC team identified a number of specific case periods from the WFIP 2 field study to test various aspects of MMC in a region of complex terrain. Specifically, periods with time-varying conditions associated with frontal passages, topographic wakes, mountain waves, or cold pools were considered because they would be challenging situations for simulations completed using coupled models. These periods were selected using the WFIP 2 event log to identify periods during which the standard weather forecast models had sufficient skill to provide realistic boundary conditions and specific cases that are relevant to the wind-energy community due to large wind speeds, ramp events, or other factors. An additional point of consideration by the team was the availability of data from WFIP 2 Physics Site, which was not operational until after 9 July 2016. The case periods for testing mesoscale-microscale coupling in a region of complex terrain were as follows:

- 3–4 July 2016: This period includes a weak frontal passage over the WFIP 2 Physics Site and has the relative advantage of being comparatively free of clouds. Although the Physics Site was not fully operational for this period, it was selected because of the frontal passage.
- 7 November 2016: This period was selected because of the presence of a persistent cold pool over much of the Columbia Basin, with preliminary simulations suggesting the presence of mountain waves.
- 12 November 2016: This period includes a cold pool and a cold frontal passage leading to a wind ramp. The HRRR model suggests that Mount Hood's wake could extend to the Wasco site and this period was the focus of an NREL-led study focused on studying the impact of the *terra incognita* in complex terrain.
- 21 November 2016: This time period includes topographic wakes over much of the WFIP 2 domain and HRRR results suggested vertically propagating mountain waves.

5.2 MMC Simulation Assessment

Previous assessment of MMC demonstrated the advantages of nesting LESs within a mesoscale simulation compared with forcing the microscale simulation using tendencies derived from a standalone mesoscale simulation. The first phase of the assessment of MMC for simulation of flows in complex terrain therefore focused on nesting of LESs within a nested mesoscale simulation. For this purpose, we used the WRF model because of its nesting capability and its ability to represent the effects of turbulence on a wide range of scales through the use of either PBL parameterization or subgrid turbulence parameterization.

The model performance of the coupled mesoscale-to-microscale simulation was assessed using data from the WFIP 2 field study. The WFIP 2 field study took place from March 2016 to March 2017 in the area of the Columbia River. Among a number of instrumented sites throughout the region, one of the sites was dedicated to microscale, surface-layer flow observations. This site, labeled as the Physics Site, spans a couple of square kilometers at the Biglow Canyon Wind Farm. At the Physics Site, there were one 80-m tower, two 20-m towers, seven 10-m towers with sonic anemometers installed on different levels, and two 3-m meteorological surface stations.

As of 30 November 2017, most of the data from the WFIP 2 observational platforms were uploaded on the DOE A2e DAP at https://download.a2e.energy.gov. Some, but not all, of the data have been quality-controlled. However, data from the 20-m towers are not yet available through the DAP. Therefore, for the assessment, we focused on the data from the tall, 80-m tower.

The tall tower was equipped with four Metek sonic anemometers installed and maintained by Argonne National Laboratory, two at the 50-m above the ground level and two at the 80 m above the ground level. At each level, one sonic anemometer was mounted on a boom facing west and one on a boom facing south. An aerial view of the Physics Site is shown in Figure 5.1 (from Google Earth). The 80-m tower (not visible in the picture) was located at the eastern vertex of the triangle outlined with yellow lines. The terrain is gently rolling and the land use is heterogeneous; wheat fields (see Figure 5.2) and range land are crisscrossed with gullies. Furthermore, the view from the Physics Site to the west, the predominant wind direction, shows the complex terrain, including Mount Hood in the distance. Mount Hood rises to 3,429 m above sea level, while the 80-m tower is at the elevation of about 450-m. A few kilometers north of the wind plant is the Columbia River. The Columbia River Gorge is approximately 100-km due west of the wind plant.

The Physics Site has observational platforms arranged in a triangular shape on the west side of the wind plant to characterize the atmospheric surface layer, including wind profiles, wind shear, and turbulence unobstructed by the wind plant under the dominant wind direction. The 80-m tower was located east of the first row of wind turbines on the west side of the wind plant; however, as can be seen in Figure 5.1, it is located in a gap between adjacent turbines, and, therefore, it is also unobstructed by the westernmost row of turbines under westerly flows.

The selection of case studies for assessment of MMC was based on several requirements, of which the main requirement was that the case study needed to be of interest for wind-energy applications; e.g., the hub-height wind speed needed to be greater than approximately 4 ($m\ s^{-1}$). We also sought cases for which most if not all the observational platforms including, but not limited to, those at the Physics Site, were collecting data.

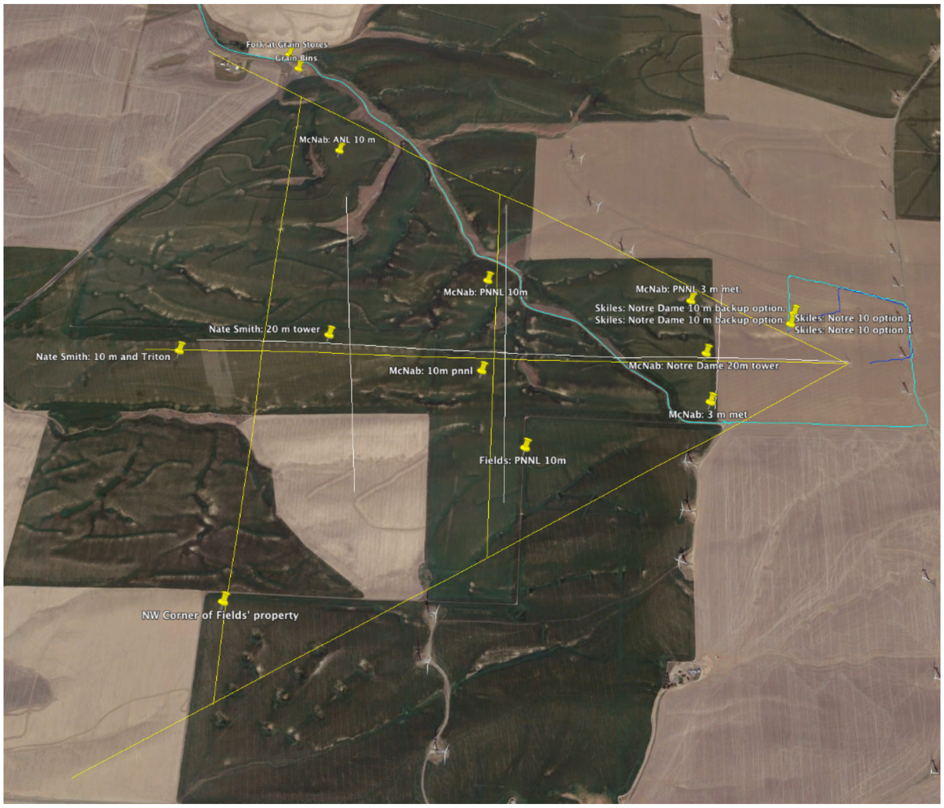

Figure 5.1. Aerial view of the Physics Site (from Google Earth). Yellow pins denote locations of the different meteorological towers.

Figure 5.2. View from the WFIP 2 Physics Site toward the west. Mount Hood can be seen in the distance.

An additional requirement was that the weather forecast provided by the HRRR forecasting system be relatively accurate, so that the coupling assessment results were minimally affected by the errors in mesoscale forcing. Another requirement was that the case be characterized by physical phenomena of interest for studies of the impact of complex terrain on wind-plant performance such as mountain waves, topographic wakes, drainage flows, gap flows, etc. Based on these requirements, 3 and 4 July 2016 and 21 November 2016 were selected for more detailed analysis of MMC. However, because the 80-m tower data are available from 14 July 2016 to 16 March 2017 our assessment focuses on the 21 November case study.

On 21 November 2016, mountain waves and topographic wakes were forecasted and observed. During the night between 20–21 November, the measured wind speed at the Physics Site was relatively low, 4–5 m s^{-1}; however, after 1900 UTC (11 a.m. local time) the wind speed increased to 10 m s^{-1}. The period between 1900–2300 UTC was simulated using the WRF model initialized with HRRR output. The WRF simulation setup included three domains. Table 5.1 lists the number of grid cells used on each of the three nests as well as corresponding grid cell sizes. The outermost parent domain, shown in Figure 5.3, extended over the area of more than 25,000 km^2 reaching all the way to the Pacific Ocean in the west. The second domain, shown as a black rectangle in Figure 5.3, used a subgrid turbulence model, thereby enabling the representation of large turbulence eddies. Although, the grid-cell size of 143 m used in domain 2 fell under the so-called *terra incognita*, between 100–1000 m, this domain includes Mount Hood and this grid-cell size is sufficient to resolve the largest eddies and topographic wakes. The third domain, covering nearly 50 km^2, centered on the Physics Site and was resolved with a grid-cell size of 13 m. An example of the flow field resolved by the two inner domains can be seen in Figure 5.4. In the left panels of Figure 5.4 a topographic wake caused by Mount Hood and the associated wind speed reduction are clearly visible.

Table 5.1. WRF model simulation domains, domain sizes, and grid-cell sizes.

Domain	D01	D02	D03
Grid cells in x and y	389	865	529
Grid cells in x and y	389	649	529
Grid-cell size: dx, dy [m]	1287	143	13

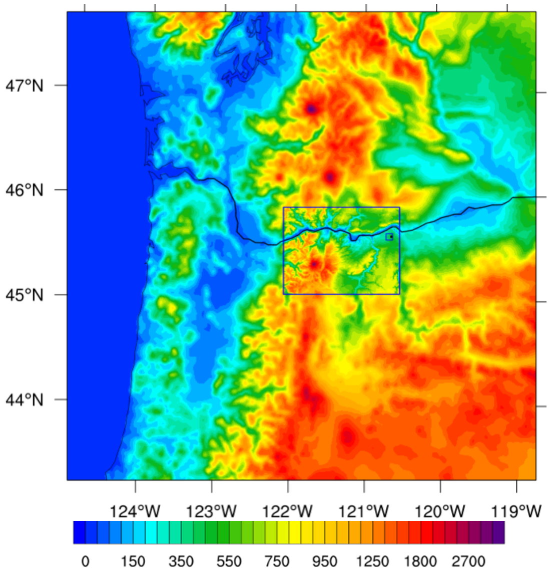

Figure 5.3. Parent domain with grid-cell size of 1.287 km and the nested second domain (black rectangle) with grid-cell size of 143 m.

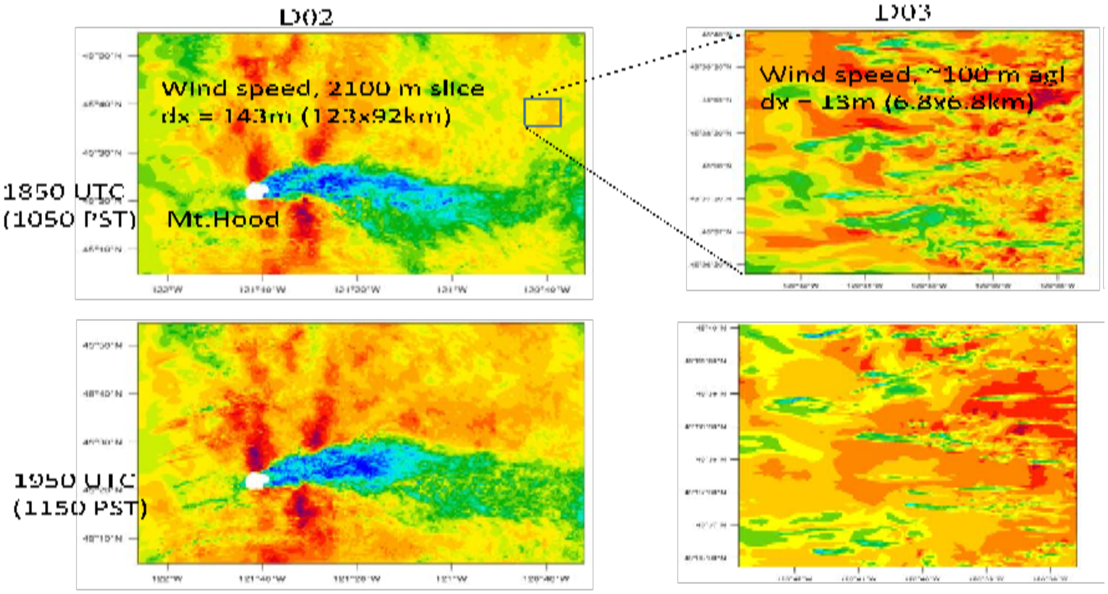

Figure 5.4. Wind speed: two horizontal slices 1 h apart at 2100 m above ground level for domain 2 (left panels) and 100 m above ground level for domain 3 (right panels).

To compare simulations to observations, we processed raw, quality-controlled observations by applying a tilt correction to the measured velocity components and subsampling signals to 1 Hz; i.e., the same frequency at which simulation results were saved. Figure 5.5 compares the measured and simulated time series of wind speed (left panel) and wind direction (right panel) at the two measurement levels of the 80 m tower. All of the time series analyzed here were computed using 20-minute running means. Comparison of simulated and measured time series demonstrates that the wind direction was captured well by the mesoscale simulation and that, over the period of interest, the wind direction was consistently westerly. During the first 2 h of the simulation between 1900–2100 UTC, the difference between measured and simulated wind speed was large, initially more than 6 m s^{-1}. By 2100 UTC, however, the difference was significantly reduced and the overall accuracy cannot be considered to be satisfactory. In Figure 5.6 the measured and simulated turbulent stress (left panel) and sensible heat flux (right panel) are compared. Overprediction of turbulent stress results from larger shear due to overprediction of wind speed during the first 2 h of the simulation, while turbulent sensible heat flux is predicted well during the same period. Although at 1900 UTC (11 local time) we can observe development of a convective PBL driven by increasing surface heat flux, an hour later, at noon local time, the surface flux starts decreasing, likely due to the presence of clouds. Overprediction of turbulent sensible heat flux in the middle of the simulation period may be attributed to errors in prediction of cloud coverage.

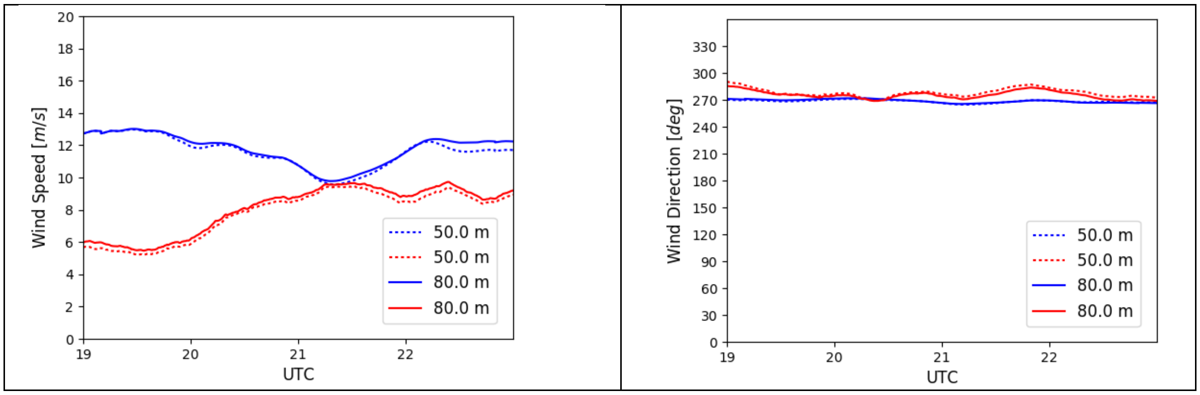

Figure 5.5. Wind speed (left panel) and wind direction (right panel) on 21 November 2017 at the 80-m tower of the WFIP 2 Physics Site. Red lines indicate measurements; blue lines indicate coupled mesoscale-to-microscale simulation results; a solid line indicates measurements and simulation results at 80 m above ground level; and a dotted line indicates measurements and simulation results 50 m above ground level.

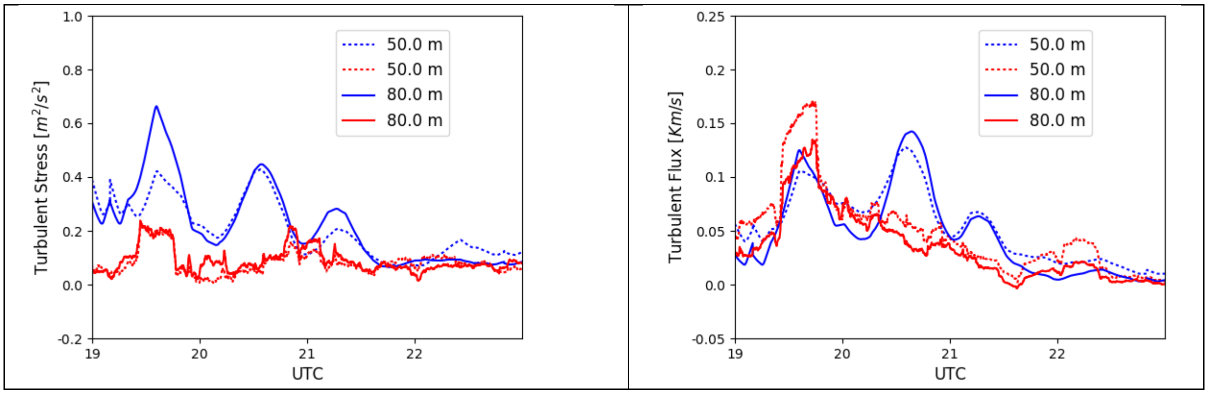

Figure 5.6. Turbulent stress (left panel) and sensible heat flux (right panel) measured at the 80 m tower at the WFIP 2 Physics Site. Red lines indicate measurements; blue lines indicate coupled mesoscale-to-microscale simulation results; a solid line indicates measurements and simulation results at 80 m above ground level; and a dotted line indicates measurements and simulation results 50 m above ground level.

The TKE shown in Figure 5.7 confirms the previous observation that overprediction of the wind speed results in larger shear, and, therefore, larger production of TKE causing larger levels of TKE compared with the measured TKE. During the last 2 h of the simulation, between 2100–2300 UTC, when the wind speed differences between simulation and observations converged, the simulated level of TKE is comparable to the observed level.

Frequency spectra of velocity components and potential temperature were computed using overlapping 20-minute time-series segments from the time period between 1900–2300 UTC (Figure 5.8). Both simulated and measured spectra were based on 1 Hz time series. Although measurements with sonic anemometers provided a 20 Hz signal, to compute spectra, we subsampled the measured signal to 1 Hz in order to compare it to the simulated signal. Relatively good agreement can be observed between the simulated and measured spectra. In particular, good agreement can be observed in the inertial range where all the spectra display a Kolmogorov's -5/3 power law. The drop-off in simulated spectra at high frequency can be attributed to the implicit filtering by a numerical scheme (at about $7\,\Delta x$).

This case demonstrates the difficulty of attempting to assess the performance of coupled mesoscale-to-microscale simulations. In coupled simulations, it is not easy to separate errors caused by errors in large-scale forcing from errors intrinsic to the coupling methodology. Even in the case where, based on expert opinion, the general synoptic situation was captured well, small differences in large-scale, upper-level flow can result in larger differences in boundary-layer flows at specific locations. Nevertheless, based on the limited assessment presented here, we can conclude that direct, online MMC represents a promising step toward achieving accurate multiscale simulations bridging the gap between mesoscale and microscale flows.

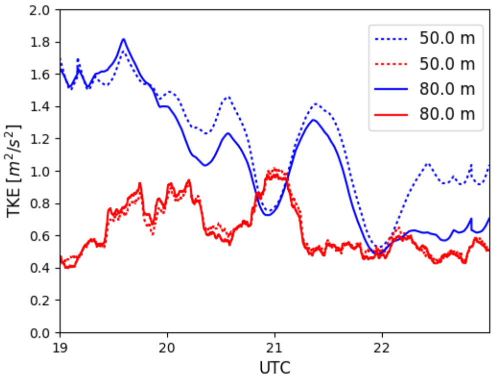

Figure 5.7. Turbulence kinetic energy. Red line indicates measurements and blue line indicates simulations at the WFIP 2 Physics Site; a solid line indicates measurements and simulation results at 80 m above ground level; and a dotted line indicates measurements and simulation results at 50 m above ground level.

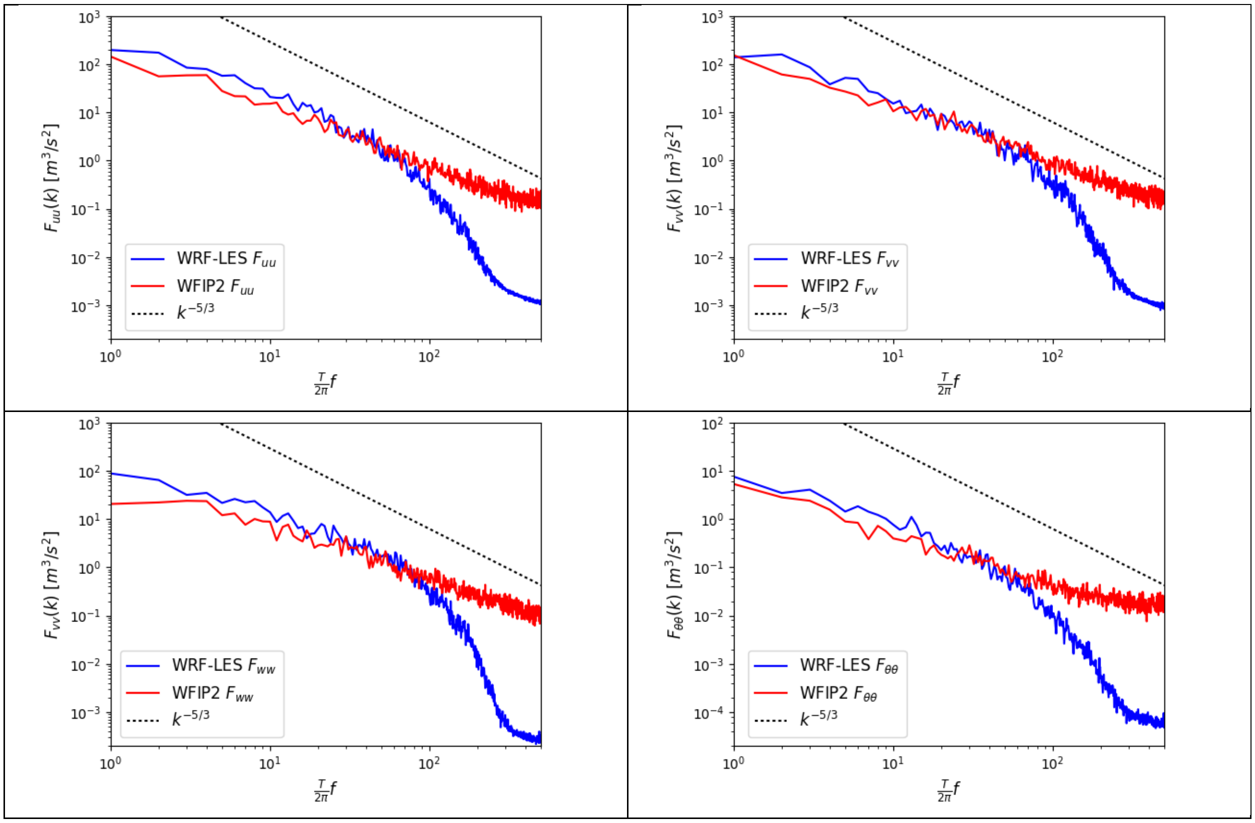

Figure 5.8. Frequency spectra of velocity components and potential temperature at the WFIP 2 Physics Site at 80 m above ground level. Spectra of the westerly component of velocity (top left panel), spectra of the northerly component of velocity (top right panel), spectra of the vertical component of velocity (bottom left panel), and potential temperature spectra (bottom right panel).

6.0 Summary, Context, and Next Steps

6.1 Summary of Results

A2e MMC project participants have been functioning as a team since mid-March 2015. The team has consisted of six DOE laboratories (ANL, LANL, LLNL, NREL, PNNL, and SNL [the latter's participation was dropped in FY17]) and NCAR (as a subcontractor to PNNL, the lead laboratory).

Within the context of a multiyear effort to develop, assess, and provide best-practice MMC recommendations for the A2e HPM framework, the third year of effort during 2017 focused on:

- documenting and assessing the impacts of modeling at the mesoscale in the *terra incognita*, including providing recommendations;
- assessing methods of initiating turbulence in microscale simulations;
- exploring methods to better represent the surface layer; and
- evaluating the turbulence statistics for model case studies in complex terrain.

6.1.1 Findings and Recommendations Relative to Modeling in the *Terra Incognita*

With respect to the *terra incognita* analysis, Section 2.1 presented the results of the analysis of the impact of the *terra incognita* on microscale simulations. A major finding of that portion of the study is that the upper limit of the *terra incognita* range should be based on the depth of the boundary layer. The results highlighted the importance of including a mesoscale nest, which leads to more realistic simulations in the flow simulated with the microscale model. The results also suggest that mesoscale domains with grid spacings in the *terra incognita* do not have a large impact on the microscale results. Guidance for configuring coupled simulations includes the following:

- Users should avoid mesoscale domains that employ grid spacing smaller than z_i due to unrealistic features in the flow. If, however, the primary interest is in the results associated with the microscale domain, this advice could be ignored for the coupled WRF/WRF-LES systems. The same may not be true for other modeling systems.
- Users should feel free to select either the MYNN or YSU boundary-layer parameterization. The fine-scale turbulence properties found on the microscale domain are nearly independent of the boundary-layer parameterization used on the mesoscale domains.
- Users should avoid driving microscale simulations with large-scale reanalysis products. Fully coupled simulations that employ mesoscale nests have more energy at larger wavelengths than microscale simulations driven by a reanalysis product alone.

Results presented in Section 2.2 demonstrated the impact of the *terra incognita* in complex terrain. The simulations and observations show periods of higher and lower wind speeds during the latter part of the case day, but the exact timing and magnitude of these changes are different between the observations and the 3-km and 750-m domains. Because this case day exhibited wave activity and a wake from Mount Hood that was meandering, capturing these high/low wind speed patterns perfectly in time is nearly impossible for a mesoscale model. The goal of improving simulations in the *terra incognita* is not likely to be achieved by resolving turbulence in a mesoscale model, but rather by determining whether wave-like structures are realistic features or numerical noise. We found that the performance of the model depends on the site of interest and its situation within the complex terrain. The finer the grid spacing, the more realistic the terrain representation. For the case studied, the simulated waves were perpendicular to the flow and realistic, and no *terra incognita* issues were found. This is in contrast to our study last year in flat terrain, where unrealistic rolls were formed parallel to the flow. An explanation for that might be that complex terrain exhibits more horizontal variations, which could suppress the creation of unrealistic numerical features.

Follow-on work should include a comparison of these simulations in complex terrain with simulations using the improved HRRR model, which was optimized to produce realistic simulations in the *terra incognita* within the WFIP 2 project by implementing 3-D boundary-layer parameterizations.

This study confirmed that for coupled WRF/WRF-LES systems, the microscale solution might yield correct flow fields even if the mesoscale solution exhibits unrealistic features in the flow due to *terra incognita* issues. It will be important to know whether this is true for other modeling systems, such as standalone microscale solvers like Nalu or OpenFOAM.

The final section considered two case days for complex terrain and accomplished formal assessment at resolutions of 3 km (mesoscale) and 750 m (inside the *terra incognita*). The results of these two case studies provided mixed indications regarding the impact of configuring the model to capture phenomena at *terra incognita* spatial scales. In some cases (e.g., wind direction profiles for 12 November 2016 and wind direction and speed profiles for 21 November 2016), the 750-m version of the model appeared to capture observed variations across time and altitude better than the 3-km mesoscale model version. However, these differences were not consistent. For the case described in Section 2.2, further evidence that the observed rolls were physical was presented.

6.1.2 Findings and Recommendations on Generating Microscale Turbulence

Several different methods were examined to accelerate the development of turbulence within LESs in general settings that do not permit the traditional method of using periodic lateral boundary conditions. Two methods based on using precursor simulations to generate turbulent inflow for LES and three methods based on perturbing smooth mesoscale inflow upon its entry into the LES domain were evaluated.

One precursor method used a periodic LES driven by mesoscale forcing parameters, to provide turbulent inflow to an offline microscale simulation over complex terrain. The method requires precomputation of both the mesoscale forcing and the microscale turbulence field, which is expensive. However, once those simulations are complete, the offline microscale simulation has the advantage of being able to use a significantly smaller domain, due to reduction of the fetch required to generate turbulence upwind of an area of interest. This approach was successfully applied over complex terrain at the WFIP 2 Physics Site, showing great promise as a means of providing instantaneous turbulent inflow. Future work will compare the approach to instrumentation within the simulation domains and examine the evolution of inflow turbulence fields that do not exactly match the current terrain or meteorological conditions to determine whether an upwind fetch is still required for the turbulence to adapt to local conditions.

The expense of precomputation of the microscale turbulence field can be significantly mitigated by saving the precomputed fields in a library. A library of precomputed microscale simulations spanning a range of meteorological forcings could provide a means of incorporating appropriate inflow turbulence into microscale simulations during time-varying meteorological conditions. A prototype of such a library, and a second technique for integrating the library files into an offline LES, asynchronous coupling, was also examined. One hundred eight LESs were executed over a range of wind speeds, temperatures, surface roughnesses, and model resolutions, based upon a neutral boundary-layer case study from the SWiFT facility examined by the project team during FY15 and FY16. Incorporation of flow from the precomputed turbulence fields into offline LESs via the asynchronous coupling procedure was attempted, but problems were encountered with the idealized open lateral boundary conditions used within the offline LES. Future work will address issues with the open lateral boundary conditions, examine the method in a meteorologically varying case study such as a diurnal cycle, and also explore machine-learning techniques to improve the efficiency of the approach.

Incorporation of inflow perturbations were also examined. Two synthetic approaches based upon the spectral perturbations, TurbSim and Gabor KS, were investigated in neutral conditions. Simulations using each method produced turbulence rapidly at the LES inflow boundary, but each method produced anomalous TKE characteristics relative to a reference simulation. TKE using the TurbSim method nearly equilibrated after about 4 km of fetch, thereafter gradually decreasing with further distance, while that using the Gabor KS method exhibited a long-term high-amplitude oscillation that never equilibrated. Potential remediation strategies were identified and will be explored during FY18. The synthetic approaches were also used to investigate the impacts of turbulence on turbine-relevant QOIs characterizing machine performance and fatigue loading, via coupling the microscale flow field to the FAST aeroelastic model.

An alternative method for instigating turbulence development on LESs, the SCPM (stochastic cell-perturbation method) of Muñoz-Esparza et al. (2015) (ME15) was also examined, this time in real-data case studies involving full physics multiscale MMC simulations conducted within the WRF model. The SCPM used herein was modified from ME15 to run concurrently with the nested LES domains. The SCPM of ME15 was a two-step process, requiring first running the mesoscale simulation to obtain operational parameters for the SCPM, then running the coupled simulation with the nested LES domain(s) embedded, during which the SCPM parameters were read in via an auxiliary input file. The SCPM uses relevant mesoscale information passed down to the nested LES domain(s) from the finest mesoscale domain within one coupled simulation.

The new SCPM was examined in a case study consisting of a diurnal cycle at the SWiFT facility, simulated both with and without the SCPM. Simulations revealed that the SCPM neither improved nor degraded the simulations during the late morning to midafternoon hours because of strong convective conditions leading to rapid turbulence generations via surface buoyancy. However, the SCPM considerably improved the representation of turbulence during the neutral and stable conditions later in the afternoon and overnight. The SCPM was also applied to a case study at the WFIP 2 site, where it again was shown to accelerate the development of turbulence. However, it was determined that the perturbations were applied over too shallow a depth, due to the small mesoscale-diagnosed PBL height at the beginning of the period. This and other observations from the simulations provided valuable guidance to further improve performance of the SCPM during FY18.

Although the SCPM of ME15 applied perturbations to the temperature field, application of perturbations to velocities was also investigated. It was shown that perturbations to the horizontal and vertical velocity components could produce faster equilibration of some turbulence parameters than the thermal perturbations, and that vertical velocity components produce the fastest equilibration. However, other quantities were better matched by the thermal perturbations. The investigations suggest that a combination of velocity and thermal perturbations could perform better overall than either method alone. Further examination will be carried out in FY18.

Each of the turbulence-generation methods investigated during FY17 shows promise for specific applications and is worthy of continued development. A suite of canonical case studies representing industry-relevant use cases for which each technique could be intercompared and evaluated against observations could provide further useful guidance on the selection of optimal techniques for given applications.

6.1.3 Findings and Recommendations Relative to Modeling the Surface Layer

Three different explicit canopy physics modules were examined to increase the fidelity of surface- and boundary-layer flow in LESs. These parameterizations augment or replace the standard MOST (Monin-Obukhov Similarity Theory [Monin and Obukhov 1954]) that is commonly used in atmospheric LES, despite its tenuous applicability to turbulence resolving flows in unsteady, heterogeneous settings.

Two canopy models were implemented into the WRF model—an explicit resolved canopy for canopy elements taller than the vertical resolution of the LES and a pseudo-canopy model for surfaces characterized by small canopy elements. The explicit resolved canopy implementation was validated against a test case from the literature, consisting of a horizontally homogeneous canopy with height variability representing a forest. The WRF model can now recover correct velocity and turbulence characteristics over tall vegetated canopies. Following the implementation of the explicit canopy model, a pseudo-canopy model using concepts from the explicit canopy, but tailored for smaller roughness elements, was developed. Simulations with the pseudo-canopy model over flat terrain with small roughness lengths produced significant improvements in the vertical distributions of velocity and turbulence characteristics relative to the standard MOST implementation, thereby showing great promise for microscale wind-energy applications.

A heterogeneous canopy model, which resolves individual trees in the horizontal direction, was also examined within the HIGRAD model, likewise showing applicability to wind-energy simulations in regions characterized by patchy vegetation. The canopy models implemented into WRF can also accommodate horizontal heterogeneity in canopy features, for which the HIGRAD simulations could provide useful validation data. Further development of the canopy approaches and their validation in more complex environments will be undertaken during FY18.

6.1.4 Findings and Recommendations Relative to Turbulence Generated in Nested Simulations in Complex Terrain

Formal assessment was accomplished for a complex terrain case from the WFIP 2 observational experiment using observations at the WFIP 2 Physics Site on 21 November 2016. This case study was characterized by topographic wake and mountain waves over the area, but the Physics Site may not have been directly affected by either of these phenomena. The mesoscale-to-microscale simulation was carried out using WRF's nesting capability; the parent nest was run in mesoscale mode while two inner nests were run in LES mode. This simulation did not include any modifications to the WRF model. Initial conditions and boundary conditions for the mesoscale-to-microscale simulation were provided by the HRRR forecasting system. The expert assessment of the HRRR forecast over Columbia River Gorge area for the period of interest indicated overall skillful prediction. However, the comparison of the mesoscale-to-microscale coupled simulation at the Physics Site showed significant differences between observed and simulated wind speed. During the period from 1900–2100 UTC, the wind speed error was up to 6 ms^{-1}. Large wind speed errors result in large differences between simulated and observed TKE and turbulent stress. Turbulent sensible heat flux is predicted quite well except possibly during relatively short intervals when the model did not accurately capture cloud cover. Spectral analysis showed excellent agreement between measured and simulated turbulence frequency spectra in the well-resolved portion of the inertial range. Good agreement indicates then even when the mesoscale flow is not captured accurately, the turbulent energy transfer from large turbulent production scales to smaller scales can be represented accurately in a well-resolved LES. At large scales, the errors in mesoscale forcing are shown by larger amounts of TKE than observed. The assessment of MMC within a single model confirms the feasibility and validity of the approach that relies on online coupling within the same model.

6.2 Context in A2e and Next Steps

The MMC team has been working with the DAP team to archive the model data from the selected cases. In FY17, modeling efforts focused on coupled modeling in complex terrain. To that end, the MMC team is working with the WFIP 2 team to identify appropriate cases in the wind region of the Pacific Northwest and to use those case studies to provide recommendations about how to best couple the microscale to the mesoscale models.

The MMC team has had continuing conversations with the HPM team and expects to continue working closely with them to assure that the lessons learned from the coupling exercises are included in the new HPM framework. Our team has been extensively documenting the necessity for mesoscale forcing to assure appropriate microscale turbulence features, especially for nonstationary conditions and in complex terrain. The next step is to work in a larger team to transition this knowledge to an environment where it is fully captured in the modeling framework.

The MMC team has been working together very effectively and collaboratively. Team members have been working together to formulate the appropriate sensitivity studies, then to each take some of the simulations to allow full comparison with a distributed work load. When one approach is effective, other team members quickly adopt it in their own code. The team's fully collaborative work style is designed to produce the best framework available for coupled modeling.

This project is expected to continue into FY18 and beyond. During FY17, the team formulated goals and objectives for the continuing work. The specific objectives identified are to:

- establish a validation framework with well-defined performance metrics and apply it to benchmark wind-plant simulation cases;
- improve the current state-of-the-science of coupling mesoscale information into high-fidelity HPC-based wind-plant simulations in order to achieve a measurable reduction of error in the prediction of wind speed and turbulence characteristics;
- disseminate our methods to stakeholders;
- verify and validate results using formal and reproducible techniques; and
- quantify the uncertainty in the results.

Specific activities and details of implementation were also configured for the next 3 years to assure that this work accomplishes its goals and provides value to industry in order to facilitate modeling of wind-plant flow, thereby enabling the wind industry to deploy wind energy more economically and efficiently. The new tools developed in this work will be usable for modeling the details of wind plants for resource assessment, forecasting wind power, and allowing wind-plant level control systems, among other uses.

7.0 References

Bailey BH. 2013. “The financial impact of wind plant uncertainty.” North American Wind Energy Academy Symposium, Boulder, Colorado, August 6, 2013.

Bokharaie VS, P Bauwererts, and J Meyers. 2016. “Wind-farm layout optimization using a hybrid Jensen-LES approach.” (Wind Engineering Science and Discussion).

Brasseur JG and T Wei. 2010. “Designing large-eddy simulation of the turbulent boundary layer to capture law-of-the-wall scaling.” *Physics of Fluids* 22:021303.

Brown AR, JM Hobson, and N Wood. 2001. “Large-eddy simulation of neutral turbulent flow over rough sinusoidal ridges.” *Boundary-Layer Meteorology* 98:411–441.

Ching J, R Rotunno, M LeMone, A Martilli, B Kosović, PA Jimenez, and J Dudhia. 2014. “Convectively Induced Secondary Circulations in Fine-Grid Mesoscale Numerical Weather Prediction Models.” *Monthly Weather Review* 142:3284–3302, doi: 10.1175/MWR-D-13-00318.1.

Chow FK, RL Street, M Xue, and JH Ferziger. 2005. “Explicit filtering and reconstruction turbulence modeling for large-eddy simulation of neutral boundary layer flow.” *Journal of Atmospheric Sciences* 62: 2058–2077.

Churchfield MJ, S Lee, PJ Moriarty, LA Martinez, S Leonardi, G Vijayakumar, and JG Brasseur. 2012. *A Large-Eddy Simulation of Wind-Plant Aerodynamics*. NREL/CP-5000-53554, National Renewable Energy Laboratory, Golden, Colorado.

Deardorff JW. 1970. “A numerical study of three-dimensional turbulent channel flow at large Reynolds numbers.” *Journal of Fluid Mechanics* 41:453–480.

Dwyer MJ, EG Patton, and RH Shaw. 1997. “Turbulent kinetic energy budgets from a large-eddy simulation of airflow above and within a forest canopy.” *Boundary-Layer Meteorology* 84:23–43.

Gaudet BJ, A Deng, DR Stauffer, and A Gassmann. 2012. “Eddy Seeding for improved WRF-LES simulations using realistic lateral boundary conditions.” *WRF Users' Workshop.* National Center for Atmospheric Research, Boulder, Colorado.

Ghate AS and SK Lele. 2017. “Subfilter-scale enrichment of planetary boundary layer large eddy simulation using discrete Fourier-Gabor modes” *Journal of Fluid Mechanics* 819:494–539, doi:10.1017/jfm.2017.187.

Haupt SE, A Anderson, L Berg, B Brown, MJ Churchfield, C Draxl, BL Ennis, Y Fang, B Kosović, R Kotamarthi, R Linn, JD Mirocha, P Moriarty, D Muñoz-Esparaza, R Rai, and WJ Shaw. 2015. *First Year Report of the A2e Mesoscale to Microscale Coupling Project.* PNNL-25108, Pacific Northwest Laboratory Report, Richland, Washington. 124 pp.

Haupt SE, A Anderson, R Kotamarthi, JJ Churchfield, Y Feng, C Draxl, JD Mirocha, E Quon, E Koo, W Shaw, R Linn, L Berg, B Kosović, R Rai, B Brown, and BL Ennis. 2017. *Second Year Report of the Atmosphere to Electrons Mesoscale to Microscale Coupling Project: Nonstationary Modeling Techniques and Assessment*. PNNL-26267, Pacific Northwest Laboratory. Richland, Washington. 156 pp.

Hong S-Y, Y Noh, and J Dudhia. 2006. “A New Vertical Diffusion Package with an Explicit Treatment of Entrainment Processes.” *Monthly Weather Review* 134:2318–2341.

Honnert R, V Masson, and F Couvreux. 2011. “A Diagnostic for Evaluating the Representation of Turbulence in Atmospheric Models at the Kilometric Scale.” *Journal of Atmospheric Sciences* 68:3112–3131.

IEC (International Electrotechnical Commission). 2014. *Wind Turbines – Part 1: Design Requirements*. IEC 61400-1, Edition 3.1, Geneva, Switzerland.

Jonkman JM and ML Buhl. 2005. *FAST User’s Guide*. NREL/EP-500-38230, National Renewable Energy Laboratory, Golden, Colorado.

Jonkman BJ and ML Buhl. 2007. *TurbSim User’s Guide*. NREL/TP-500-41136, National Renewable Energy Laboratory, Golden, Colorado.

Jonkman JM, JA Annoni, G Hayman, B Jonkman, and A Purkayastha. 2017. *Development of FAST.Farm: A New Multiphysics Engineering Tool for Wind Farm Design and Analysis*. NREL/CP-5000-67528, National Renewable Energy Laboratory, Golden, Colorado.

Kelley ND. 2011. *Turbulence-Turbine Interaction: The Basis for the Development of the TurbSim Stochastic Simulator*. NREL/TP-5000-52353, National Renewable Energy Laboratory, Golden, Colorado.

Kirkil G, JD Mirocha, FK Chow, and E Bou-Zeid. 2012. “Implementation and evaluation of dynamic subfilter-scale stress models for large-eddy simulation using WRF.” *Monthly Weather Review* 140*:*266–284.

Kosović B. 1997. “Subgrid-scale modelling for the large-eddy simulation of high-Reynolds-number boundary layers.” *Journal of Fluid Mechanics* 336:151–182.

Lilly DK. 1967. “The representation of small-scale turbulence in numerical simulation experiments.” In IBM Scientific Computing Symposium on environmental sciences, pages 195–210, Yorktown Heights.

Lim HC, TG Thomas, and IP Castro. 2009. “Flow around a cube in a turbulent boundary layer: LES and Experiment.” *Journal of Wind Engineering and Industrial Aerodynamics* 97:96–109.

Linn RR, J Winterkamp, JJ Colman, C Edminster, and JD Bailey. 2005. “Modeling interactions between fire and atmosphere in discrete element fuel beds.” *International Journal of Wildland Fire* 14 (1):37–48.

Lund T, X Wu, and KD Squires. 1998. “Generation of Turbulent Inflow Data for Spatially-Developing Boundary Layer Simulations.” *Journal of Computational Physics* 140:233–258.

Mann J. 1994. “The spatial structure of neutral atmospheric surface-layer turbulence.” *Journal of Fluid Mechanics* 273:141–168.

Mayor SD, PR Spalart, and GJ Tripoli. 2002. “Application of a perturbation recycling method in the Large-Eddy Simulation of a mesoscale convective internal boundary layer.” *Journal of Atmospheric Science* 59:2385–2395.

Mehta D, AH van Zuijlen, B Koren, JG Holierhoek, and H Bijl. 2014. “Large-Eddy Simulation of wind farm aerodynamics: A review.” *Journal of Wind Engineering and Industrial Aerodynamics* 133:1–17.

Mirocha JD, JK Lundquist, and B Kosović. 2010. “Implementation of a Nonlinear Subfilter Turbulence Stress Model for Large-Eddy Simulation in the Advanced Research WRF Model.” *Monthly Weather Review* 138:4212–4228.

Moeng C-H. 1984. “A Large Eddy Simulation Model for the Study of Planetary Boundary-Layer Turbulence.” *Journal of Atmospheric Sciences* 41:2052–2062.

Monin AS and AM Obukhov. 1954. “Basic laws of turbulent mixing in the surface layer of the atmosphere.” *Tr. Akad. Nauk SSSR Geofiz. Inst.* 24:163–187; English translation by John Miller, (1959).

Muñoz-Esparza D, B Kosović, J van Beeck, and JD Mirocha. 2015. “A stochastic perturbation method to generate inflow turbulence in large-eddy simulation models: Application to neutrally stratified atmospheric boundary layers.” *Physics of Fluids* 27:035102.

Nakanishi M and H Niino. 2009. “Development of an Improved Turbulence Closure Model for the Atmospheric Boundary Layer.” *Journal of the Meteorological Society of Japan. Ser. II* 87: 895–912.

Patton EG, KJ Davis, MC Barth, and PP Sullivan. 2001. “Decaying scalars emitted by a forest canopy: A numerical study.” *Boundary-Layer Meteorology* 100(1):91–129.

Patton EG and JJ Finnigan. 2012. *Canopy turbulence*. Vol. 1, Fernando, HJS (ed.), Chap. 24, 311–327, CRC Press.

Pimont F, J-L. Dupuy, RR Linn, and S Dupont. 2009. “Validation of FIRETEC wind-flows over a canopy and a fuel-break.” *International Journal of Wildland Fire* 18(7):775–790.

Rai RK, LK Berg, B Kosović, JD Mirocha, MS Pekour, and WJ Shaw. 2017. “Comparison of measured and numerically simulated turbulence statistics in a convective boundary layer over complex terrain.” *Boundary-Layer Meteorology* 163:69–89.

Sanderse B, SP van der Pijl, and B Koren. 2011. “Review of computational fluid dynamics for wind turbine wake aerodynamics.” *Wind Energy* 14:799–819.

Shaw WJ, JK Lundquist, and SJ Schreck. 2009. “Workshop on Research Needs for Wind Resource Characterization.” *Bulletin of the American Meteorological Society* 90:535–538.

Shaw RH and U Schumann. 1992. “Large-eddy simulation of turbulent flow above and within a forest.” *Boundary-Layer Meteorology* 61(1–2):47–64.

Shaw RH and EG Patton. 2003. “Canopy element influences on resolved-and subgrid-scale energy within a large-eddy simulation.” *Agricultural and Forest Meteorology* 115:5–17.

Shin HH and J Dudhia. 2016. “Evaluation of PBL Parameterizations in WRF at Subkilometer Grid Spacings: Turbulence Statistics in the Dry Convective Boundary Layer.” *Monthly Weather Review* 144:1161–1177.

Shin HH and S-Y Hong. 2013. “Analysis of Resolved and Parameterized Vertical Transports in Convective Boundary Layers at Gray-Zone Resolutions.” *Journal of Atmospheric Sciences* 70:3248–3261.

Skamarock W, J Klemp, J Dudhia, D Gill, D Barker, M Duda, X-Y Huang, W Wang, and J Powers. 2008. A Description of the Advanced Research WRF Version 3. NCAR/TN-475+STR, NCAR Technical Note, National Center for Atmospheric Research, Boulder, Colorado.

Spalart PR. 1988. "Direct simulation of a turbulent boundary layer up to Rθ = 1410." *Journal of Fluid Mechanics* 187:61–98.

Stevens RJAM, J Graham, and C Meneveau. 2014. "A concurrent precursor inflow method for Large Eddy Simulations and applications to finite length wind farms." *Renewable Energy* 68:46–50.

Thomas TG and JJR Williams. 1999. "Generating a wind environment for large eddy simulation of bluff body flows." *Journal of Wind Engineering* 82:189–208.

Troldborg N, GC Larsen, HA Madsen, KS Hansen, JN Sørensen, and R Mikkelsen. 2011. "Numerical simulations of wake interaction between two wind turbines at various inflow conditions." *Wind Energy* 14, 859–876.

Wyngaard JC. 2004. Toward numerical modeling in the "*Terra incognita*." *Journal of Atmospheric Sciences* 61:1816–1826.

Xie Z-T and IP Castro. 2008. "Efficient Generation of Inflow Conditions for Large Eddy Simulation of Street-Scale Flows." *Flow, Turbulence, and Combustion* 81(3):449–470.

Appendix A

List of Project Publications

Journal Papers:

Mirocha, J.D., M.J. Churchfield, D. Muñoz-Esparaza, R. Rai, Y. Feng, B. Kosović, S.E. Haupt, B. Brown, B.L. Ennis, C. Draxl, J.S. Rodrigo, W.J. Shaw, L.K. Berg, P. Moriarty, R. Linn, R.V. Kotamarthi, R. Balakrishnan, J. Cline, M. Robinson, and S. Ananthan, 2017: Large-Eddy Simulation sensitivities to variations of configuration and forcing parameters in canonical boundary layer flows for wind energy applications, submitted to *Wind Energy Science.*

Abstract: The sensitivities of idealized large-eddy simulations (LES) to variations of model configuration and forcing parameters on quantities of interest to wind power applications are examined. Simulated wind speed, turbulent fluxes, spectra, and cospectra are assessed in relation to variations of two physical factors—geostrophic wind speed and surface roughness length—and several model configuration choices, including mesh size and grid aspect ratio, turbulence model, and numerical discretization schemes, in three different code bases. Two case studies representing nearly steady neutral and convective atmospheric boundary layer flow conditions over flat terrain, occurring at the Sandia Scaled Wind Farm Technology test facility, were used to force and assess idealized LES using periodic lateral boundary conditions. Comparison with fast-response velocity measurements at five heights within the lowest 50 m indicates that most model configurations performed similarly overall, with differences between observed and predicted wind speed generally smaller than measurement variability. Simulations of convective conditions produced turbulence quantities and spectra that matched the observations well, while those of neutral simulations produced good predictions of stress, but smaller than observed magnitudes of turbulence kinetic energy, likely due to tower wakes influencing the measurements during the neutral case. Although sensitivities to model configuration choices and variability in forcing can be considerable, idealized LES are shown to reliably reproduce quantities of interest to wind-energy applications within the lower PBL during quasi-ideal, nearly steady neutral and convective conditions.

Rai, R.K., L.K. Berg, B. Kosović, J.D. Mirocha, M.S. Pekour, and W.J. Shaw, 2016: Comparison of measured and numerically simulated turbulence statistics in a convective boundary layer over complex terrain. *Bound.-Layer Meteor.*, **163**, 69-98.

Abstract: The Weather Research and Forecasting (WRF) model can be used to simulate atmospheric processes ranging from quasi-global to tens of m in scale. Here we employ large-eddy simulation (LES) using the WRF model, with the LES domain nested within a mesoscale WRF model domain with grid spacing decreasing from 12.15 km (mesoscale) to 0.03 km (LES). We simulate real-world conditions in the convective planetary boundary layer over an area of complex terrain. The WRF-LES model results are evaluated against observations collected during the U.S. Department of Energy-supported Columbia Basin Wind Energy Study. Comparison of the first- and second-order moments, turbulence spectrum, and probability density function of wind speed shows good agreement between the simulations and observations. One key result is to demonstrate that a systematic methodology needs to be applied to select the grid spacing and refinement ratio used between domains, to avoid having a grid resolution that falls in the grey zone and to minimize artifacts in the WRF-LES model solutions. Furthermore, the WRF-LES model variables show large variability in space and time caused by the complex topography in the LES domain. Analyses of WRF-LES model results show that the flow structures, such as roll vortices and convective cells, vary depending on both the location and time of day as well as the distance from the inflow boundaries.

Rai, R.K., L.K. Berg, M. Pekour, W.J. Shaw, B. Kosović, J.D. Mirocha, and B.L. Ennis, 2017: Spatio-temporal variability of turbulence kinetic energy budgets in the convective boundary layer over both simple and complex terrain. *J. Appl. Meteor. and Climatol.,* doi:10.1175/JAMC-D-17-0124.1, in press.

Abstract: The assumption of subgrid-scale horizontal homogeneity within a model grid cell, which forms the basis of subgrid-scale turbulence closures used by mesoscale models, becomes increasingly tenuous as grid spacing is reduced to a few kilometers or less, such as in many emerging high-resolution applications. Herein, we use the turbulence kinetic energy budget equation to study the spatiotemporal variability in two types of terrain—complex (Columbia Basin Wind Energy Study [CBWES] site, north-eastern Oregon) and flat (Scaled Wind Farm Technology [SWiFT] site, West Texas) using the Weather Research and Forecasting (WRF) model. In each case six nested domains (three domains each for mesoscale and large-eddy simulation [LES]) are used to downscale the horizontal grid spacing from ∼10 km to ∼10 m using the WRF model framework. The model output was used to calculate the values of the turbulence kinetic energy budget terms in vertical and horizontal planes as well as the averages of grid cells contained in the four quadrants (a quarter area) of the LES domain. The budget terms calculated along the planes and the mean profile of budget terms show larger spatial variability at the CBWES site than at the SWiFT site. The contribution of the horizontal derivative of the shear production term to the total shear production was found to be ≈45% and ≈15% at the CBWES and SWiFT sites, respectively, indicating that the horizontal derivatives applied in the budget equation should not be ignored in mesoscale model parameterizations, especially for cases with complex terrain with <10 km scale.

Conference Papers and Presentations: (presenter in **Bold)**

Cline, J., S.E. Haupt, and W. Shaw, 2017: Meteorology Research in DOE's Atmosphere to Electrons (A2e) Program, WindTech International Conference on Future Technologies in Wind Energy, Boulder, CO, October 24.

Churchfield, M., 2017: A Strategy for Performing Mesoscale-Driven Microscale Simulations in Complex Terrain, North American Wind Energy Symposium, Ames, IA, September.

Draxl, C., Churchfield, M., and Rodrigo, J.S., 2017: Coupling the Mesoscale to the Microscale Using Momentum Budget Components, North American Wind Energy Symposium, Ames, IA, September.

Draxl, C., Churchfield, M., and Rodrigo, J.S., 2017: Coupling the Mesoscale to the Microscale Using Momentum Budget Components, American Meteorological Society Annual Meeting, Seattle, WA, January.

Haupt, S.E., L. Berg, M. Churchfield, J. Cline, J. Mirocha, B. Kosović, C. Draxl, R. Rai, R. Kostmarthi, M. Robinson, and W. Shaw, 2017: The US DOE A2e Mesoscale to Microscale Coupling Project: Nonstationary Modeling Techniques and Assessment, International Conference on Energy and Meteorology, Bari, Italy, June 28.

Haupt, S.E., **J. Cline**, W. Shaw, L. Berg, M. Churchfield, J. Mirocha, B. Kosović, C. Draxl, R. Rai, and R. Kotamarthi, 2017: The US DOE A2e Mesoscale to Microscale Coupling Project: Nonstationary Modeling Techniques and Assessment, European Geophysical Union, Vienna, Austria, April 26.

Haupt, S.E., W. Shaw, and B. Kosović, 2016: The DOE A2e Mesoscale to Microscale Coupling Project, American Meteorological Society Symposium on Boundary Layers and Turbulence, Salt Lake City, UT, June 20.

Haupt, S.E., 2016: Meteorology Models Enabling Wind Energy, Wyoming Renewable Energy Summit, Laramie, WY, June 13. Invited Keynote.

Haupt, S.E., W. Shaw, and B. Kosović, 2015: Meso- to Microscale Coupling Project, WindTech Workshop, London, Ontario, Canada, October 19.

Kosović**, B.,** J.D. Mirocha, M.J. Churchfield, D. Muñoz-Esparza, R.K. Rai, Y. Feng, S.E. Haupt, B. Brown, B.L. Ennis, C. Draxl, J. Sanz Rodrigo, W.J. Shaw, L.K. Berg, P. Moriarty, R. Linn, and R.V. Kotamarthi, 2017: Assessment of Large-Eddy Simulations of the Atmospheric Boundary Layer for Wind Energy Applications, WindTech International Conference on Future Technologies in Wind Energy, Boulder, CO, October 25.

Mirocha, J.D., R.K. Rai, M.J. Churchfield, Y. Feng, C. Draxl, J. Sanz Rodrigo, B.L. Ennis, B. Kosović , and S.E. Haupt, 2017: An investigation of online and offline mesoscale-microscale coupling techniques during unsteady meteorological conditions, WindTech International Conference on Future Technologies in Wind Energy, Boulder, CO, October 25.

Rai, R.K., L.K. Berg, B. Kosović, J.D. Mirocha, S.E. Haupt, B.L. Ennis, and C. Draxl, 2017: Evaluation of the Impact on *Terra incognita* for Mesoscale and Microscale WRF Simulations, WindTech International Conference on Future Technologies in Wind Energy, Boulder, CO, October 25.

Rai, R.K., L.K. Berg, B. Kosović, J.D. Mirocha, M. Pekour, B. Ennis, and W.J. Shaw, 2017: Examination of the Spatio-Temporal Variability of the Terms of the Turbulent Kinetic Energy Budget over a Complex Terrain in the Convective Boundary Layer: A Tool for Parameterization Development, American Meteorological Society Meeting, Seattle, WA, January 24.

Sever, G., R.V. Kotamarthi, Y. Feng, 2017: A turbulence library for asynchronous coupling of meso and microscale models, WindTech - International Conference on Future Technologies in Wind Energy, Boulder, CO, October 25, 2017.

Appendix B

Contributions of Individual Laboratories

The Mesoscale-to-Microscale Coupling (MMC) project is truly a collaborative effort of national laboratories. Each laboratory takes a share of the effort and the staff works individually and collectively as MMC team members to advance the state-of-the-science of MMC. The fiscal year 2017 (FY17) contributions of the individual laboratories (in alphabetical order) are briefly summarized below.

Argonne National Laboratory (ANL): Argonne worked on building a turbulence library for asynchronous coupling of mesoscale and microscale models. All numerical experiments are performed using WRF-LES v3.9 on Argonne's computing facilities. The focus was on conducting a set of high-resolution simulations based on neutral stable atmospheric conditions. The ensemble simulations are performed to cover a range of atmospheric states as well as variability in surface roughness. Atmospheric states from well-established periodic boundary conditions are applied to open boundary simulations to test the offline-coupling approach. We are working on testing the approach for more frequent data recycling as well as comparing with other turbulence-generation methods. Gökhan and Rao participated in regular teleconferences for discussions about modeling approaches and technical details of simulations. Gökhan gave a podium presentation at the WindTech 2017 conference and participated in the follow-up meetings to discuss next year's project plan.

Lawrence Livermore National Laboratory (LLNL): During FY17, LLNL participated in the selection of case studies for various simulations undertaken by the MMC team, assisted in interpretation of field data and simulation results, developed new MMC physics parameterizations, executed and evaluated MMC simulations, and contributed to the dissemination of our project goals and technical results through journal papers, technical conference presentations, and project reports, all in close collaboration with colleagues across the team.

LLNL contributed three new codes and parameterizations to assist the MMC project. The first new code enables the stochastic cell-perturbation method to execute within one MMC simulation, rather than requiring two separate simulations, as previously implemented. The second coding effort implemented two canopy models to improve WRF's surface-layer physics for LES. Both an explicit canopy parameterization for large canopy elements and a pseudo-canopy parameterization for surfaces characterized by small roughness lengths were implemented into WRF. Several simulations using the new codes and parameterizations were executed and evaluated for relevance to improving MMC capabilities as described in Chapters 3 and 4 of this report. LLNL staff also traveled to Boulder for project meetings and visited PNNL to collaborate with staff to meet MMC project deliverables.

LLNL's dissemination efforts involved authorship of the idealized LES sensitivity study, conducted using data from the Scaled Wind Farm Test facility during FY15 and FY16, that is now accepted pending minor revisions at Wind Energy Science (LLNL led the effort with 20 coauthors from the MMC team and management). LLNL also coauthored a paper (led by PNNL) examining turbulence kinetic energy budgets from simulations in the Columbia River Gorge, which was published in *Boundary-Layer Meteorology*. LLNL presented an overview of the MMC project at the WindTech meeting in Boulder, Colorado, in October 2017. LLNL also assisted in authorship of this report, collating and synthesizing contributions by all of the laboratories into Chapters 3, 4, and 6.

Los Alamos National Laboratory (LANL): LANL participated in the project by implementing a new boundary perturbation method for turbulence generation and by testing the effects of heterogeneous vegetation on atmospheric turbulence. Laura Mazzaro contributed by designing, implementing, and testing a new perturbation method in WRFWRF, based on direct random forces applied at the nested domain boundaries. Eunmo Koo contributed by implementing and testing the force-perturbation method and comparing it with potential temperature perturbations in HIGRAD. He also collaborated with LLNL on using the canopy method for surface stress parameterization. The influence of different heterogeneous vegetation canopies on the turbulent atmospheric flow was explored with a series of idealized, heterogeneous canopy simulations using HIGRAD. Eunmo Koo and Laura Mazzaro participated in weekly teleconferences to give progress updates and technical discussion contributions. Additionally, Laura presented a poster about the new perturbation method at the WindTech 2017 conference and participated in the MMC in-person meeting on October 26-27 in Boulder, Colorado. Eunmo presented a poster comparing the force-perturbation method and potential-temperature-perturbation method using HIGRAD at the American Meteorological Society Annual meeting in January 2017 and participated in the MMC workshop in June 2017 in Boulder, Colorado.

National Center for Atmospheric Research (NCAR): As a subcontractor to PNNL, NCAR took on project leadership, with Dr. Haupt serving as project principal investigator, leading most of the team teleconferences, presenting the project at Atmosphere to Electrons (A2e) Initiative workshops and several conferences, including preparing PowerPoint slides for others to present at some conferences; preparing quarterly reports; and leading development of this third-year report. NCAR hosted a team meeting in March at which the lab personnel came together to choose cases and finalize the technical approach to modeling the nonstationary cases. At that meeting and beyond, NCAR led the process of formalizing goals and planning for the next 3 years of the project. NCAR was also responsible for the development of the metrics, including developing the metrics plan and providing the formal verification and validation of the model results, which appear in Chapters 2 and 5 of this report. The process required much processing of the data from both the Scaled Wind Farm Test tower and Wind Forecasting Improvement Project 2 site, including quality control. Model results also required significant post-processing, including providing code for the modeling teams to output their results in common formats, hosting a model repository, and planning for long-term data storage with the Data Archive and Portal team. NCAR and PNNL worked together on uncertainty quantification planning and assessment. NCAR also supplied modeling advice and guidance. NCAR summarized the results of the assessment and provided the project overview. NCAR coordinated the planning and assumed leadership for compiling and formatting this report, including writing major portions of it, although all laboratories contributed to the technical discussions and report writing.

National Renewable Energy Laboratory (NREL): During FY17, NREL performed work in further developing inflow perturbation methods to initiate turbulence in the microscale domain. NREL also further tested internal forcing methods that apply large-scale mesoscale forcings to the microscale domain as source terms. Initial simulations bringing together our coupling strategies with Columbia River Gorge complex terrain were performed, presented at the 2017 North American Wind Energy Academy Conference, and are shown in Chapter 3 of this report. In the area of microscale modeling, NREL performed WRF simulations of benchmark Wind Forecasting Improvement Project 2 days, and helped in the analysis of the output data. A study was performed on the effect of using high resolution (750 m) over complex terrain on WRF simulation results, which is presented in Chapter 2 of this report. NREL participated in MMC workshops, helping to select benchmark Wind Forecasting Improvement Project 2 cases to simulate as well as refine the MMC objectives and future-year plans.

Pacific Northwest National Laboratory (PNNL): PNNL staff have actively participated in the project in a number of different ways, including making contributions to the selection of case studies, running both mesoscale and coupled mesoscale-microscale simulations, and preparing presentations and peer-reviewed publications. In collaboration with NREL, we have conducted studies to identify the impact of horizontal grid spacing in *terra incognita* on both mesoscale and microscale simulations. In collaboration with LLNL, NREL, and NCAR, we contributed nested WRF/WRF-LES simulations that test a number of different methods to pass information from the mesoscale to the microscale models for a number of the case studies selected by the MMC team. PNNL has also contributed mesoscale simulations to NCAR for evaluation. Our work in FY17 has resulted in two peer-reviewed publications (one published in *Boundary-Layer Meteorology* and one published in the *Journal of Applied Meteorology and Climatology*) as well as presentations at the American Meteorological Society meeting and WindTech 2017. Our team has collaborated with NCAR on uncertainty quantification planning and assessment and administers the NCAR subcontract.

Distribution

No. of
Copies

\# Name
Organization
Address
City, State and ZIP Code

\# Organization
Address
City, State and ZIP Code
Name
Name
Name
Name
Name (#)

\# Name
Organization
Address
City, State and ZIP Code

No. of
Copies

\# **Foreign Distribution**
\# Name
Organization
Address
Address line 2
COUNTRY

\# **Local Distribution**
Pacific Northwest National Laboratory

Name	Mailstop
Name	Mailstop
Name	Mailstop
Name	Mailstop
Name	(PDF)

Pacific Northwest
NATIONAL LABORATORY

Proudly Operated by **Battelle** *Since 1965*

U.S. DEPARTMENT OF
ENERGY

902 Battelle Boulevard
P.O. Box 999
Richland, WA 99352
1-888-375-PNNL (7665)

www.pnnl.gov